



# MÉRNÖKI ÉS INFORMATIKAI MEGOLDÁSOK

## ENGINEERING AND IT SOLUTIONS

EÖTVÖS LORÁND UNIVERSITY  
FACULTY OF INFORMATICS  
SAVARIA INSTITUTE OF TECHNOLOGY



II. 2022.

**MÉRNÖKI ÉS INFORMATIKAI MEGOLDÁSOK**  
**ENGINEERING AND IT SOLUTIONS**

II. 2022.

# IMPRESS

## Editor-in-Chief

Dr. Ferenc Safranyik

## Editors

Dr. Mátyás Andó  
Prof. Dr. Jurij Sidor

## Editorial board

Dr. Árpád Bak	Prof. Dr. Gábor Kalácska
Dr. István Barányi	Prof. Dr. István Keppler
Dr. Gergely Bencsik	Dr. Róbert Zsolt Keresztes
Dr. Imre Czupy	Prof. Dr. László Kollár
Prof. Dr. András Eleőd	Dr. Zoltán Pödör
Dr. Gábor Farkas	Dr. Zoltán Szakál
Dr. Gusztáv Fekete	Dr. Béla János Szekeres
Dr. Dániel Fenyvesi	Dr. Attila Varga
Dr. László Gál	Dr. László Zsidai
Prof. Dr. Béla Horváth	

## Publisher

Eötvös Loránd University, Faculty of Informatics  
Savaria Institute of Technology  
Prof. Dr. László Kollár, head of institute

## Cover design

Dr. Ferenc Safranyik

HU ISSN 2677-1691

DOI: [10.37775/EIS.2022.2](https://doi.org/10.37775/EIS.2022.2)

© ELTE, Faculty of Informatics, Savaria Institute of Technology, 2022.

HU-9700, Szombathely, Károlyi Gáspár tér. 4.

Contact: [sf@inf.elte.hu](mailto:sf@inf.elte.hu), [URL](https://www.inf.elte.hu)

## TABLE OF CONTENTS

<b>János György Bátorfi, Gyula Pál, Purnima Chakravarty, Jurij Sidor</b> Models for symmetric cold rolling of an aluminum sheet .....	4
<b>Ibrahim Kipngeno Rotich, László E. Kollár</b> Numerical simulation of the performance of an asymmetrical airfoil under extreme weather conditions .....	19
<b>Bálint Varga, Balázs Mikó</b> CAD modelling of the chip shape in case of ball-end milling .....	30
<b>János György Bátorfi, Gyula Pál, Purnima Chakravarty, Jurij Sidor</b> Investigation of materials flow during the cold-rolling process by experimental evidence and numerical approaches .....	39
<b>Csaba Felhő, Frezgi Tesfom</b> Investigation of cutting force components and surface roughness in face milling with different cutting ratios .....	52
<b>Gyula Pál, Purnima Chakravarty, János György Bátorfi, Jurij Sidor</b> Microstructural study of an Aluminium sheet deformed by multistage process .....	66

# Models for symmetric cold rolling of an aluminum sheet

János György Bátorfi<sup>a,b\*</sup>, Gyula Pál<sup>a,b</sup>, Purnima Chakravarty<sup>a,b</sup>, Jurij Sidor<sup>a</sup>

<sup>a</sup> ELTE, Faculty of Informatics, Savaria Institute of Technology

<sup>b</sup> ELTE, Faculty of Science, Doctoral School of Physics

## ABSTRACT

In the current work, the behavior of Al alloys during cold rolling is studied with the help of numerical approaches such as Finite Element (FEM) and Flow-Line (FLM) Models. The applicable simplifications for each method have been summarized in this contribution. For simulating the process of rolling, a material model was employed, which is based on the measured values obtained from the tensile test. The results of the conducted rolling experiments were compared with the numerical simulations performed by employing the experimental material models. The analysis of simulated and experimental data allowed us to evaluate the friction coefficient. A relationship has been established between the minimum friction coefficient necessary for rolling and the estimated one and this result is in a good agreement with the counterpart reported in literature sources. The established method was used for the evaluation of the characteristic components of the strain, namely the normal, shear, and equivalent components. The comparative study between recorded measurements and simulations indicates that both the FEM and FLM models can be successfully applied to simulate the symmetric cold rolling process of aluminum with sufficient accuracy.

**Keywords:** *cold rolling, aluminum, finite element model, flow-line model*

## 1. Introduction

The coefficient of friction enforces a strong effect on the deformation paths during the process of rolling. This technological parameter expresses the rate of shear and normal stresses in the contacts of the sheet and the rolls, as it is expressed among others by Avitzur [2]. There are many models for describing the deformation rate as a function of various technological and physical parameters such as temperature, slip velocity in the contact, normal pressure, the shear strength of the sheets material, or the roughness of the surface [3, 4], however, in this study, a simple approximation is used with a constant value.

The presented work aims to compare various calculation techniques for estimating the strain values at different points of the sheet during the cold rolling process. The results of the analytical approximation employed were compared to the experimental counterparts. Various physical parameters were determined by these calculations, for example, the friction coefficient, which describes the frictional properties. The experimentally observed deformation flow was likewise compared to the results of FEM simulations.

---

© ELTE, Faculty of Informatics, Savaria Institute of Technology, 2022

\*Corresponding author: János György Bátorfi, bj@inf.elte.hu

<https://doi.org/10.37775/EIS.2022.2.1>

## 2. Tensile and rolling samples

The FEM simulations required a material model, the parameters of which were determined from the strain-stress curve, obtained by the tensile test. Prior to tensile testing and rolling experiments, the samples were heat-treated at 550 °C for 3 min for reducing the effect of previous thermo-mechanical treatments. The samples were prepared from a sheet of Al-1050 with an initial thickness of 2 mm. Gauge length and initial cross section of the tensile samples are 50 mm and 18.44 mm<sup>2</sup> respectively. The strain and stress values are calculated by Eq. (12) and (2), as described by Santaoja [5, 6].

$$\varepsilon = \ln \left( 1 + \frac{\Delta l}{l_0} \right), \quad (1)$$

$$\sigma = \frac{F}{A_0} \left( 1 + \frac{\Delta l}{l_0} \right). \quad (2)$$

The strain-stress diagram is shown in Fig. 1. The tensile test data are fitted by the Ramberg-Osgood material model by using Eq. (3) [7, 8]:

$$\varepsilon = \frac{\sigma}{E} + \left( \frac{\sigma}{K} \right)^{1/c} \quad (3)$$

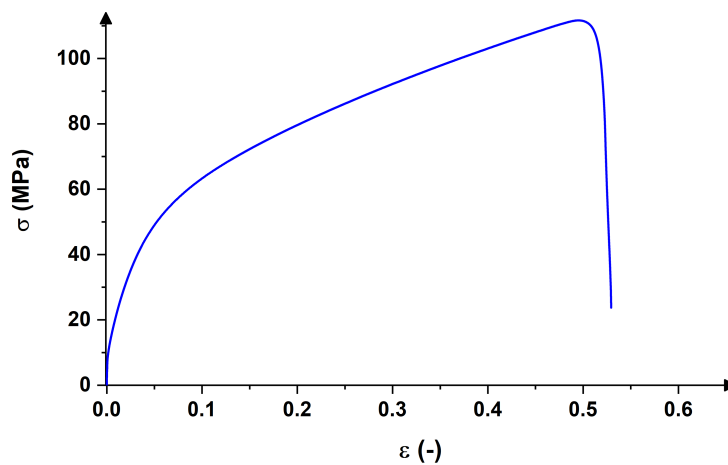
The parameters of the material model are presented in Table 1. The correlation factor for the measured and fitted values is 0.9996. The rolling was performed with geometrical dimensions described in Table 2.

**Table 1.** Parameters for the Ramberg-Osgood material model

Parameter	Value
$E$ [GPa]	69.9
$K$ [MPa]	144.6
$c$ [-]	0.37

**Table 2.** Parameters of cold rolling

Parameter	Value
Radius of the roll, $R$ [mm]	75
Initial thickness of the sheet, $h_i$ , [mm]	2
Sheet thickness following rolling, $h_f$ , [mm]	1.4
Angular velocity of the rolls, $\omega$ , [rad/s]	1.1023



**Figure 1.** Strain-stress values for tensile test

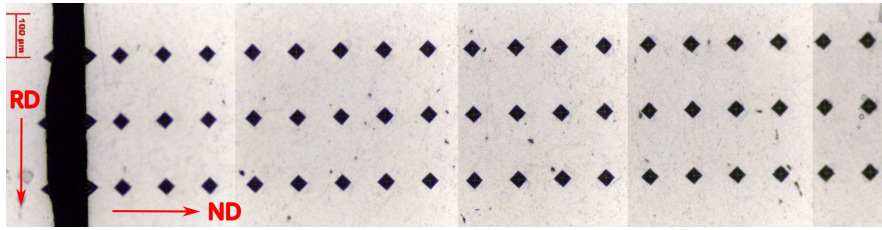


Figure 2. The prepared surface of the sheet prior to cold rolling

### 3. Rolling

In most general case, rolling can be defined as a widely used manufacturing process employed for reducing the thickness of materials. The rolling experiment is performed by pressing the sheet material between 2 rotating rolls. Based on the velocity of the bottom and top rolls, the rolling process can be defined as symmetric and asymmetric. On the other hand, based on temperature maintained during the deformation, symmetric and asymmetric rolling can be categorized as cold and hot rolling [9]. In this study, only the cold symmetrically rolled material has been studied. The geometrical model of the roll gap, showing the half-thickness of a rolled sheet is presented in Fig. 3. This simplified, half-geometry is used in the numerical models employed.

After rolling, the initially straight lines made of indents became distorted, and the displacements of the sheet layers are shown in Fig. 4. To further proceed with the study, the plane perpendicular to the transverse direction (TD plane) was grinded and polished, and afterward a pattern, consisting of numerous points, was created by microhardness indents as it is shown in Fig. 2.

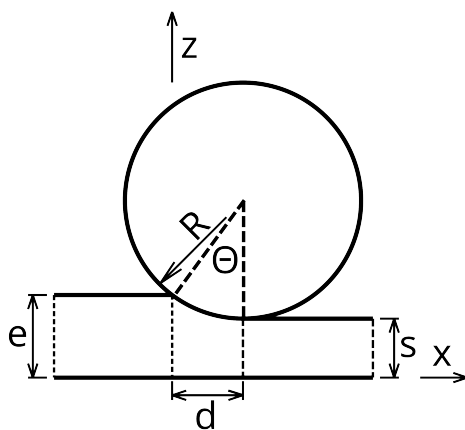


Figure 3. Simplified geometry used for FEM and FLM

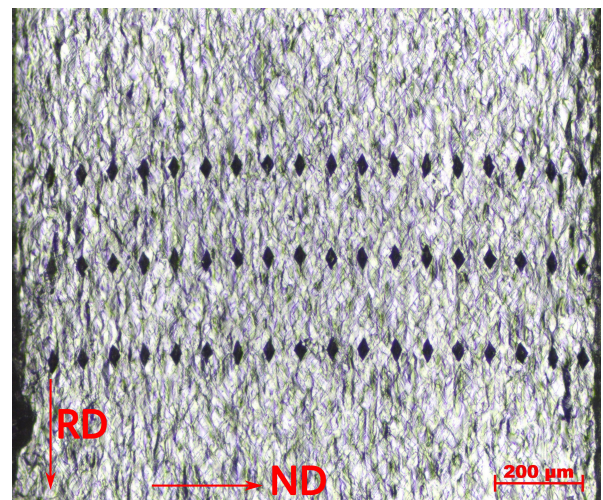


Figure 4. Distortion of initially straight lines caused by cold rolling

The displacement of a particular layer can be determined by the method developed by Boldetti [10], Roumina [11], and Ma [12]. The mentioned methodology allows us to calculate the strain values as it is described by Eq. (4-7) [12, 13]:

$$\varepsilon = \frac{h_i - h_f}{h_i}, \quad (4)$$

$$\gamma = \frac{dz}{dx}, \quad (5)$$

$$\varepsilon_S = \frac{2(1 - \varepsilon)^2}{\varepsilon(2 - \varepsilon)} \gamma \cdot \ln \frac{1}{1 - \varepsilon}, \quad (6)$$

$$\varepsilon_{vM} = \sqrt{\frac{4}{3} \left( \ln \left( \frac{1}{1 - \varepsilon} \right) \right)^2 + \frac{\varepsilon_S^2}{3}}, \quad (7)$$

where  $\varepsilon$  is a thickness reduction,  $z$  is a coordinate along the thickness of the sheet,  $x$  is a displacement of the sheet in the rolling direction,  $\gamma$  is a derivative of displacement of the sheet in the rolling direction,  $\varepsilon_S$  is the shear deformation, and  $\varepsilon_{vM}$  is a von Mises strain.

An important parameter of the rolling process is the friction coefficient  $\mu$ , which is the result of a complex mechanism, effected by various physical parameters, as is summarised by Szűcs [3, 14] and Sidor [15]. The most important parameters allowing estimation of  $\mu$  are the temperature, the pressure that acts on the surface, and the slip velocity between the sheet and the rolls [3]. According to a commonly used approximation, these dependencies can be neglected, and one can estimate a representative value of  $\mu$  for the entire process, i.e. a constant  $\mu$  is assumed for a given roll gap geometry. According to the model of Avitzur [16], a minimum value of friction coefficient can be determined by Eq. (8):

$$\mu_{min} = \frac{1}{2} \sqrt{\frac{h}{R} \ln \left( \frac{h_i}{h_f} \right) + \frac{1}{4} \sqrt{\frac{h_i - h_f}{R}}} \cdot \tan^{-1} \left( \frac{h_i}{h_f} - 1 \right). \quad (8)$$

The  $\mu_{min}$  calculated by using the parameters presented in Table 2 is 0.049. Alternative models dealing with the friction are described in [3, 14, 16–22]. The studies can be extended with further parameters such as microstructural properties as described by Sidor [23].

#### 4. Finite Element Model

Finite element modeling is a commonly used method to describe the deformation conditions of the manufacturing process [24–28]. In this study, the commercially available DEFORM 2D software [29] was used, which is designed for modeling the plastic deformation. For the simulation, the previously described Ramberg-Osgood model was used. The further parameters are set as described in Table 2, with the extension, that the friction coefficient was changed between the  $\mu_{min}$  and  $\mu = 0.25$ .

The optimum value of the friction coefficient was determined by comparing the experimentally observed and simulated deformation patterns. The geometry of the roll gap is visible in Fig. 5. The



Figure 5. Rolling gap geometry used in the FEM simulation



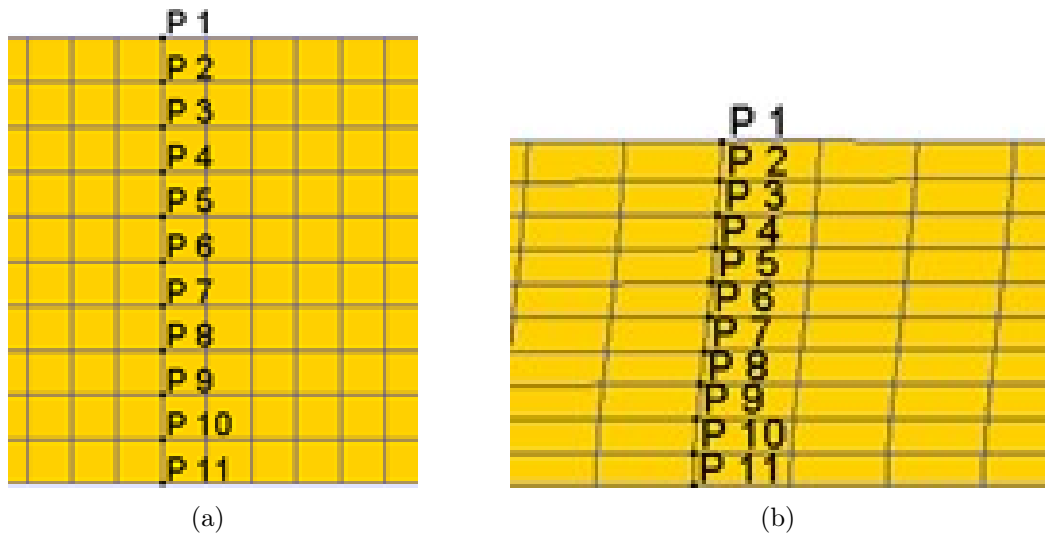


Figure 6. a) Mesh prior to rolling, b) Mesh distortion after 30% rolling reduction

sheet was subdivided into 10 layers, while each layer contains identical square shaped elements. The meshed sheets before and after the rolling are presented in Figs. 6(a) and 6(b).

The deformation pattern extracted from the deformed sheet and the simulated counterparts with different constant friction coefficients are shown in Fig. 7. The wide-dashed line is the average displacement calculated from the 3 different measured line, the narrow-dashed line represents the tolerance limits calculated from the measured points, by adding and subtracting the standard deviations. It is important to mention, that the  $dx$  and  $z$  coordinates are equal to 0 on the symmetry plane of the rolled sheet. The estimated friction coefficient, based on a comparison of distorted lines, is approximately 0.068.

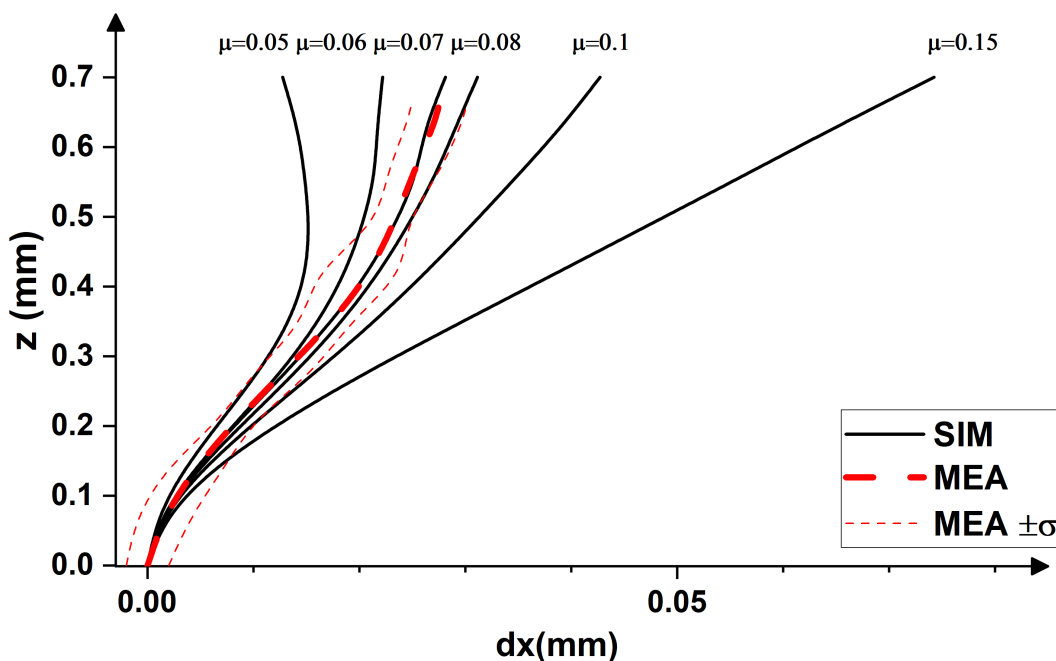


Figure 7. Deformation patterns of measured (MEA) and simulated displacements for 30% thickness reduction

## 5. Flow-Line Model (FLM)

There are different simplified numerical models, which can be used for a well-specified manufacturing process. The most commonly used types are based on simplified hydrodynamical models, for example, the Flow-Line Model (FLM) [30]. This model is based on the description of the virtual flowlines described by means of analytical functions. The model used in this study consist of a function expressed in the form of Eq. (9) by Beausir [30] and Decroos [31].

$$\Phi(x, z) = \frac{z_s}{\alpha} = z \left[ 1 + \left( \alpha + \frac{(1 - \alpha)(x - d)^2}{d^2} \right)^{-n} \right]^{1/n}, \quad (9)$$

where  $x$ ,  $z$  coordinates on the sheet as defined in Fig. 3,  $z_s$  relative coordinate on the rolled sheet's thickness,  $\alpha$  and  $n$  are later explained parameters used for describing the flowlines' deformation characteristics, the definition of these parameters are different for various models. For further calculations, it is important to define the following parameters:

$$\alpha = \frac{s}{e}, \quad (10)$$

$$\cos(\theta) = \frac{R + s - e}{R}, \quad (11)$$

$$d = R \sin(\theta), \quad (12)$$

where  $s$  half of the thickness after rolling,  $e$  half of the thickness before rolling,  $\alpha$  is a parameter used for calculating the thickness's relative change,  $\theta$  is the press angle,  $d$  is the projected length of pressed arc. By using these definitions, the velocity components for the directions can be defined by Eq. (13) and (14) as defined by Beausir [30].

$$v_x(x, z) = \lambda(x, z) \frac{\partial \Phi(x, z)}{\partial z}, \quad (13)$$

$$v_z(x, z) = -\lambda(x, z) \frac{\partial \Phi(x, z)}{\partial x}. \quad (14)$$

The  $\lambda(x, z)$  function is defined by a velocity boundary condition in the exit points of the rolling gap, with Eq. (15) [30].

$$\lambda(x, z) = \frac{v_x(x = d, z)}{(\alpha^{-n} + 1)^{1/n}}. \quad (15)$$

The velocity profile can be calculated by Eq. (16) [30].

$$v_x(x = d, z) = A \cdot z_s^2 + B \cdot z_s + C, \quad (16)$$

where  $A$ ,  $B$ , and  $C$  parameters can be calculated by Eq. (17)-(23) [30].

$$A = v_0^t + v_0^b - 2 \frac{v_0 + v_n}{2s^2}, \quad (17)$$

$$B = \frac{v_0^t - v_0^b}{s^2}, \quad (18)$$

$$C = v_0 + v_n, \quad (19)$$

$$v_0^t = \omega^t R, \quad (20)$$

$$v_0^b = \omega^b R, \quad (21)$$

$$v_0 = \frac{\omega^t + \omega^b}{2} R, \quad (22)$$

$$v_n = -pv_0, \quad (23)$$

where  $p$  parameter for describing the frictional conditions,  $w^t$  and  $w^b$  are the angular velocities for top and bottom rolls. By knowing the components of velocity, the velocity gradients can be expressed in general form with Eq. (24) by applying the theory of Beausir [30]:

$$L_{ij} = \frac{\partial v_i}{\partial j}. \quad (24)$$

The values of the displacement components were determined by Eq. (25) [24]:

$$D_{ij} = \int_0^L \frac{L_{ij}}{v_x} dx. \quad (25)$$

The strain tensor components can be calculated by Eq. (26).

$$\varepsilon_{ij} = \varepsilon_{ji} = \frac{D_{ij} + D_{ji}}{2}. \quad (26)$$

The fitted value for the parameter  $p$  is 0.0025.

## 6. Modified version of Flow-Line Model (mFLM)

In [15, 31] a partially modified version of the FLM model is described. The main difference compared to the previous version of FLM is that the flow line's definition and the definition of  $v_x$  velocity is different. The updated version is given by Eq. (27) and (28), this modified version was developed by Decroos [31]. Other numerical models are founded for example in [32–40].

$$\Phi(x, z) = \frac{z}{e} \left[ 1 + \left( \frac{s}{e} + \left( 1 - \frac{s}{e} \right) \left( \frac{d-x}{d} \right)^{2.1} \right)^{-m} \right]^{1/m}, \quad (27)$$

$$v_x(x, z) = f_1(x) \cdot (1 - z_s)^n + f_2(x) \cdot z_s^n. \quad (28)$$

The  $f_1(x)$  and  $f_2(x)$  functions can be calculated from the boundary condition, by applying the Eq. (29) and (30) of the Decroos' theory [31].

$$\frac{1}{n+1} f_1(x) + \frac{1}{n+1} f_2(x) = v_{in} \cdot \left[ 1 + \left( \frac{s}{e} + \left( 1 - \frac{s}{e} \right) \left( \frac{d-x}{d} \right)^{2.1} \right)^{-m} \right]^{1/m}, \quad (29)$$

$$f_2 - f_1 = \alpha \cdot \left\{ e \cdot v_{in} \cdot \left[ 1 + \left( \frac{s}{e} + \left( 1 - \frac{s}{e} \right) \left( \frac{d-x}{d} \right)^{2.1} \right)^{-m} \right]^{1/m} - f_{1,ref} \right\}, \quad (30)$$

where,  $v_{in}$  is the velocity of the sheet before rolling, this value can be approximated by the angular velocity of rolls,  $m$  is an arbitrary parameter, in our study the, the applied value is 50. The  $f_{1,ref}$  function can be defined by Eq. (31) [31].

$$f_{1,ref} = \left[ 1 - e^{-a \left( \frac{x}{d} \right)^b} \right] \left( \frac{e}{s} v_{in} - v_{in} \right) + v_{in}. \quad (31)$$

The parameter  $b$  in the Eq. (29)-(31) is an arbitrary number, in this study, the value of 3 was chosen according to reference [31]. This value was determined by comparing various simulation methods, by Decroos [31]. The parameter  $a$  is parameter based on the relative position of the neutral point, the

**Table 3.** Friction coefficients defined for various computational techniques

Method	Value
FEM	$\mu = 0.068$
FLM	$p = 0.0025$
mFLM	$\mu = 0.070$
Theory, Eq. (8)	$\mu = 1.4\mu_{\min} = 0.0685$

calculation method is described in [31]. Determination of  $\alpha$  and  $n$  was done by the model of Sidor [15], which employs Eq. (32)-(34) for the estimation of both model parameters.

$$\Psi = \mu^{1.833} \cdot \left(\frac{h_i}{R}\right)^{0.789} \cdot \left(\frac{R}{h_i - h_f}\right)^{0.2293} \cdot \left(\frac{R}{h_f}\right)^{0.2983}, \quad (32)$$

$$\alpha = 21.332\Psi - 225\Psi^2 - 184.1\Psi^3 + 12420\Psi^4 + 0.4833 \left(\frac{h_i - h_f}{2L_d}\right), \quad (33)$$

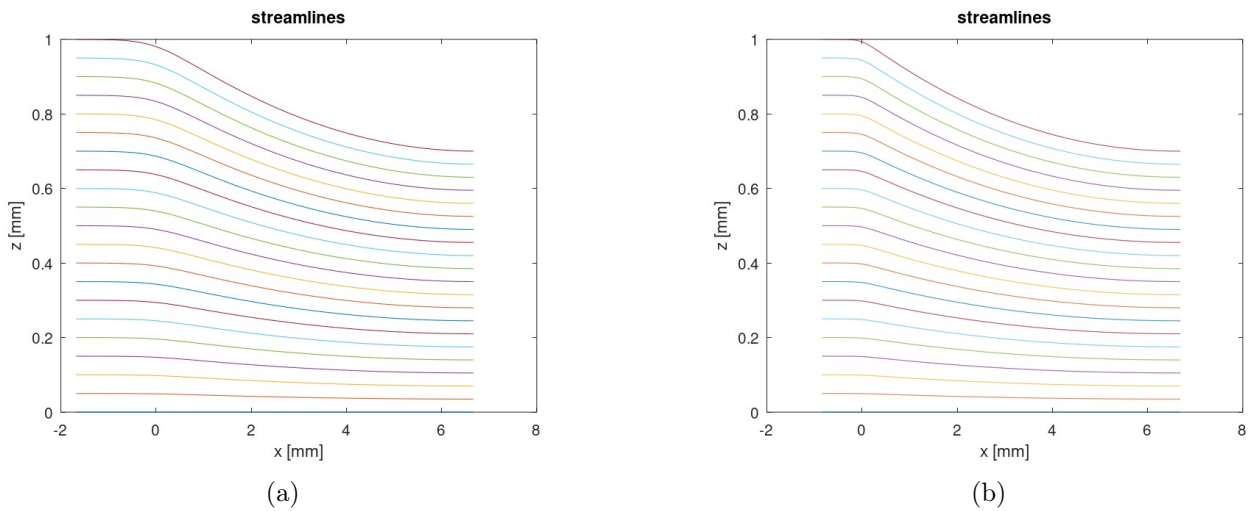
$$n = 19.369\mu^{0.09882} \left(\frac{h_i}{R}\right)^{0.00512} + 9.463\mu^{-0.1869} \left(\frac{L_d}{L_{dN}}\right)^{0.06414} - \quad (34)$$

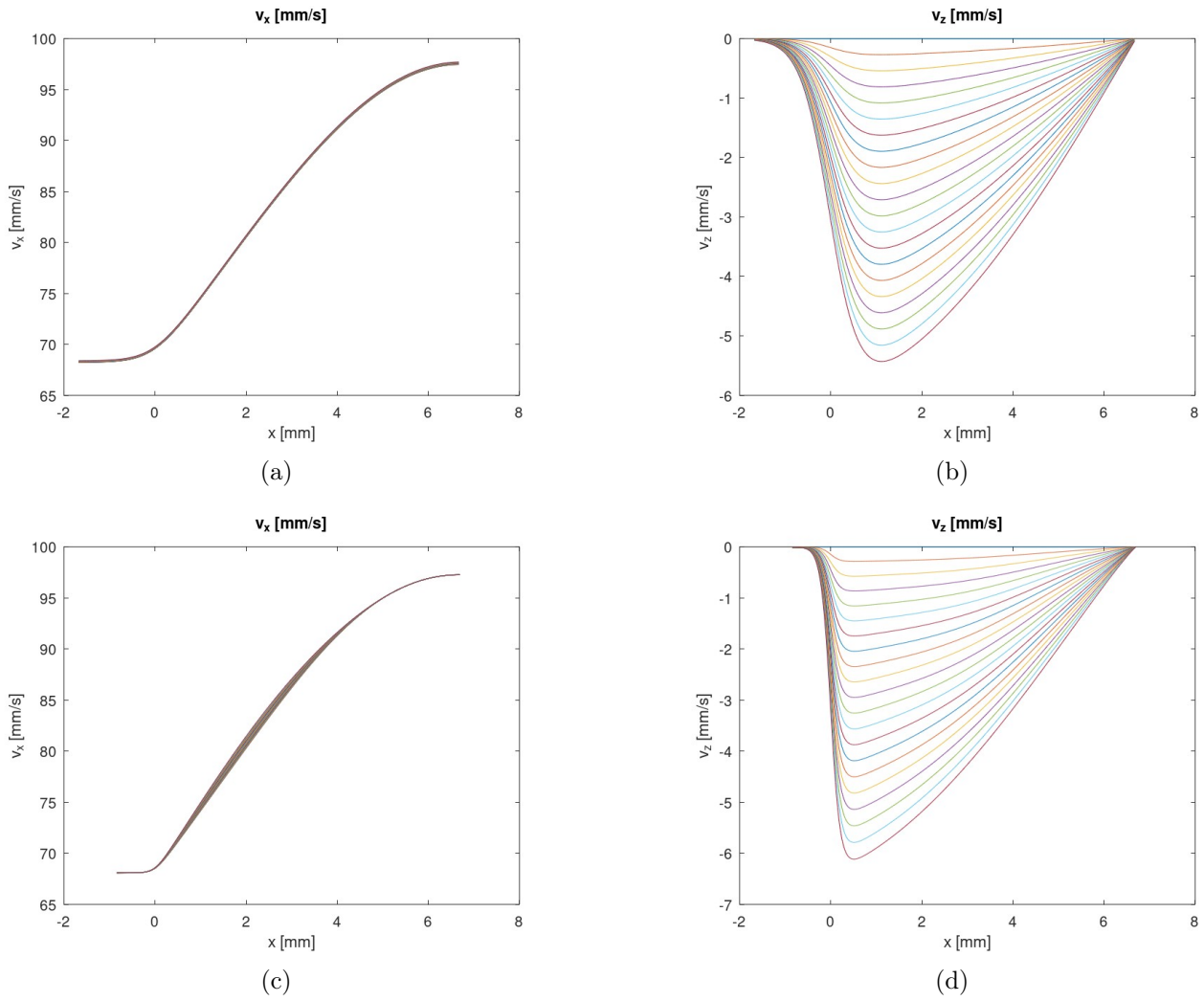
$$- 18.606\mu^{-0.1045} \left(\frac{h_i + h_f}{R}\right)^{-0.00586} - 9.086\mu^{0.2441} \left(\frac{L_d}{h_i + h_f}\right)^{-0.162} + 0.03201,$$

where,  $L_d$  is the projected length of the pressed arc,  $L_{dN}$  is the position of the neutral point on the pressed arc,  $\alpha$  and  $n$  are intermediate parameters used for the FLM model, these parameters have a different meaning, than in previous model. Substituting the values of roll gap geometry into Eq. (32)-(34) yields to the  $\mu = 0.07$ .

## 7. Comparison

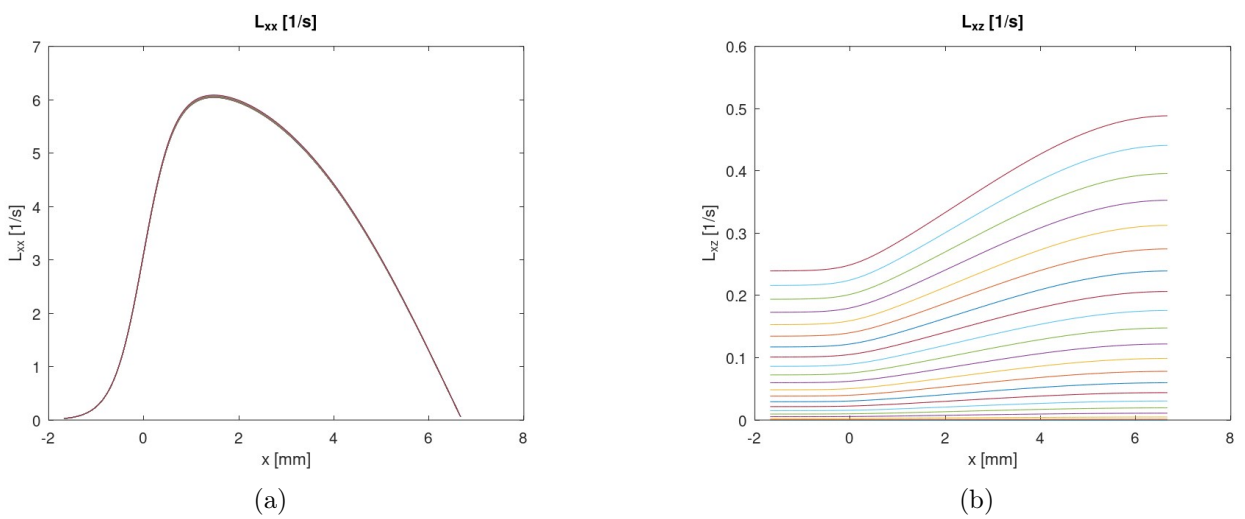
The determined values of  $\mu$  for each method are presented in Table 3. The estimated friction coefficients by the FEM and the mFLM are comparable to the  $\mu_{\min}$  (see Eq. (8)). It should be noted here that it is difficult to validate the accuracy of the FLM model since the model parameter  $p$  is not correlated directly with the  $\mu$ . These obtained friction coefficients can be compared to the result

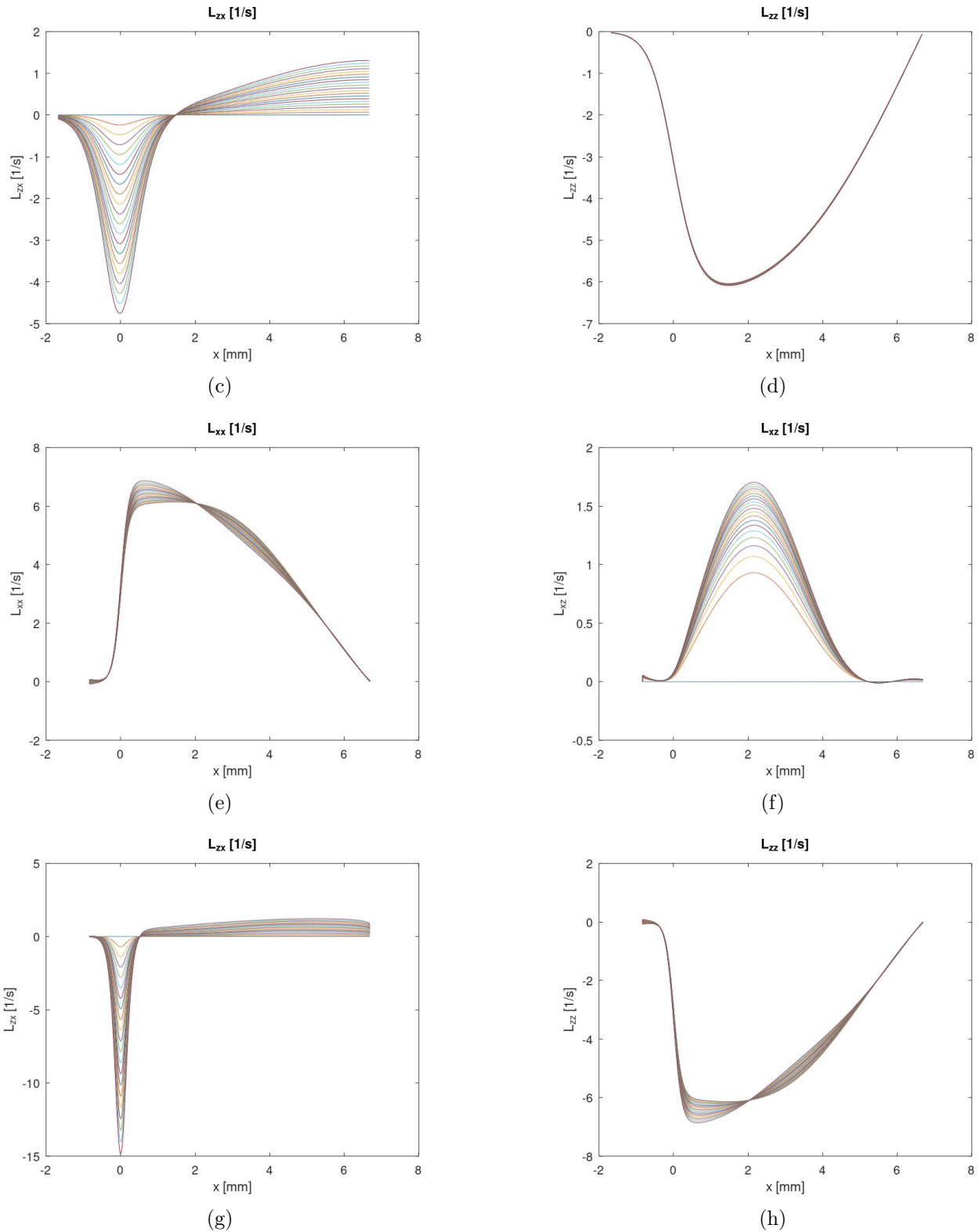
**Figure 8.** Flowlines determined with the FLM (a) and mFLM (b) models



**Figure 9.** Velocity in x and z directions predicted by the FLM (a, b) and mFLM (c, d) models

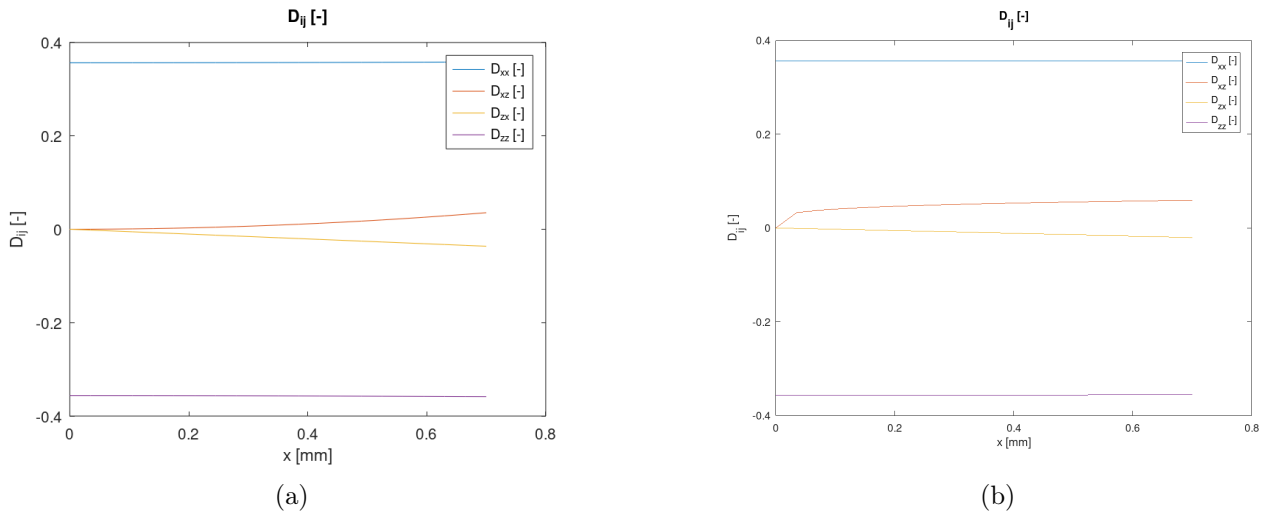
of [1], where  $\mu$  was estimated as 0.068. Based on the above analysis, one can conclude, that the friction coefficient can be derived from the FEM and mFLM simulations. The described FLM and





**Figure 10.** Velocity gradients in directions  $xx$ ,  $xz$ ,  $zx$ , and  $zz$  for FLM (a-d) and mFLM (e-h) models

mFLM models are solved by using GNU Octave numerical software package [41]. Comparison of the deformation flow as predicted by the FLM and mFLM are demonstrated in Figs. 9-11. Based only on the flowlines of Fig. 8(a) and 8(b), it can be concluded that there is a negligible difference between



**Figure 11.** Strain components predicted by the FLM (a) and mFLM (b) models

the FLM and mFLM models. The difference is observed mainly near the entry part of the roll gap. Similar to the flowline models, differences in velocity are observable, especially in the direction  $z$  (Fig. 9(b), 9(d)).

It can be concluded, that directional velocity gradients are similar for FLM and mFLM only for  $xx$  (Fig. 10(b), 10(e)) and  $zz$  (Fig. 10(d), 10(h)) directions. In the case of the  $zx$  direction, the difference is higher compared to  $xx$  and  $zz$  directions. These deviations can be attributed to the different flowlines near to the entry point of the roll gap. For the direction  $xz$ , the difference between the two model predictions is quite noticeable, and the tendency of the lines is different between the FLM and mFLM models, however, the individual tendencies are corresponding to the models described in literature sources [24, 30] and [15, 31].

The calculated strain components in the rolled sheet by both FLM and mFLM models are shown in Fig. 11. As one can notice, the strain components are comparable to each other, while there is a slight difference near the mid-thickness of the rolled sheet. The shear strain values predicted by the models employed are given in Table 4. It seems that all methods tend to provide comparable shear strains.

### 8. Summary

In the present study, the measured deformation patterns of a rolled sheet are analyzed by various numerical approaches. The study suggests that the commonly used FEM model can be successfully employed for the simulation of the rolling process. The friction coefficient of 0.068 ensures a deformation flow in a cold rolled material with a 30% thickness reduction comparable to the experimentally observed one. Nearly identical value for the  $\mu$  was predicted the Flow-Line Model employed [31].

**Table 4.** Shear strain values predicted by the models employed

Method	Value
Measured	$\gamma_s = 0.020$
FEM	$\gamma_s = 0.030$
FLM	$\gamma_s = 0.030$
mFLM	$\gamma_s = 0.025$

The minimum value of friction coefficient, necessary for cold rolling, as predicted by the analytical approach is comparable to ones derived by the FEM and FLM approaches. Both FEM and FLM methods were found to be suitable for describing the cold rolling, however, the computational time in case of FLM was orders of magnitude shorter as compared to FEM simulations.

In the later work, the model can be extended by the implementation of additional technological parameters, which will allow for: explaining the effect of heat generation, the nonuniformity of the friction coefficient, and the effect of the asymmetry due to different roll velocity. On the other hand, a new model can be developed for describing the anisotropy of the sheet's material, the hardening of the material, and its microstructural properties. In this way, a new, more precise material model will be used for the numerical simulations. The assessment of numerical approaches can be validated by relatively simple rolling trials.

## 9. Acknowledgement

Project no. TKP2021-NVA-29 has been implemented with the support provided by the Ministry of Innovation and Technology of Hungary from the National Research, Development and Innovation Fund, financed under the TKP2021-NVA funding scheme.

## 10. References

- [1] J.Gy. Bátorfi, J.J. Sidor, *Alumínium lemez aszimmetrikus hengerlése közben fellépő deformációjának vizsgálata*, Mérnöki és Informatikai Megoldások|Engineering and IT Solutions, 2020. I, pp. 5–14, [CrossRef](#)
- [2] B. Avitzur, *An upper-bound approach to cold-strip rolling*, Journal of Engineering for Industry 86(1), 1964, pp. 31–45, [CrossRef](#)
- [3] M. Szűcs, Gy. Krallics, J.G. Lenard, *The difficulties of predicting the coefficient of friction in cold flat rolling*, Journal of Tribology 143(10), 2021, 101703, [CrossRef](#)
- [4] A. Fischer, K. Bobzin, *Friction, wear and wear protection*, International Symposium on Friction, Wear and Wear Protection 2008, Aachen, Germany, Weinheim, Germany, Wiley-VCH, 2008.
- [5] C. Cerbu, H. Teodorescu-Draghicescu, *Aspects on modeling the mechanical behavior of aluminum alloys with different heat treatments*, Journal of Computational and Applied Mechanics 12(2), 2017, pp. 85–98, [CrossRef](#)
- [6] K. Santaoja, *Viscous and elastic-plastic material model in the ABAQUS*, Espoo: Technical Research Centre of Finland, 1993.
- [7] G. Gadamchetty, A. Pandey, M. Gawture, *On Practical Implementation of the Ramberg-Osgood Model for FE Simulation*, SAE International Journal of Materials and Manufacturing 9(1), 2016, pp. 200–205, [CrossRef](#)
- [8] W. Ramberg, W.R. Osgood, *Description of stress-strain curves by three parameters*, 1943, [CrossRef](#)
- [9] O. Engler, J. Hirsch, *Texture control by thermomechanical processing of AA6xxx Al–Mg–Si sheet alloys for automotive applications — a review*, Materials Science and Engineering A 336(1–2), 2002, pp. 249–262, [CrossRef](#)



- [10] C. Boldetti, C. Pinna, I.C. Howard, G. Gutierrez, *Measurement of deformation gradients in hot rolling of AA3004*, *Experimental Mechanics* 45(6), 2005, pp. 517–525, [CrossRef](#)
- [11] R. Roumina, C.W. Sinclair, *Deformation geometry and through-thickness strain gradients in asymmetric rolling*, *Metallurgical and Materials Transactions A* 39(10), 2008, pp. 2495–2503, [CrossRef](#)
- [12] C. Q. Ma, L.G. Hou, J.S. Zhang, L.Z. Zhuang, *Strain Analysis during the Symmetric and Asymmetric Rolling of 7075 Al Alloy Sheets*, In: M. Hyland (Ed.), *Light Metals 2015*, pp. 445–449, Springer International Publishing, [CrossRef](#)
- [13] S.S. Dhinwal, L.S. Tóth, *Unlocking deformation path in asymmetric rolling by texture simulation*, *Materials* 13(1), 2019, 101, [CrossRef](#)
- [14] M. Szűcs, Gy. Krállics, J. Lenard, *A comparative evaluation of predictive models of the flat rolling process*, *Periodica Polytechnica Mechanical Engineering* 62(2), 2018, pp. 165–172, [CrossRef](#)
- [15] J.J. Sidor, *Assessment of flow-line model in rolling texture simulations*, *Metals* 9(10), 2019, 1098, [CrossRef](#)
- [16] B. Avitzur, *Friction-aided strip rolling with unlimited reduction*, *International Journal of Machine Tool Design and Research* 20(3–4), 1980, pp. 197–210, [CrossRef](#)
- [17] T. Miłek, *The influence of friction coefficient on forward slip in experimental research on cold longitudinal flat rolling*, presented at the 10th Conference on Terotechnology, 2018, pp. 67–72, [CrossRef](#)
- [18] Q.Y. Wang, Y. Zhu, Y. Zhao, *Friction and forward slip in high-speed cold rolling process of aluminum alloys*, *Applied Mechanics and Materials* 229–231, 2012, pp. 361–364, [CrossRef](#)
- [19] H. Jin, D.J. Lloyd, *The different effects of asymmetric rolling and surface friction on formation of shear texture in aluminium alloy AA5754*, *Materials Science and Technology* 26(6), 2010, pp. 754–760, [CrossRef](#)
- [20] M. Qwamizadeh, M. Kadkhodaei, M. Salimi, *Asymmetrical sheet rolling analysis and evaluation of developed curvature*, *The International Journal of Advanced Manufacturing Technology* 61(1–4), 2012, pp. 227–235, [CrossRef](#)
- [21] G.-Y. Tzou, *Relationship between frictional coefficient and frictional factor in asymmetrical sheet rolling*, *Journal of Materials Processing Technology* 86(1–3), 1999, pp. 271–277, [CrossRef](#)
- [22] L.A. de Carvalho, J. Ebrahim, Zs. Lukács, *The importance of pressure and velocity dependent friction coefficient in the metal forming simulation*, *GÉP LXXII(1–2)*, 2021, pp. 11–14, [CrossRef](#)
- [23] J.J. Sidor, P. Chakravarty, J.Gy. Bátorfi, P. Nagy, Q. Xie, J. Gubicza, *Assessment of dislocation density by various techniques in cold rolled 1050 aluminum alloy*, *Metals* 11(10), 2021, pp. 1571, [CrossRef](#)

- [24] J.J. Sidor, R.H. Petrov, L. Kestens, *Texture control in aluminum sheets by conventional and asymmetric rolling*, In: Comprehensive Materials Processing, Elsevier, 2014, pp. 447–498, [CrossRef](#)
- [25] J.Gy. Bátorfi, M. Andó, *Study of parameters during aluminum cutting with finite element method*, Periodica Polytechnica Mechanical Engineering 64(2), 2020, pp. 136–144, [CrossRef](#)
- [26] J.Gy. Bátorfi, P. Chakravarty, J.J. Sidor, *Investigation of the wear of rolls in asymmetric rolling*, Mérnöki és Informatikai Megoldások|Engineering and IT Solutions 2021 II, pp. 14–20, [CrossRef](#)
- [27] T. Inoue, *Strain variations on rolling condition in accumulative roll-bonding by finite element analysis*, In: D. Moratal (Ed.), Finite Element Analysis, Sciyo, 2010, [CrossRef](#)
- [28] T. Inoue, H. Qiu, R. Ueji, *Through-thickness microstructure and strain distribution in steel sheets rolled in a large-diameter rolling process*, Metals 10(1), 2020, 91, [CrossRef](#)
- [29] J. Fluhrer, *DEFORM(TM) 2D Version 8.1 User's Manual*, Scientific Forming Technologies Corporation, [CrossRef](#)
- [30] B. Beausir, L.S. Tóth, *A new flow function to model texture evolution in symmetric and asymmetric rolling*, In: A. Haldar, S. Suwas, D. Bhattacharjee (Eds.), Microstructure and Texture in Steels, London, Springer London, 2009, pp. 415–420, [CrossRef](#)
- [31] K. Decroos, J.J. Sidor, M. Seefeldt, *A new analytical approach for the velocity field in rolling processes and its application in through-thickness texture prediction*, Metallurgical and Materials Transactions A 45(2), 2014, pp. 948–961, [CrossRef](#)
- [32] F. Ďuroský, L. Zboray, Ž. Ferková, *Computation of rolling stand parameters by genetic algorithm*, Acta Polytechnica Hungarica 5(2), 2008, pp. 59–70.
- [33] Y. Tian, Y. Guo, Z. Wang, G. Wang, *Analysis of rolling pressure in asymmetrical rolling process by slab method*, Journal of Iron and Steel Research International 16(4), 2009, pp. 22–26, [CrossRef](#)
- [34] G. Hirt, S. Senge, *Selected processes and modeling techniques for rolled products*, Procedia Engineering 81, 2014, pp. 18–27, [CrossRef](#)
- [35] Gy. Krállics, M. Szűcs, J. Lénárd, *Súrlódási tényező meghatározása lemez hideghengerlésnél*, Bányászati és Kohászati Lapok - Kohászat 145(2), 2012, pp. 3–6.
- [36] A. Halloumi, Ch. Desrayaud, B. Bacroix, E. Rauch, F. Montheillet, *A simple analytical model of asymmetric rolling*, Archives of Metallurgy and Materials 57(2), 2012, pp. 425–435, [CrossRef](#)
- [37] J.J. Minton, C.J. Cawthorn, E.J. Brambley, *Asymptotic analysis of asymmetric thin sheet rolling*, International Journal of Mechanical Sciences 113, 2016, pp. 36–48, [CrossRef](#)
- [38] M. Mišović, N. Tadić, M. Jaćimović, M. Janjić, *Deformations and velocities during the cold rolling of aluminium alloys*, Materiali in tehnologije 50(1), 2016, pp. 59–67, [CrossRef](#)
- [39] S.L. Oh, S. Kobayashi, *An approximate method for a three-dimensional analysis of rolling*, International Journal of Mechanical Sciences 17(4), 1975, pp. 293–305, [CrossRef](#)

- 
- [40] Y.-M. Hwang, T.-H. Chen, H.-H. Hsu, *Analysis of asymmetrical clad sheet rolling by stream function method*, International Journal of Mechanical Sciences 38(4), 1996, pp. 443–460, [CrossRef](#)
- [41] J.W. Eaton, D. Bateman, S. Hauberg, *GNU Octave version 7.1.0 manual: a high-level interactive language for numerical computations*, 2022, [CrossRef](#)

# Numerical simulation of the performance of an asymmetrical airfoil under extreme weather conditions

Ibrahim Kipngeno Rotich<sup>a,b\*</sup>, László E. Kollár<sup>a</sup>

<sup>a</sup> ELTE, Faculty of Informatics, Savaria Institute of Technology

<sup>b</sup> ELTE, Faculty of Science, Doctoral School of Environmental Sciences

## ABSTRACT

This paper presents a numerical study of icing of a NACA2412 airfoil and the aerodynamic performance of the airfoil with ice accretion. The study analyzes the effects of liquid water content, accretion time and varying angles of attack (AoA) up to 20° on ice accretion and, consequently, on the aerodynamic coefficients of the airfoil. The free stream velocity and air temperature were kept constant in the simulations. Results revealed that the ratio of lift and drag coefficients was the highest after a short accretion time (i.e., about 20 minutes) for AoA up to 10°, but then it decreased significantly with accretion time. Ice accretion increased with time; its mass was the greatest at 10° of AoA. The results can be beneficial for designing blade shapes to optimize wind turbine performance during adverse weather conditions.

**Keywords:** *ice accretion, ice mass, aerodynamic performance, airfoil, LWC*

## 1. Introduction

Icing conditions pose a great danger in the power production of wind turbines, causing uncertainties in future power demand [1, 2]. Other associated impacts of icing include increased operation and maintenance costs, structural integrity disturbance, lifespan reduction of wind turbines and permanent stall of turbines [3–6]. The icing depends on parameters such as freestream velocity, temperature, liquid water content (LWC), and droplet size distribution (DSD). The temperature affects the icing rate and nature of ice (rime, glaze or mixed) formed on the surface. LWC determines water present in the icing domain showing the severity of icing, type and shape of ice. Droplet diameter influences the local collision efficiencies, icing rate and type of ice formed. The geometry of the airfoil, i.e., airfoil orientation, angle of attack and surface roughness, determines the accretion rate, while accretion time affects the ice shape and mass of ice. The combined effects of the thermodynamic parameters determine the icing intensity on the airfoil surface [7]. Small water droplets may have a temperature below 0° without freezing. When these supercooled water droplets hit the cold surface, they freeze upon impact to form the ice accretion. The process is called dry growth if there is no unfrozen water on the surface and it results in rime ice. When there is a liquid layer on the surface, then the process is called wet growth and it results in glaze ice.

Power loss is affected by the accretion's intensity, frequency and duration of icing events [8] estimated that 20% of power losses occurs annually due to icing [9]. Gao & Hu [10] studied the effect of icing on a utility-scale turbine for a period of 51 hrs yielding 25 MW power loss. Homola et al.

---

© ELTE, Faculty of Informatics, Savaria Institute of Technology, 2022

\*Corresponding author: Ibrahim Kipngeno Rotich, [ibrahimrkipp@gmail.com](mailto:ibrahimrkipp@gmail.com)

<https://doi.org/10.37775/EIS.2022.2.2>

[11] simulated icing effect on NREL 5MW baseline turbine leading to 24-27% power loss. The need to reduce power loss has been in constant progress with several studies done. Icing controls using microwaves and other anti/de-icing techniques minimize the impact of icing, but their applicability is becoming a challenge due to costs and the amount of energy needed in heating [12–15]. Simulation of icing helps improve safety and maintenance, reduce power losses, and decrease the load on the blade, which can cause the delamination and fracturing of the blade and thus reducing the lifespan. Ice accretion on the blade over an extended period increases the airfoil’s mass, and can cause power reduction of up to 80% [10]. The reduction in power production also depends on the frequency of icing events in the region [16]. Ice accretion on the surface is affected by the duration in which the icing occurs. In anti-icing and de-icing systems, the heating element is mostly installed on the leading edge where most ice accumulates [17], and the accretion on the leading edge is greatly affected by the angle of attack and accretion time.

Research on wind turbines and on the impacts of icing poses challenges with limited resources, such as the use of drones, and Supervisory Control and Data Acquisition (SCADA) was employed due to the complexity of identifying real-time icing on the blades [15]. Ice accumulation experiments on wind farms are costly and have operational difficulties; thus, the use of numerical simulations has increased compliance. The numerical approach conveniently provides information on aerodynamics and predicts energy production losses due to icing. A laboratory setup is applicable to estimate the amount of ice accretion after reproducing the icing conditions, assuming that conditions do not vary during the experiment. Numerical models on ice accretion involve complex flow simulation on the airfoil, boundary layer characteristics and water droplet behavior, and iced surface thermodynamics with phase changes. Softwares used for modeling wind turbine and aeronautical icing applications include TURBICE, FENSAP ICE, and LEWICE. Virk et al. [18] used TURBICE software to numerically simulate the effects of ice accretion near the tip on the NACA 64618 blade profile by varying the angle of attack from -5 to 7.5 °C. The airflow around the airfoil impacted the ice formation on the leading-edge surface with lower angle of attack having less ice. Kollar & Mishra [16] numerically studied the icing on wind turbine blade sections under adverse weather conditions with Matlab. Fu & Farzaneh [19] developed a computational fluid dynamics model on rime ice accretion on a 450-kW/S809 horizontal axis wind turbine. Hildebrandt & Sun [20] carried out a comparative numerical assessment on the impact of short icing events of five 2 hour scenarios with varied atmospheric conditions on a 1.5 MW turbine and compared the icing rate on stalled turbine and a rotating turbine using ANSYS FLUENT.

This study applies the numerical approach for modelling icing over a wind turbine blade section using FENSAP-ICE. The ice accretion on the bare and the iced blade is simulated, and the corresponding aerodynamic coefficients (lift and drag) and the loads of ice (mass) are compared. The results obtained provide information on the extent of aerodynamic degradation due to icing and disturbance of flow over the airfoil by accreted ice. The results will help determine airfoil shape with minimal ice accretion and improved lift, which would benefit the wind power industry and the energy production under extreme weather conditions.

## 2. Methodology

### 2.1. Geometry and mesh

Numerical simulations were carried out on the NACA2412 airfoil section with a 1 m chord length to analyze the icing growth effect by varying LWC, angle of attack (AoA), and accretion time on a rectangular topological domain. Numerical simulation is performed by applying the computational fluid dynamics (CFD) software FENSAP-ICE, where the airflow is modeled, and the aerodynamic perfor-

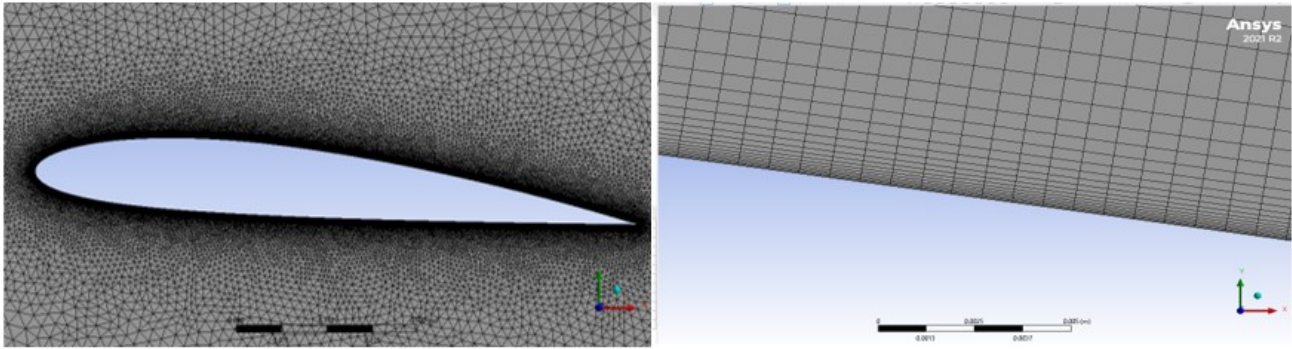


Figure 1. Meshing around the airfoil and the first layers enlarged

mance is evaluated for both bare and iced profiles. Unstructured (triangular) and semi-structured meshes were applied to the computational domain and the near wall region (airfoil). The resulting grid has elements within the boundary layer suitable for no-slip conditions around the airfoil. The no-slip boundary condition near the airfoil surface with a  $y^+$  value less than 1 is obtained using a Cadence calculator [21] because we will use a low-Re model. The first layer thickness is determined to be  $1.43 \cdot 10^{-5}$  m, and 27 layers are inserted with growth rate of 1.08%, the growth rate in the domain of triangular mesh was set to 1.05% as shown in Fig. 1.

**2.2. Flow conditions and boundary conditions**

The density of air and droplets are set to be  $1.394 \text{ kg/m}^3$  and  $1000 \text{ kg/m}^3$ , respectively, while the ice density was kept constant at  $917 \text{ kg/m}^3$  with air static pressure set at 1013.25 hPa and air temperature of  $-20 \text{ }^\circ\text{C}$ , with  $-18 \text{ }^\circ\text{C}$  on the airfoil surface (wall). Boundary conditions are shown in Fig. 2. The flow conditions were set in the inlet to freestream velocity at 20 m/s, whereas to pressure coupled at 0 atm in the outlet. On the boundary domains top and bottom the command "symm" is applied to consider linear symmetry. The model describes continuous fluid motion involving phase properties changes (liquid to solid, i.e., water droplets in the airflow over the airfoil surface to ice formation). The numerical simulation predicts the accretion of ice on the blade surface by considering successive water droplet trajectories hitting the surface, followed by airflow calculation on the surface, and energy and mass conservation (heat balance) with the water droplets simulated over the object freezing. The water droplets simulated over the object may freeze or evaporate. The heat balance in the thermodynamic model includes droplet heating, and heat contained in the water flowing on the blade, convection, radiation and evaporation [22]. These conditions were considered

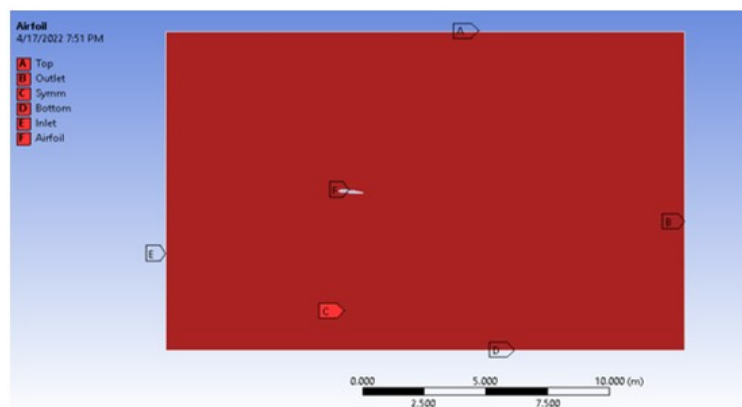
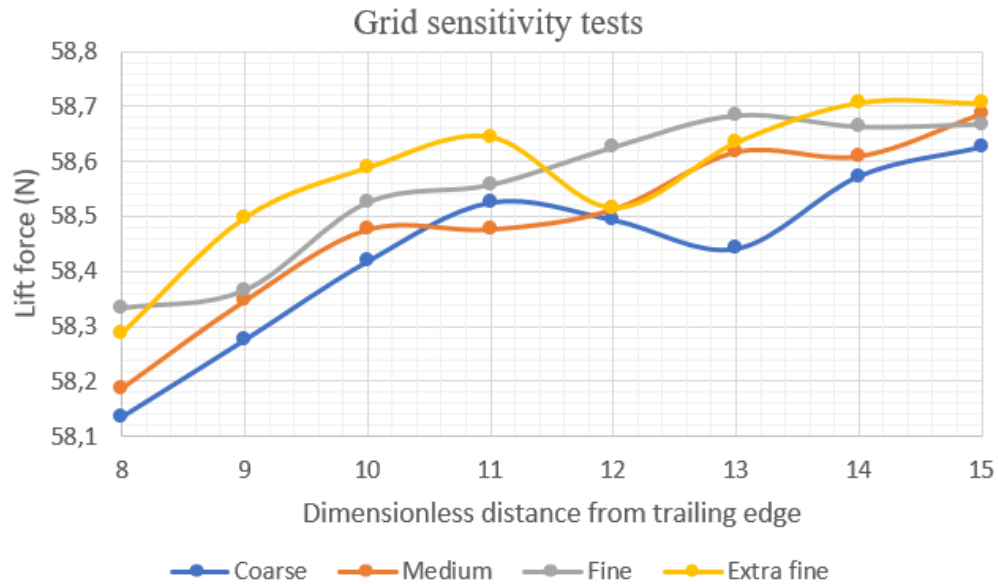


Figure 2. Boundary conditions on the rectangular computational domain

**Table 1.** Operating parameters of Airfoil NACA 2412

Parameter	Value
Temperature [°C]	-20
Velocity [m/s]	20
MVD [ $\mu\text{m}$ ]	20
DSD	Langmuir D
LWC [ $\text{g}/\text{m}^3$ ]	0.5; 1; 1.5
Exposure time [mins]	7; 20; 40; 60; 120; 180
AoA [°]	0; 5; 10; 15; 20

by the FENSAP ICE software. The turbulence model used is the  $k-\omega$  SST model since it provides a better prediction of flow separation and exhibits less sensitivity to flow outside the boundary layer than other turbulence models. The effects of angle of attack, liquid water content (LWC), and accretion/exposure time on icing and the aerodynamic performance are simulated using FENSAP-ICE. The range of these parameters is shown in Table 1. The impact of size of the droplets hitting the accreting surface is important on the ice accretion. However, the range of droplet sizes that the Langmuir D distribution covers is relatively small; therefore, the consideration of this distribution in the model instead of the MVD had little effect on the ice accretion [23]. The parameters used in the study represented the normal working conditions experienced in real life scenario, with some being simplified to controlled natural environments though they vary from time to time such as LWC and temperature [24]. The droplets were assumed to be spherical, and the forces acting on the droplets were inertia and drag.



**Figure 3.** Mesh sensitivity analysis on Lift force ( $N$ ) with varying lengths of computational domain behind airfoil trailing edge. The distance from the trailing edge is non-dimensionalized with the chord length

**2.3. Grid independence and boundary sensitivity tests**

Grid independence tests aim to obtain the optimal mesh and size of the computational domain considering accuracy and computational cost. The angle of attack had little impact on the mesh, the number of elements for fine mesh ranges from 502700 to 501710 for 0° to 20° AoA, respectively.

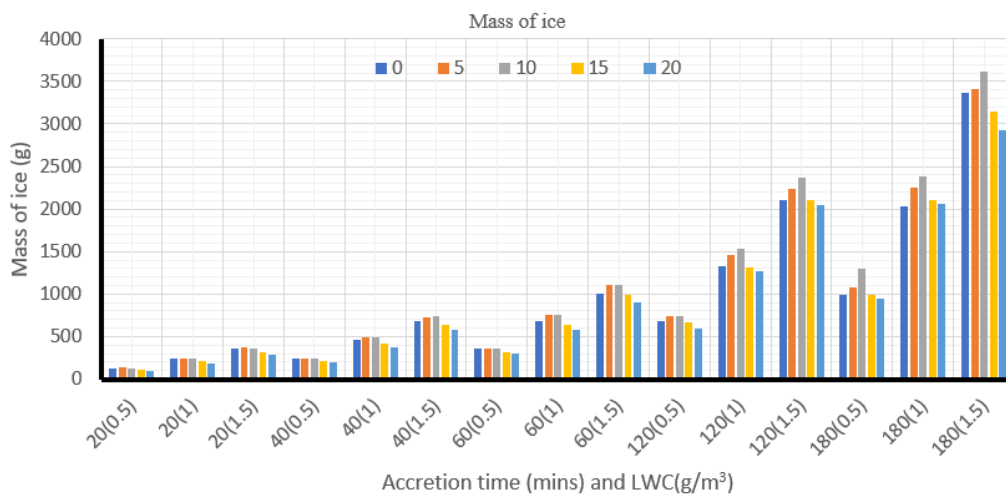
The grid sensitivity analysis is based on the aerodynamic performance by considering the lift force for varying lengths of computational domain behind the trailing edge. According to the analysis shown in Fig. 3, the distance behind the trailing edge does not significantly affect the lift force if it is within the recommended range, i.e., 10-15 times the chord length. The lift force obtained is between 58.15 N and 58.7 2N when the length of the computational domain behind the trailing edge varies between 8 and 15 times the chord length. The fine mesh was used with 14 m behind the trailing edge in the study since the value of lift force changed by 0.05% only when the size behind the trailing edge was increased from 14 m to 15 m.

**3. Results and discussion**

The effects of LWC, accretion time and angle of attack on ice mass and aerodynamic performance are examined.

**3.1. Effects of LWC, accretion time and angle of attack on the mass of ice accretion**

Mass of ice accreted was determined for accretion times of 7, 20, 40, 60,120 and 180 minutes, LWCs of 0.5 g/m<sup>3</sup>, 1.0 g/m<sup>3</sup> and 1.5 g/m<sup>3</sup>, and AoA of 0°, 5°, 10°, 15° and 20° (see Table 1). Figure 4 shows the effects of LWC, accretion time and angle of attack on the mass of ice accretion. Ice accretion is greatly affected by the angle of attack, with a lower angle causing the ice to accumulate mainly on the leading edge. In contrast, the higher angle of attack causes ice to accrete even at the trailing edge. The comparison shows the highest accretion mass at 10°, and the lowest at 20° angle of attack for all the LWCs considered. Ice accretion on the blade is also affected by the quantity of liquid water in the air. Increasing LWC means a higher amount of water in the atmosphere leading to a greater mass of ice accretion. Ice mass increases with LWC and increases exponentially with accretion time. The highest mass of ice obtained in 180 min is 3620 g at 10° and at 1.5 g/m<sup>3</sup> and the lowest mass is 940 g at 20° and at 0.5 g/m<sup>3</sup>.



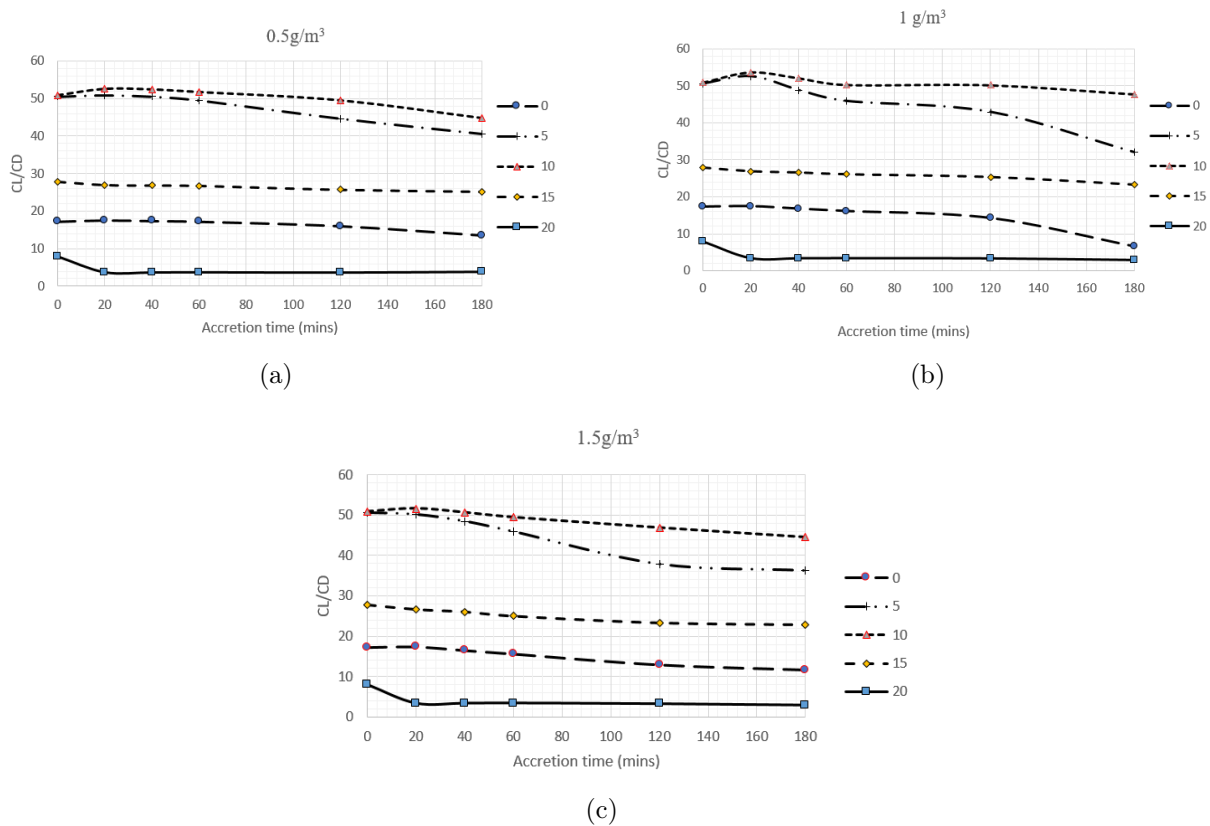
**Figure 4.** Effect of Liquid Water Content(g/m<sup>3</sup>), accretion time (min) and angle of attack (°) on the mass of ice accretion (g)



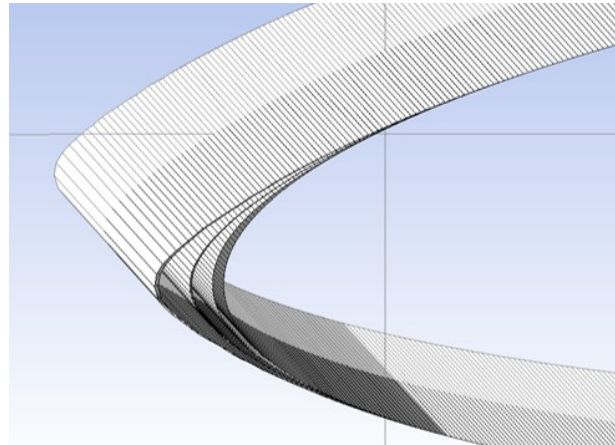
**3.2. Variation of CL/CD with accretion time**

The aerodynamic performance of the airfoil will be evaluated via the ratio of lift and drag coefficients, CL/CD with Figure 5 showing the impact of ice accretion time. The CL/CD slightly increases before 20 minutes for angles of attack 10° and below due to increase in the stagnation point and airfoil shape from ice accretion distorting disturbance of flow distribution. This change is about 3.29%, 5.43%, and 1.48% for LWC of 0.5g/m<sup>3</sup>, 1 g/m<sup>3</sup>, and 1.5 g/m<sup>3</sup>, respectively, for the 10° angle of attack. The comparison of the iced shapes in Figure 6 shows that ice on the leading edge raises the stagnation point after 20 minutes of accretion, enhancing the aerodynamic performance, which eventually degrades with further accretion. The highest CL/CD is 52.55, 53.65 and 51.63 for LWC of 0.5 g/m<sup>3</sup>, 1 g/m<sup>3</sup> and 1.5 g/m<sup>3</sup>, respectively, as it can be seen on the curve fitted on the data for 10° angle of attack. The CL/CD for small angle of attack between 0° to 10° increased slightly to about 20 minutes before it starts decreasing. For higher angle of attack (>10°), the CL/CD dropped immediately when ice started to accumulate on the surface, followed by a decreasing tendency. At 20° angle of attack, with minimal ice accretion on the surface after 20 minutes accretion, the CL/CD decreased by 53.38%, 57.41%, and 57.50% for LWC of 0.5 g/m<sup>3</sup>, 1 g/m<sup>3</sup> and 1.5 g/m<sup>3</sup>, respectively, as compared to the bare blade.

The ice accretion on the asymmetrical airfoil surface moves the stagnation point upward. Asymmetrical airfoils have a stagnation point slightly below the leading edge. Thus, with minimal icing on the surface, the stagnation point moves toward the upper surface, causing a slight increase in the CL/CD (see Fig. 5). Considering that the airfoil used in the study (NACA2412) had asymmetrical characteristics, the horizontal flow velocity hits the stagnation point slightly above the suction surface of the airfoil. Slight ice accretion on the surface raises the suction surface nearly to the stagnation

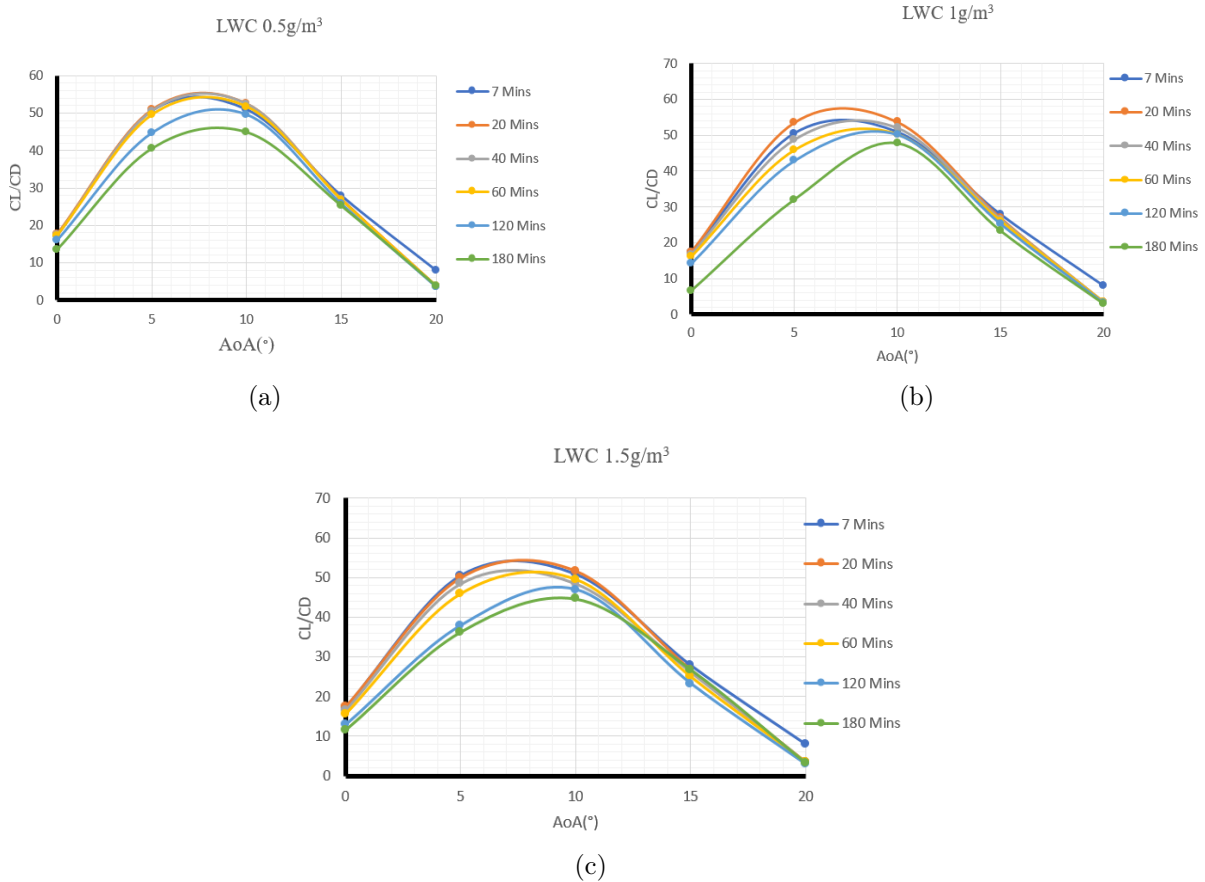


**Figure 5.** Variation of CL/CD with accretion time for different values of angle of attack and LWC



**Figure 6.** Accreted ice on the surface at 0°, 1 g/m<sup>3</sup> at 7,20 and 40 mins

point at lower accretion time and thus increases the CL/CD. According to the comparison presented on Fig. 6 for 0°, the accretion surface between the 7th and 40th minute shows that little change in the streamlines caused slight icing. Increasing angle of attack increment moves the stagnation point next to the suction surface and thus decreases the CL/CD.



**Figure 7.** Variation of CL/CD with the angle of attack (°) for different values of accretion time (mins) and LWC (g/m<sup>3</sup>)

### 3.3. Variation of CL/CD with the angle of attack

Fig. 7 shows the variation of CL/CD with the angle of attack for different accretion times and LWC. The ratio CL/CD for a bare airfoil is greatest for angles between  $5^\circ$  and  $10^\circ$ , and this tendency does not change for iced blades, but the value of this ratio is smaller for iced blades. This observation corresponds to those in [25]. Moreover, a greater decrease of CL/CD may be observed after a long accretion time for smaller values of angle of attack (below  $10^\circ$ ). With the increase in LWC, more ice accumulation leads to greater CL/CD ratio reduction. The maximum of CL/CD is 53.52 for LWC of  $0.5 \text{ g/m}^3$ , whereas its highest value is 51.63 for  $1.5 \text{ g/m}^3$ .

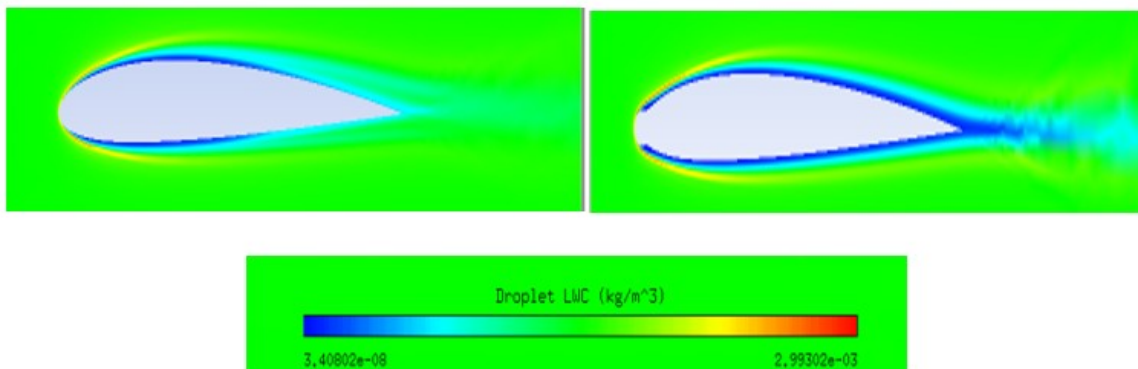
### 3.4. Velocity distribution around an iced airfoil

The flow distribution over the airfoil is dependent on the angle of attack. At a lower angle of attack, the Kutta condition was met, while at a higher angle of attack, the separation zone moved upward towards the leading edge with vortices occurring at the trailing edge. Fig. 8 and 9 show the impacts of icing and varying angle of attack on the velocity distribution. Icing causes changes in airfoil shape, impacting on flow distribution, which can be observed due to the multi-shot simulations. Figure 8 shows the iced shapes at zero angle of attack, during the simulation of 3 hours accretion time and the impact caused by icing after the 3rd (minimal separation, 108 min) and the 5th shot (turbulent regions develop, 180 min) at LWC of  $1.5 \text{ g/m}^3$ . After further shots, the flow over the airfoil starts separating and causes some difficulty in the reattachment in the regions near the trailing edge, so that recirculation occurs.

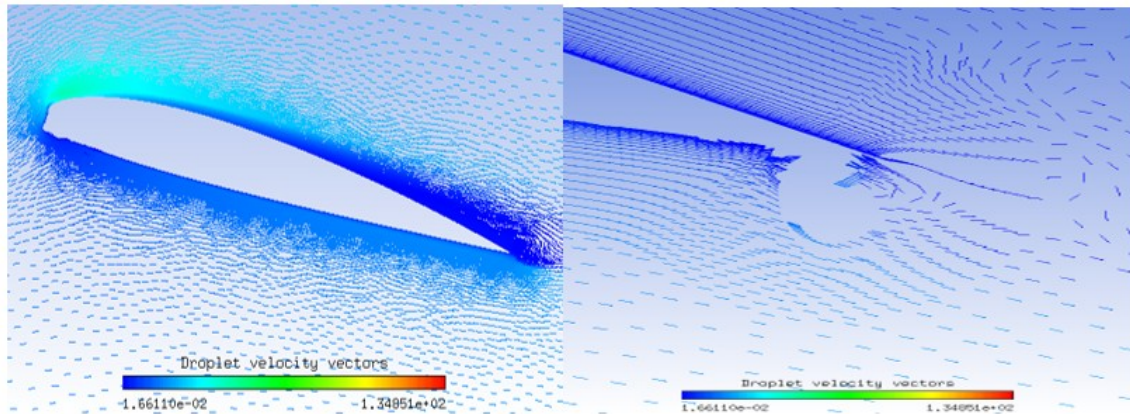
Higher angle of attack led to vortices forming near the leading edge even for less amount of ice. The arrows near the trailing edge in Fig. 9 show the vortices in the recirculation region caused by the flow separation, and the vortices occur where arrows are missing. The backflow may influence droplet motion on the surface and freezing time, but further study is needed for a more profound description of this process.

## 4. Conclusions

The effects of ice accretion on the aerodynamic performance of an airfoil section have been examined under different ambient conditions. Icing of a NACA2412 airfoil was simulated numerically, and the lift and drag coefficients on the iced airfoil were calculated with varying LWC, accretion time and angle of attack. The aerodynamic performance was evaluated by comparing the ratio of lift and drag coefficients CL/CD obtained after different accretion times. The reduction of CL/CD was



**Figure 8.** Effect of accretion time on ice shape and velocity distribution at  $0^\circ$  AoA and LWC of  $1.5 \text{ g/m}^3$  in the simulation of 180 minutes accretion time at 3rd shot (108 min) and 5th shot (180 min)



**Figure 9.** The flow distribution over the airfoil(left) and backflow (recirculation) at the trailing edge (right) at  $10^\circ$  AoA and LWC of  $1.5 \text{ g/m}^3$

observed on the asymmetric shape of the airfoil after about 20 minutes of accretion time. However, a short enough accretion time, i.e. less than 20 minutes, may lead to a slight increase of the ratio  $CL/CD$ , because the stagnation point moves toward the upper surface making the airfoil to become more streamlined. LWC and angle of attack also influences the aerodynamic performance, mass of accreted ice and the velocity distribution over the airfoil surface. The higher LWC results in increased mass of accreted ice, and consequently, aerodynamic performance degradation. The mass of ice increased exponentially with accretion time. Increasing the angle of attack caused more ice to form on the lower surface and the flow separation region on the upper surface increased towards the leading edge. According to the results presented in the study, slight altering of the airfoil shape may increase aerodynamic performance making the wind turbine possible to work under adverse atmospheric conditions.

## 5. Acknowledgement

Project no. TKP2021-NVA-29 has been implemented with support from the Ministry of Innovation and Technology of Hungary from the National Research, Development and Innovation Fund, financed under the TKP2021-NVA funding scheme.

## 6. References

- [1] N. Dalili, A. Edrisy, R. Carriveau, *A review of surface engineering issues critical to wind turbine performance*, Renewable and Sustainable Energy Reviews 13(2), 2009. pp. 428–438, [CrossRef](#)
- [2] D.L. Johnson, R.J. Erhardt, *Projected impacts of climate change on wind energy density in the United States*, Renew Energy 85, 2016, pp. 66–73, [CrossRef](#)
- [3] A.G. Kraj, E.L. Bibeau, *Phases of icing on wind turbine blades characterized by ice accumulation*, Renew Energy 35(5), 2010, pp. 966–972, [CrossRef](#)
- [4] P. Blasco, J. Palacios, S. Schmitz, *Effect of icing roughness on wind turbine power production*, Wind Energy 20(4), 2017, pp. 601–617, [CrossRef](#)
- [5] F. Afzal, M. S. Virk, *Review of Icing Effects on Wind Turbine in Cold Regions*, E3S Web of Conferences 72, 2018, p. 01007, [CrossRef](#)

- [6] F. Martini, L.T. Contreras Montoya, A. Ilinca, *Review of Wind Turbine Icing Modelling Approaches*, *Energies* (Basel) 14(16), 2021, p. 5207, [CrossRef](#)
- [7] A. Ilinca, *Analysis and Mitigation of Icing Effects on Wind Turbines*, in *Wind Turbines*, 2011, pp. 177–214, [CrossRef](#)
- [8] J.G. Pallarol, B. Sunden, Z. Wu, *On Ice Accretion for Wind Turbines and Influence of Some Parameters*, In R. S. Amano & B. Sundén (Eds.), *Aerodynamics of Wind Turbines: Emerging Topics*, 2014, pp. 129–159, [CrossRef](#)
- [9] L.T. Contreras Montoya, S. Lain, A. Ilinca, *A Review on the Estimation of Power Loss Due to Icing in Wind Turbines*, *Energies* (Basel) 15(3), 2022, p. 1083, [CrossRef](#)
- [10] L. Gao, H. Hu, *Wind turbine icing characteristics and icing-induced power losses to utility-scale wind turbines*, *Proceedings of the National Academy of Sciences* 118(42), 2021, p. e2111461118, [CrossRef](#)
- [11] M.C. Homola, M.S. Virk, P.J. Nicklasson, P.A. Sundsbø, *Performance losses due to ice accretion for a 5 MW wind turbine*, *Wind Energy* 15(3), 2012, pp. 379–389, [CrossRef](#)
- [12] R. Luo, X. Chen, J. Guo, *Design of deicing device for wind turbine blade based on microwave and ultrasonic wave*, *Journal of Physics: Conference Series* 1748 (6), 2021, p. 062018, [CrossRef](#)
- [13] O. Yirtici, I.H. Tuncer, S. Ozgen, *Ice Accretion Prediction on Wind Turbines and Consequent Power Losses*, *Journal of Physics: Conference Series* 753, 2016, p. 022022, [CrossRef](#)
- [14] O. Yirtici, I.H. Tuncer, *Aerodynamic shape optimization of wind turbine blades for minimizing power production losses due to icing*, *Cold Regions Science and Technology*, 185, 2021, 103250, [CrossRef](#)
- [15] X. Dong, D. Gao, J. Li, Z. Jincan, K. Zheng, *Blades icing identification model of wind turbines based on SCADA data*, *Renew Energy* 162, 2020, pp. 575–586, [CrossRef](#)
- [16] L. E. Kollar, R. Mishra, *Inverse design of wind turbine blade sections for operation under icing conditions*, *Energy Convers Management* 180, 2019, pp. 844–858, [CrossRef](#)
- [17] C. Montoya, L. Tatiana, S. Lain, A. Ilinca, *A Review on the Estimation of Power Loss Due to Icing in Wind Turbines*, *Energies* 15(3), 2022, [CrossRef](#)
- [18] M.S. Virk, M.C. Homola, P.J. Nicklasson, *Relation Between Angle of Attack and Atmospheric Ice Accretion on Large Wind Turbine’s Blade*, *Wind Engineering* 34(6), 2010, pp. 607–614, [CrossRef](#)
- [19] P. Fu, M. Farzaneh, *A CFD approach for modeling the rime-ice accretion process on a horizontal-axis wind turbine*, *Journal of Wind Engineering and Industrial Aerodynamics* 98(4–5), 2010, pp. 181–188, [CrossRef](#)
- [20] S. Hildebrandt, Q. Sun, *Evaluation of operational strategies on wind turbine power production during short icing events*, *Journal of Wind Engineering and Industrial Aerodynamics* 219, 2021, p. 104795, [CrossRef](#)
- [21] *Compute Grid Spacing for a Given  $Y^+$* , Accessed May 02, 2022, [CrossRef](#)

- [22] L. Makkonen, T. Laakso, M. Marjaniemi, K.J. Finstad, *Modelling and Prevention of Ice Accretion on Wind Turbines*, Wind Engineering 25(1), 2001, pp. 3–21, [CrossRef](#)
- [23] *ANSYS FENSAP-ICE Tutorial Guide*, ANSYS 18.2. 2017, [CrossRef](#)
- [24] L. E. Kollár, M. Farzaneh, *Modeling the evolution of droplet size distribution in two-phase flows*, International Journal of Multiphase Flow 33(11), 2007, pp. 1255–1270, [CrossRef](#)
- [25] B. Csöre, L. Kollár, D. Fenyvesi, *Jeges szárnyalak aerodinamikájának vizsgálata*, Mérnöki és Informatikai Megoldások|Engineering and IT Solutions, 2022, I, pp. 19–27, [CrossRef](#)

# CAD modelling of the chip shape in case of ball-end milling

Bálint Varga<sup>a,b\*</sup>, Balázs Mikó<sup>a</sup>

<sup>a</sup> Óbuda University, Doctoral School on Materials Sciences and Technologies

<sup>b</sup> Óbuda University, Institute of Material and Manufacturing Science

## ABSTRACT

The manufacturing of free form surfaces is a common task in the field of mould and die manufacturing. The changing circumstances of the finishing milling with ball-end milling cutter has effect on the shape and the volume of the chip, the load of the cutting tool and the generated surface roughness. The aim of the article is to investigate the changing of the chip thickness and volume in case of ball-end milling by 3D CAD modelling, and to analyse the changing of the circumstances in case of milling of a convex and a concave surfaces.

**Keywords:** *free form surface, ball-end milling, chip, CAD modelling, average chip thickness*

## 1. Introduction

In injection moulding tools, dies or in the manufacture of vehicle bodies, free-form surfaces are also encountered, and machining them requires high precision as well as productivity. In the field of mold and die production, these surfaces are basically made by milling, where finishing is done by a ball-end mill. During milling of a free-form surface with a ball-end mill, depending on the nature of the surface, the working edge section, the working diameter and thus the cutting conditions, the shape and volume of the chip, and the cutting force change continuously [1, 2]. This affects the load on the tool, the quality of the resulting surface, and the wear of the tool.

The volume of the chip in the case of milling can be determined as the multiplication of the cutting depth ( $a_p$ ), the cutting width ( $a_e$ ) and the cutting feed ( $f_z$ ):

$$V_c = a_p \cdot a_e \cdot f_z. \quad (1)$$

However, during machining with a ball end mill, the depth of cut and width of cut values differ from the nominal values due to the mentioned conditions. There are several methods for determining the shape and the volume of a chip.

Analytical description of the tool edge and surface enables the exact description of the chip shape, however, due to the consideration of the surface description and the tool edge, it requires complicated calculations [3, 4]. The volume of the chip can also be determined as the product of the feed per tooth and the orthogonal area of the chipped area [5]. This cutted surface segment can also be produced with a simplified geometrical description of the ball-end tool [6]. The variable location and size of this surface determines the required power, dynamic conditions, and surface roughness of machining with a ball end mill [2].

In addition to the analytical and geometric description, the chip shape can also be examined with CAD modelling [7]. The chip removal is simulated in a 3D virtual environment. The aim of

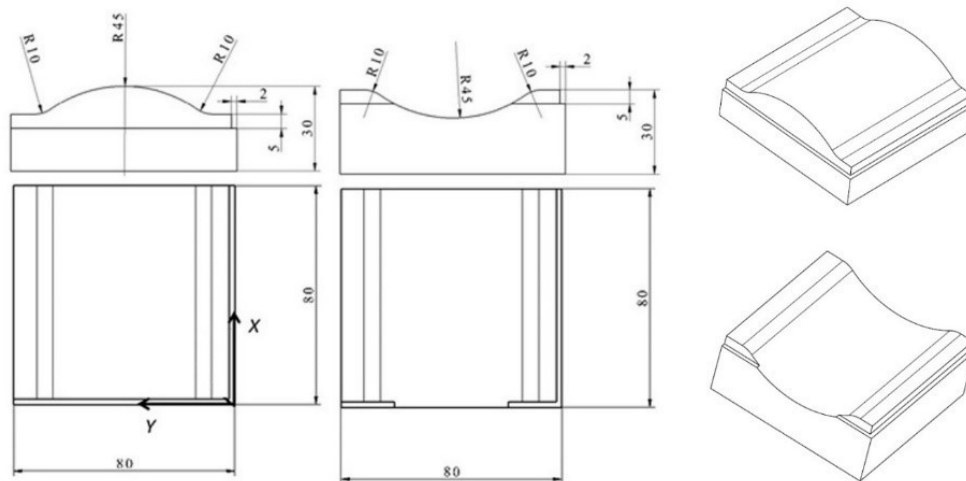


Figure 1. Geometric design of the test part

the research is to investigate the accuracy of surfaces machined with a ball-end mill, primarily to investigate the relationship between milling strategy and shape accuracy [8, 9]. The purpose of this is to be able to choose the appropriate milling strategy, taking into account the micro- and macro-accuracy of the surface, and to determine its technological and geometric parameters when using CAM systems.

The purpose of this article is to determine the shape and cross-section of the chip removed during surface milling with a ball end mill using 3D geometric modelling, and to analyze the change in the cutting conditions.

## 2. Method

The size of the test part is  $80 \times 80 \times 30$  mm, the tested free-form surface is a cylindrical surface with a radius of 45 mm. This surface is connected to the horizontal plane by a rounding with a radius of 10 mm. In order to examine the geometrical conditions, we also examined the geometry of convex and concave parts. The dimensions of the test part are shown in Fig. 1. The height and depth of the large cylindrical surface of the convex (convex - CX) and concave (concave - CV) part is 9.2 mm. The size of the test part was defined considering manufacturing and measuring aspects.

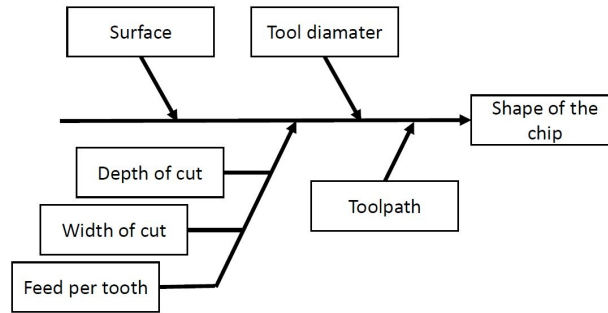
During the geometric modelling of the chip shape, the CATIA V5 CAD system was used. During the modelling, the factors influencing the chip shape were parameterized, so by changing them, the conditions of the chipping can be examined. The examined parameters are: the position ( $x, y$ ) of the tool diameter ( $D_c$ ), the surface normal, the tool feed ( $f_z$ ), the feed direction ( $A_f$ ), the cutting width ( $a_e$ ) and the cutting depth ( $a_p$ ).

During the simulation, we changed the value of the feed per tooth and the width of cut with several feed directions. The tool diameter was  $D_c = 10$  mm, the cutting depth was  $a_p = 0.3$  mm, and the direction of the surface normal is determined by the shape of the test piece and the current position of the tool.

Table 1. Cutting parameters

Parameter	1	2	3	4	5
$f_z$ [mm]	0.08	0.08	0.08	0.12	0.16
$a_e$ [mm]	0.35	0.25	0.15	0.15	0.15



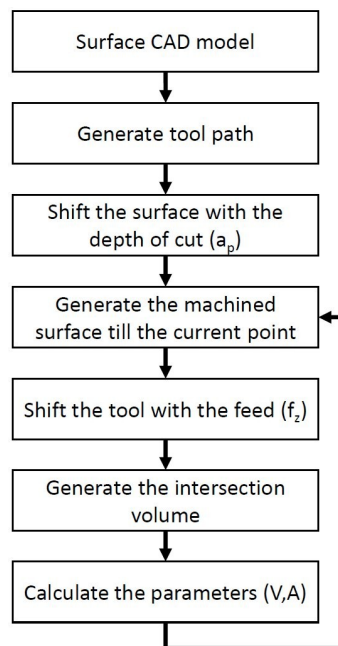


**Figure 2.** Factors determining the shape of a chip

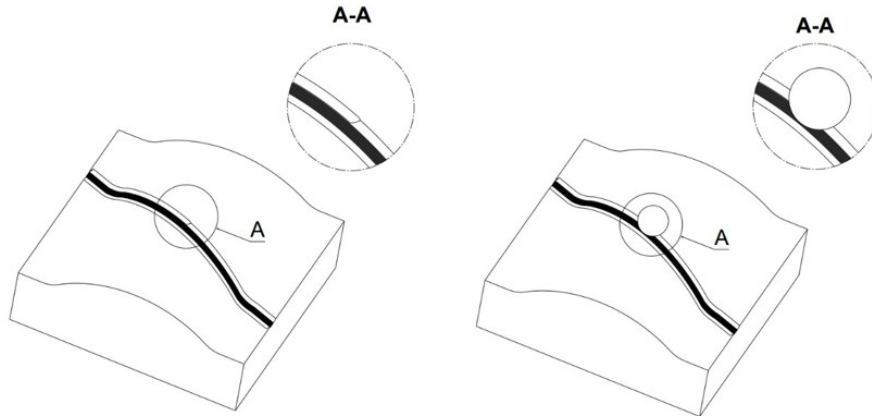
Based on the CAD model, the volume ( $V$ ) of the generated theoretical chip shape was determined, as well as the average chip thickness ( $h_m$ ) as a quotient of the volume and the surface area ( $A$ ) facing the direction of the tool. The values of the feed direction during modelling were  $0.0^\circ$ ,  $22.5^\circ$ ,  $45.0^\circ$ ,  $67.5^\circ$  and  $90.0^\circ$ . The values of feed and width of cut were examined in 5 sets according to [Table 1](#).

### 3. CAD modeling of the chip

During the geometric modelling, the goal was to create a parametric CAD model, which is suitable for determining the volume and cross-section of the resulting chip at any point of the surface model. For this, it is necessary to parameterize the tool position coordinates, as well as to consider additional parameters that determine the shape of the chip. These parameters are the depth of cut ( $a_p$ ), the lateral step (width of cut) ( $a_e$ ), the feed per tooth ( $f_z$ ), the angle of the milling direction ( $A_f$ ) and the diameter of the tool ( $D_c$ ) ([Fig. 2](#)). The modelling method focuses only the geometric circumstances, and cannot consider the effect of the tool edge geometry, the cutting speed and the mechanical properties of the workpiece and the tool. The modelling process was demonstrated on the convex piece. The modelling was performed at a thousandfold magnification due to the geometric resolution of the CAD system. The first step of the modelling is to shift the initial surface by the value of the depth of the cut ( $a_p$ ), which represents the pre-smoothed geometry ([Fig. 3](#)). The next step



**Figure 3.** The modelling process

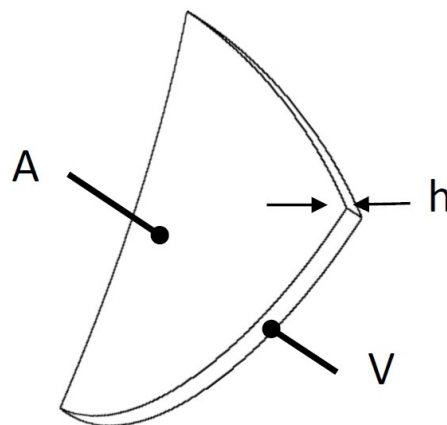


**Figure 4.** CAD model of the simulation

of the modelling is to parameterize the coordinate points of the toolpath. A hemisphere of a given diameter, representing the cutting tool, is traced along the toolpath constructed on the surface, thus touching the surface that is to be machined. The part of the material that has already been touched by the tool must then be removed up to the coordinate where the shape and parameters of the chip are determined (Fig. 4).

The figure on the left shows the surface already machined at the given coordinate. On the right, the same is shown with a symbolic representation of the tool in the tested position. The tool, i.e. the hemisphere, is offset along the toolpath by exactly the same amount as the feed per tooth. In the presented picture, not all toolpaths are visible due to the graphics capability of the computer, only the 20 toolpaths before the measuring point are shown, which are visible as a thick black line. This simplification does not affect the result. In the final step, only the common part of the two bodies, the tool and the machined surface, is created, resulting in the geometric model of the chip shown in Fig. 5.

The test involved modelling the chips at 21 points on both workpieces. At these points, the surface normal is always in a different direction, varying continuously from  $0^\circ$  to  $33^\circ$  in one direction ( $y$ ) only, due to the surface to be machined. The positions of the test points are shown in Fig. 6. A total of 1050 chip shapes were defined in the modeling.



**Figure 5.** Modelled chip shape

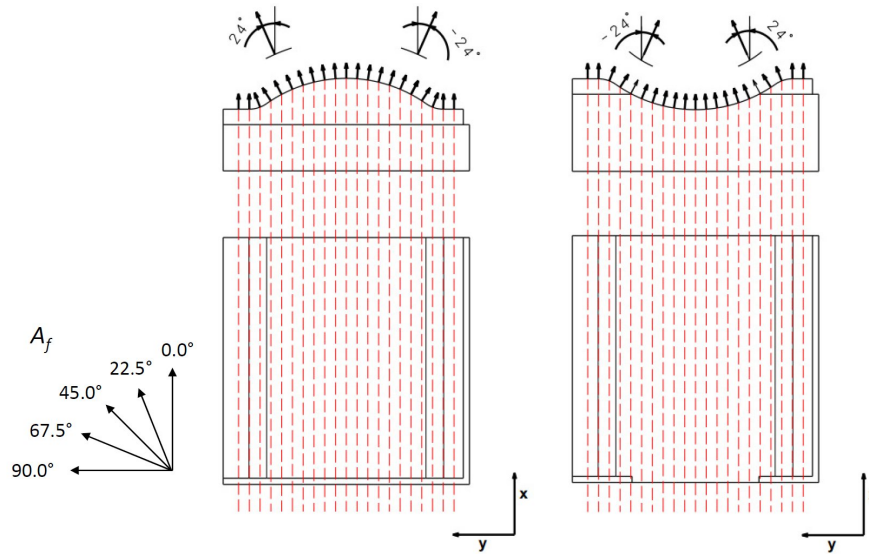


Figure 6. Tool positions investigated in the modelling

4. Results

The CAD simulation of the chip removal shows that the chip volume and chip thickness change along the path due to surface variation, and that this variation is different for the concave (CV) and convex (CX) pieces. At the horizontal sections (points 1 and 21), the chip volume is equal to the theoretical value given by Eq. (1). Fig. 7 shows the variation for the parameters at  $f_z = 0.12$  mm and  $a_e = 0.15$  mm.

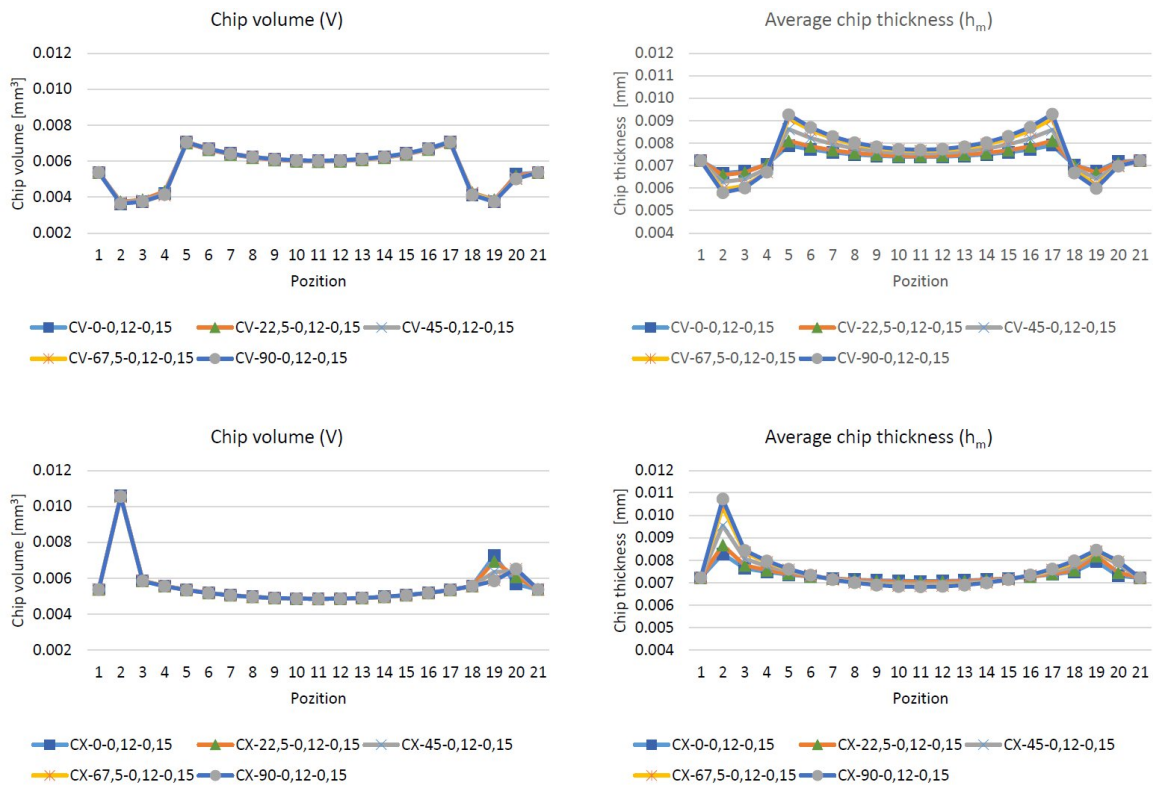
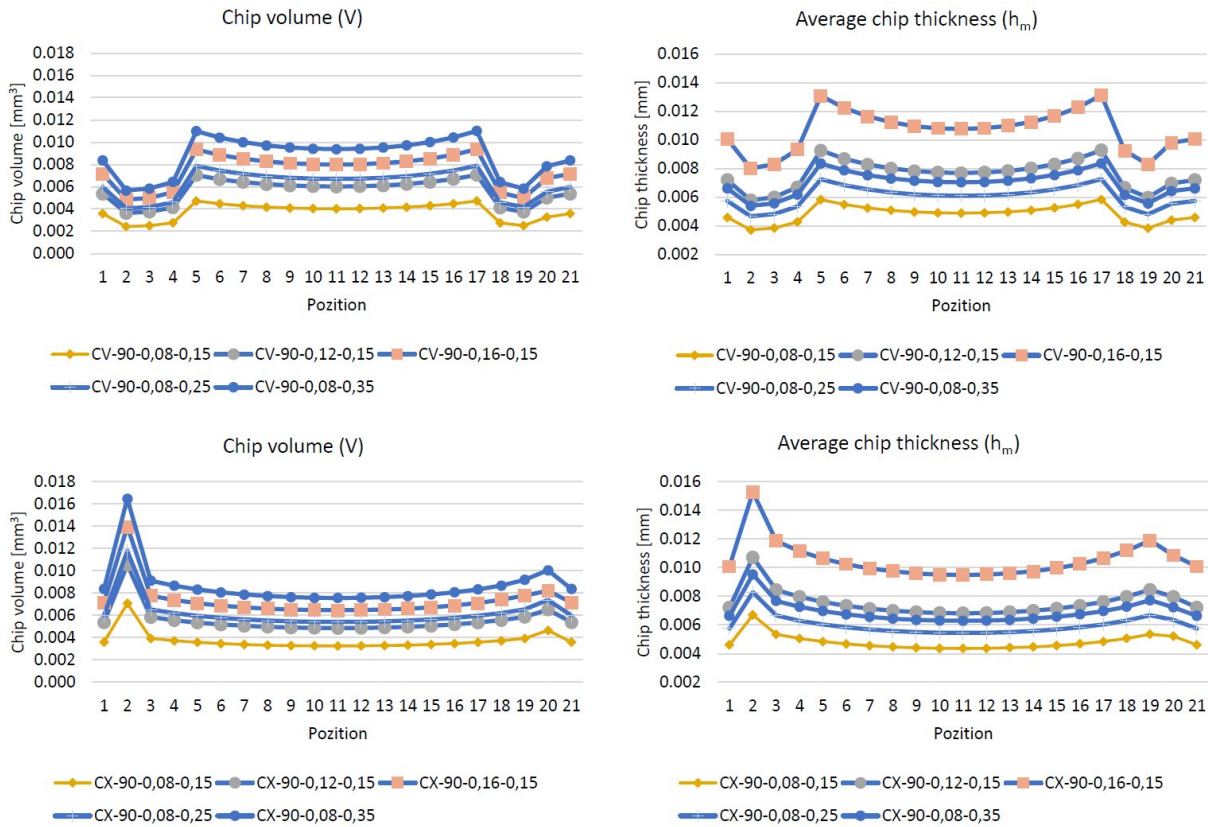


Figure 7. Variation of chip volume and mean chip thickness as a function of milling direction



**Figure 8.** Variation of chip volume and mean chip thickness as a function of milling parameters for 90° milling direction

The nature of the curves is different at convex and concave surfaces, as more of the tool is in contact with the surface when milling a concave surface. For concave surfaces, the chip volume is larger on the R45 curved section. As can be seen, the chip volume and chip thickness curves are not symmetric, so the chip volume and mean thickness are different in the straight and curved (R10) sections of the inlet and outlet. In the case of a concave (CV) surface, the inlet and outlet radius is convex, reducing the chip volume. For the convex surface (CX), the radius is concave, so there is a large increase. The rate of increase depends on the relationship between the surface radius and the tool radius. The increase is smaller at the outlet section. Since a different section of the tool contacts the surface on either side of the test surface, the volume of the chip is also different.

For the chip volume, the curves are nearly coincident, so the value does not depend on the milling feed direction. However, the values for the mean chip thickness differ, so the milling direction affects its value. The diagram shows that the mean chip cross-section is smallest at  $A_f = 0$  and largest at  $A_f = 90$ . The deviation is smaller for the convex (CX) surface.

The effect of feed per tooth and width of cut is shown in Fig. 8 for a 90° milling direction. As can be seen, the curves are similar. The smallest chip volume there is at  $f_z = 0.08$  mm,  $a_e = 0.15$  mm, the largest at  $f_z = 0.08$  mm,  $a_e = 0.35$  mm, so the role of the width of cut ( $a_e$ ) is more important. The average chip thickness there is at  $f_z = 0.16$  mm,  $a_e = 0.15$  mm, where the feed per tooth ( $f_z$ ) plays a more important role.

Further tests will only analyse data for the R45 mm curved section. Fig. 9 shows the average values of the simulations with the given parameters  $f_z$  and  $a_e$ . They show that in case of the concave (CV) surface, both chip volume and mean chip thickness are larger. In the case of volume, the width of cut has a greater effect, and in the case of chip thickness, the feed rate has a greater effect.

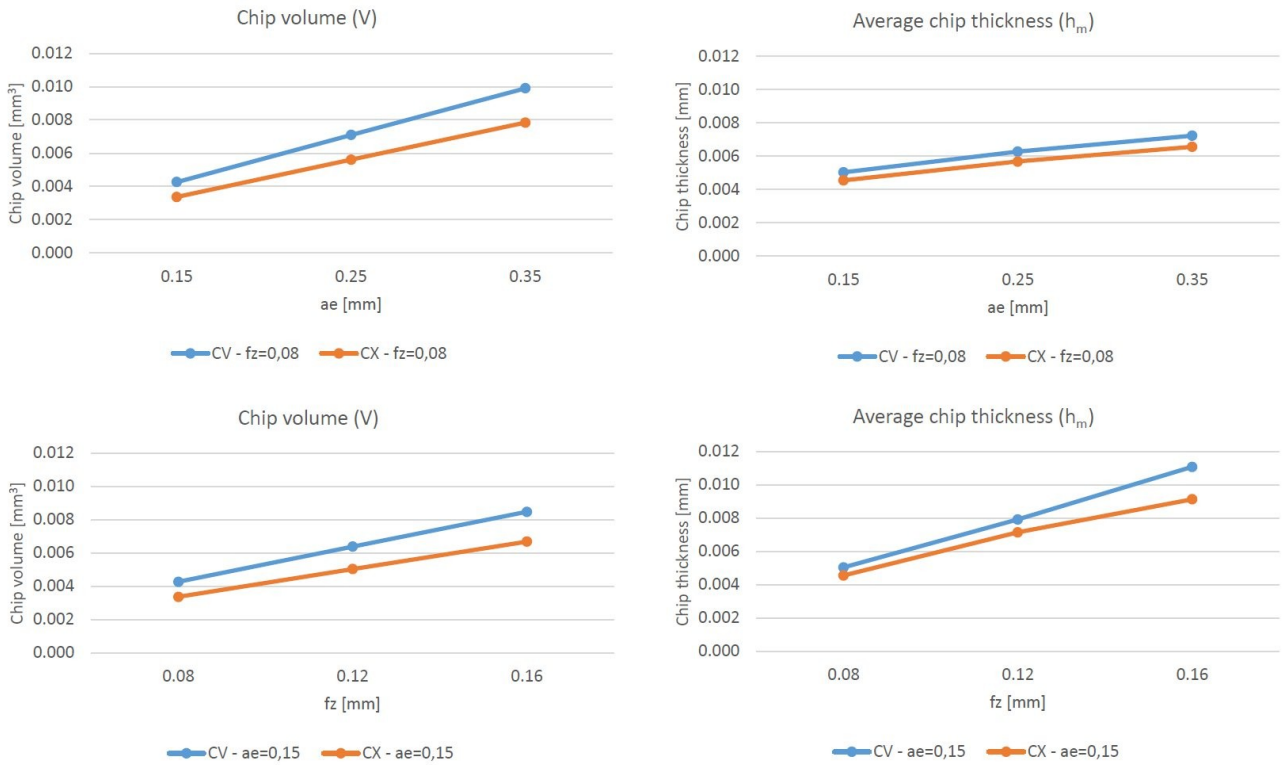


Figure 9. Average values on the curved (R45) section

Fig. 10 and 11 show the average values for milling with the given parameters in the given direction. They show that the average value of the chip volume is not sensitive to the milling direction and higher for concave surfaces. The value of the standard deviation, which indicates the variation along

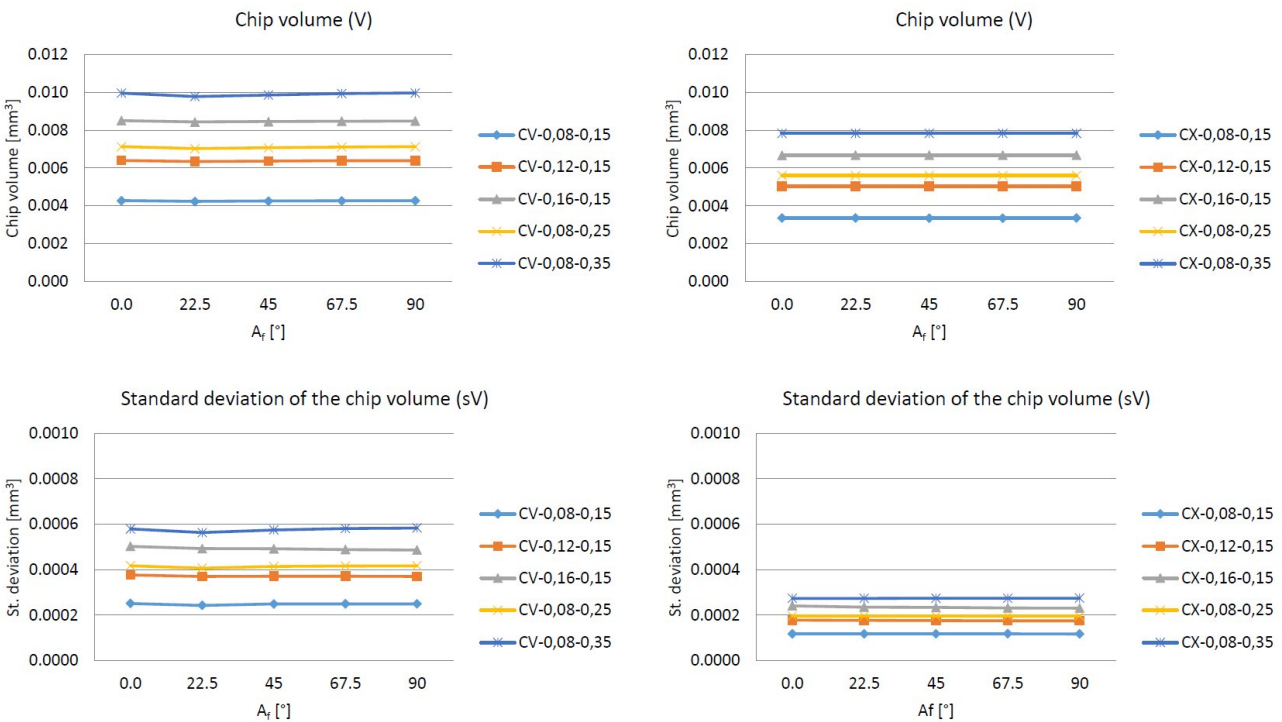
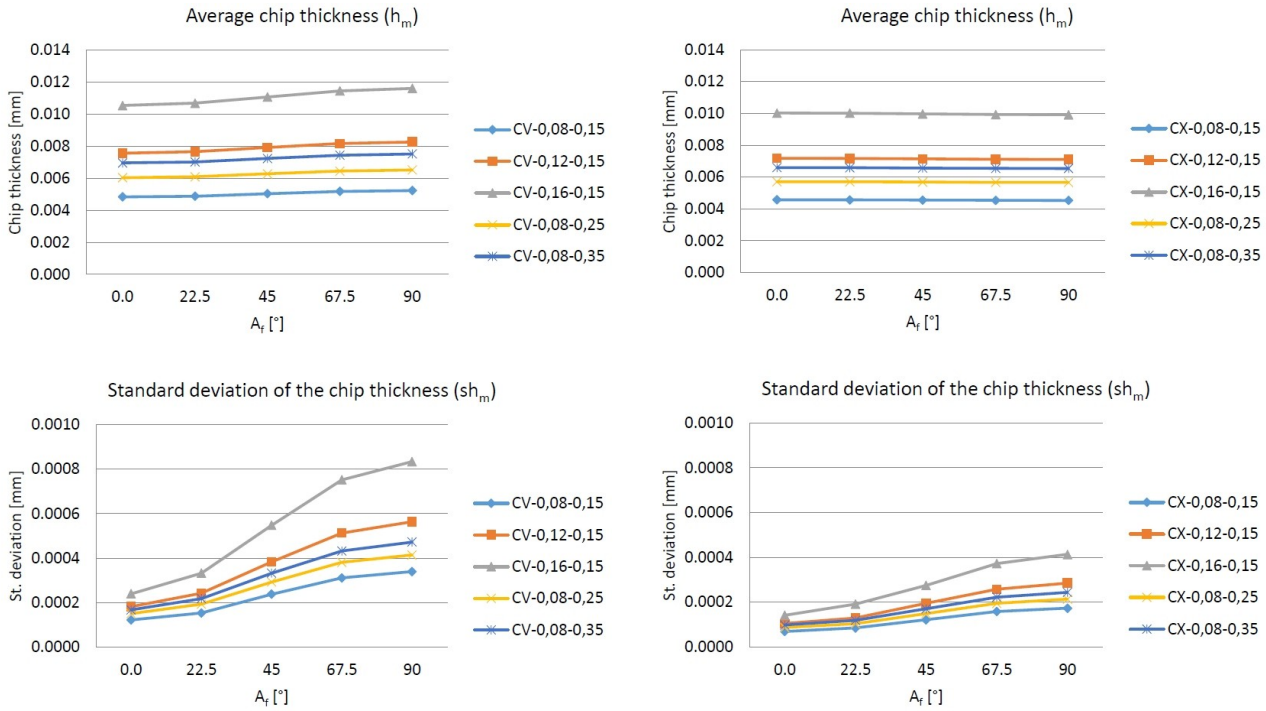


Figure 10. Mean and standard deviation of chip volume by milling direction



**Figure 11.** Mean and standard deviation of average chip thickness by milling direction at R45

the path, is also insensitive to the milling direction, being larger for concave (CV) surfaces and smaller for convex surfaces (CX), i.e. the chip volume varies less along the path for convex surfaces. The average values of the mean chip thickness (Fig. 11) show a small increase with the change in milling direction for the concave (CV) surface, while there is no effect when milling the convex surface. On the other hand, the standard deviation values of the mean chip thickness along the tool path vary significantly with the direction of the path, with the smallest variation at 0° and the largest variation at 90°. The variation is larger for a concave surface than for a convex surface.

### 5. Conclusions

When finishing a free-form surface with a ball-end milling cutter, the conditions of chip removal are constantly changing as the surface changes, affecting the tool load and the micro and macro accuracy of the surface. In case of concave and a convex free-form surfaces machined with a ball-end milling cutter, the shape, volume and average thickness of the chip were investigated by CAD simulation.

Based on the simulations, it was found that (1) the theoretical turning volume agrees with the simulation values only in the horizontal sections; (2) for concave and convex surfaces, the chip volume and mean thickness vary differently; (3) for concave pieces, the chip volume is larger under the same conditions; (4) for chip volume, the width of cut has a greater effect, for chip thickness, the feed rate has a greater effect; (5) the mean value and variance of the chip volume are not sensitive to the milling direction; (6) the average value of the mean chip thickness is only slightly sensitive to the milling direction, but the variation along the path (standard deviation) is significant. The presented method also provides the possibility to study the tool load variation, to select the appropriate milling strategy and to determine the theoretical roughness.

## 6. References

- [1] T. Altan, B Lilly, Y.C. Yan, *Manufacturing of dies and moulds*, CIRP Annals - Manufacturing Technology 50(2), 2001, pp. 404-422, [CrossRef](#)
- [2] C.K. Toh, *A study of the effects of cutter path strategies and orientations in milling*, Journal of Materials Processing Technology 152, 2004, pp. 346–356, [CrossRef](#)
- [3] L. Sai, R. Belguith, M. Baili, G. Dessenin, W. Bouzid, *An approach to modelling the chip thickness and cutter workpiece engagement region in 3 and 5 axis ball end milling*, Journal of Manufacturing Processes 34 A, 2018, pp. 7–17, [CrossRef](#)
- [4] L. Sai, R. Belguith, M. Baili, G. Dessenin, W. Bouzid, *Cutter-workpiece engagement calculation in 3-axis ball end milling considering cutter runout*, Journal of Manufacturing Processes 41, 2019, pp. 74–82, [CrossRef](#)
- [5] T. Huang, X. Zhang, H. Ding, *Decoupled chip thickness calculation model for cutting force prediction in five-axis ball-end milling*, The International Journal of Advanced Manufacturing Technology volume 69, 2013, pp. 203-1217, [CrossRef](#)
- [6] A.F. de Souza, A.E. Diniz, A.R. Rodrigues, R.T. Coelho, *Investigating the cutting phenomena in free-form milling using a ball-end cutting tool for die and mold manufacturing*, The International Journal of Advanced Manufacturing Technology 71, 2014, pp. 565–1577, [CrossRef](#)
- [7] H. Iwabe, K. Shimizu, M. Sasaki, *Analysis of cutting mechanism by ball end mill using 3D-CAD*, JSME International Journal Series C 49(1), 2006, pp. 28-34, [CrossRef](#)
- [8] B. Mikó, B. Varga, W. Zebala, *The effect of the feed direction on the micro- and macro accuracy of 3D ball-end milling of chromium-molybdenum alloy steel*, Materials 12, 2019, 4038, [CrossRef](#)
- [9] B. Varga, B. Mikó, *Impact of different CAM strategies and cutting parameters on machining free-form surfaces with ball-end milling tool in terms of micro and macro accuracy*, Acta Polytechnica Hungarica 18(7), 2021, pp. 109-128, [CrossRef](#)

# Investigation of materials flow during the cold-rolling process by experimental evidence and numerical approaches

János György Bátorfi<sup>a,b\*</sup>, Gyula Pál<sup>a,b</sup>, Purnima Chakravarty<sup>a,b</sup>, Juriij Sidor<sup>a</sup>

<sup>a</sup> ELTE, Faculty of Informatics, Savaria Institute of Technology

<sup>b</sup> ELTE, Faculty of Science, Doctoral School of Physics

## ABSTRACT

In this paper, the modeling possibilities applicable to rolling processes were summarized, with particular reference to finite element models (FEM) and different flow-line models (FLM). The results of the analysis suggest that the different models are suitable for the study of deformation processes during cold rolling. Furthermore, the possibilities for the extension of the FLM model are summarized.

**Keywords:** *aluminum, cold rolling, FEM, flow-line model, material model, plastic deformation*

## 1. Introduction

Rolling means the plastic deformation of a sheet between rotating rolls, the thickness of the sheet is smaller after deformation than before it [1]. A simple geometrical drawing is shown in Fig. 1.

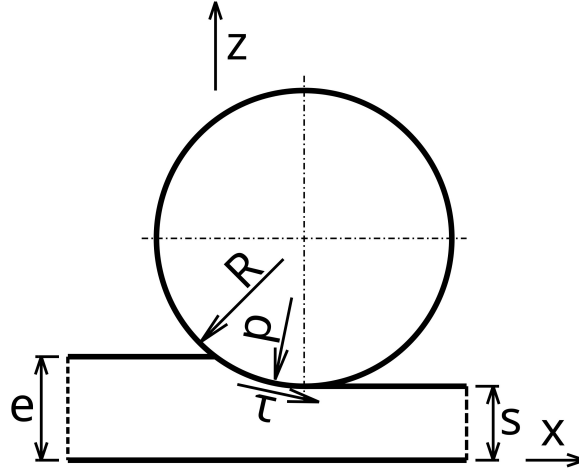
Because of the sheet's constant volume, the other two geometrical dimensions should be modified. Based on the results summarized in [2], the changes in the width can be neglected, so the relative change in the thickness dimension should be equal to the relative change in the sheet's length. For the notation of directions during the calculations, the following rules can be applied, which rules are the same as those applied in [3, 4]:

- $x$ ,  $RD$ , or 1 means the direction along the sheet's length,
- $y$ ,  $TD$ , or 2 means the direction along the sheet's width,
- $z$ ,  $ND$ , or 3 means the direction along the sheet's thickness.

The relation between the rolls' velocities can be different based on the type of the rolling process. In the case of symmetric rolling, the velocities are equal to each other, but in the case of asymmetric rolling, the velocities are different [1, 5]. This difference explains the difference in strain conditions: In the case of symmetric rolling, the characteristic types of strains are normal directional ones, but for asymmetric arrangement it is different, the shear types are typical on it [1, 3, 6, 7]. The effect of strain in different directions, i.e., normal and shear strains can be investigated by various measuring methods. The most well-documented and precious methods are the electron [1, 8–10] and X-ray [11–13] based methods, which are used for determining the relative amount of differently oriented grains. These techniques are developed by measuring the characteristic/typical texture components [1, 4, 8, 9, 14]. By knowing the amount of these texture components, it is possible determine the anisotropic and generally plastic-elastic properties of the deformed materials. The applicable options are for example the CP-FEM [15–21] or VPSC [22–26] models.

There are different methods for calculating the components and the equivalent value of the strain,





**Figure 1.** Applied geometry for simulations

in this study we have applied the version described in [14, 27–29]. The strain in the normal direction can be calculated by using Eq. (1) [27]:

$$\varepsilon_n = \frac{h_i - h_f}{h_i}, \quad (1)$$

where,  $\varepsilon_n$  is the strain in the normal direction,  $h_0$  is the sheet's thickness before rolling, and  $h_f$  is the sheet's thickness after rolling.

The measurable shear can be calculated by using Eq. (2) [27]:

$$\gamma = \frac{dx}{dz}, \quad (2)$$

where  $\gamma$  is a derivative of displacement of the sheet in the rolling direction.

The calculated shear strain contains the effect of shear and the reduction of the sheet's thickness [27]:

$$\varepsilon_S = \frac{2(1 - \varepsilon_n)^2}{\varepsilon_n(2 - \varepsilon_n)} \gamma \cdot \ln \frac{1}{1 - \varepsilon_n}, \quad (3)$$

where,  $\varepsilon_S$  is the calculated value of the shear strain.

The value of equivalent strain was calculated from the previously calculated shear strain [27]:

$$\varepsilon_{eq} = \sqrt{\frac{4}{3} \left( \ln \left( \frac{1}{1 - \varepsilon_n} \right) \right)^2 + \frac{\varepsilon_S^2}{3}}, \quad (4)$$

where,  $\varepsilon_{eq}$  is the equivalent strain.

The other important parameters, which can be used during the description of the deformation processes, are the “coefficient of friction (COF)”, and the “roll gap parameter”. The friction coefficient means the rate of the maximal slip stress and the normal pressure [30], there are many other, similar parameters for describing this phenomenon [31–33]. On other hand, there are more parameters that can be applied during this calculation [34, 35], but in our study, we have used only the geometrical parameters for calculating a minimal value of the coefficient of friction [36]. The theory under consideration is presented by Eq. (5).

$$\mu_{min} = \frac{1}{2} \sqrt{\frac{h}{R}} \frac{\ln\left(\frac{h_o}{h_f}\right) + \frac{1}{4} \sqrt{\frac{h_o - h_f}{R}}}{\tan^{-1}\left(\frac{h_o}{h_f} - 1\right)}, \quad (5)$$

where,  $\mu_{min}$  is a calculated minimal value of the coefficient of friction.

However, in case of more precise calculations and simulations, it is necessary, to use a corrected value of coefficient of friction; this correction is achieved by applying Eq. (6). The correction factor expresses the effect of the neglected parameters for example roughness, the local change of the temperature, the contact pressure, and the slip velocity between the rolls and the sheet [30].

$$\mu_{mod} = C_f \cdot \mu_{min}, \quad (6)$$

where,  $\mu_{mod}$  is the corrected value of the friction coefficient and  $C_f$  is the correction factor. The correction factor has a value of 1.1-1.4-1.5 [20, 21, 37]. Another approximation is using a constant 0.07-0.08 value, as it is described in [3].

The last, following examined important parameter is the effect of the roll gap, which documents not only the geometry of the sheet, but also the dimensions of the rolls is a significant factor [38]. This effect can be taken into account by using the parameter  $L/R$  based on simple geometrical calculations, which is described in Eq. (7).

$$\frac{L}{R} = \sqrt{\frac{h_i - h_f}{R}}, \quad (7)$$

where,  $L/R$  is the ‘‘roll gap parameter’’ and  $L$  is the length of the pressed surface.

During this study, we have examined the cold rolling of aluminum sheets, and the modeling options, mainly the finite element method and the flowline model.

## 2. Material model

The modeling of plastic deformation during specific manufacturing processes needs a mechanical material model for deformation. This model can be developed by different standard material examinations. The most commonly used methods applied for determining the deformation stress belongs to different value of strain, strain rate, and temperature. The examined material in this research is Aluminum (Al), which has various stress responses for different groups of material parameters. We examined the material about the room temperature (20-25 °C) [39, 40] and a relatively small strain rate. It has been summarized in different literature sources [41, 42], that for these parameter sets the effect of temperature and strain are subject of ignorance. These parameters are neglected because the room temperature (which has been the temperature of the specimen during the tensile test) is 40% below the melting point of Al-1050 material, which reduced the value of recrystallization temperature to 380-410 °C [43]. The Ramberg-Osgood material model [44, 45], which was used for the Finite Element Simulation (FEM), was chosen from the general material model programmed in the applied DEFORM 2D [46] FEM software by a slightly different form. The applied equation is shown in Eq. (8), and the material parameters of the equation are the following, based on the measured values of [37]: the elasticity modulus ( $E$ ) is 69.9 GPa, the hardening coefficient ( $K$ ) is 144.6 MPa and the hardening exponent is 0.370 and these parameters were determined from the tensile test.

$$\varepsilon = \frac{\sigma}{E} + \left(\frac{\sigma}{K}\right)^{1/c} \quad (8)$$

### 3. Modeling approaches

There are several approaches used for the simulation of the rolling. The three main groups can be defined by the modeling principles: simple geometrical, analytical and ones based on principles of continuum mechanics. However, the accuracy of the geometric model is relatively low due to the simplifications of complex processes. These models also use 2D [47] or 3D [48] approximations. On the other hand, it is possible to improvise these models by modifying a few parameters, that can be determined by various measurements or can be found in various literature sources. These methods for different types of rolling (hot/cold, symmetric/asymmetric) are described among others in [1, 14, 21, 49, 50].

The second group includes those methods, which are valid and applicable only to a small group of general manufacturing processes. They use fewer approximations, for example; using a simple material model by neglecting the effect of generated heat during the plastic deformation, and using a theoretical function for describing the relations between various parameters. These types of modelling techniques however have a giant advantage compared to the third group, they have a significantly higher simulation speed because they use explicit numerical methods, which provide the interpretation that the required temperature and mechanical parameters can be calculated for an arbitrary time and coordinates of the workpiece. The most commonly used examples for this group of modeling approaches are the “flowline models (FLM)”. There are several types of FLMs that can be used for calculating the deformation processes of forming manufacturing technologies beyond the rolling [51–54], for example, “(non)equal-channel angular pressing ((N)ECAP)” [55–57].

The third modeling group consists of the numerical methods. The typical example is the “finite element method (FEM)”, but there are many others, for example, the “upper bound method” [58, 59], the “uniform strain field method” [54, 60], or the “finite difference method” [54, 61]. The FEM is based on dividing the geometry into smaller parts, and the mechanical, thermodynamical, and crystallographic theories can be applied to these smaller parts for individual timesteps. The calculation is simpler for one element, but due to the large number of elements and timesteps, the calculation takes a long time. The advantage of the FEM method is, that the mechanical and thermodynamical material laws can be modified for individual materials. In addition, the contacts, properties, and the applied simplifications can be defined by user in the software. The models can be extended by crystallographic and texture calculations for determining the anisotropic and general mechanical properties of the deformed material. Examples for applying the FEM to modeling the rolling process can be found in literature [1, 3, 5, 49, 50, 52, 53, 62–68].

### 4. Flowline model

Different versions of the FLM models are based on simple continuity principles [51]. The models use an approximating function to describe streamlines/flowlines, described by Eq. (9) [51, 52], where the streamline means the material’s flow along a prescribed path, by examining the motion of rollgap’s points [52].

$$\Phi(x, z) = z \left[ 1 + \left( \alpha + \frac{(1 - \alpha)(x - d)^2}{d^2} \right)^{-n} \right]^{1/n} = \frac{z_s}{\alpha}, \quad (9)$$

where,  $\Phi$  is the streamline function,  $x$ ,  $z$  are coordinate values on the sheet as defined earlier in Fig. 1,  $z_s$  is the relative position of the rolled sheet’s thickness.

There are other important parameters, which are used by the FLM model. These parameters are described in Eq. (10)-(12) [51].

$$\alpha = \frac{s}{e}, \quad (10)$$

where,  $s$  is half-thickness after the rolling, and  $e$  is the half-thickness prior rolling.

$$\cos(\theta) = \frac{R + s - e}{R}, \quad (11)$$

where,  $\theta$  is the press angle.

$$d = R \sin(\theta), \quad (12)$$

where,  $d$  is the projected length of the pressured surface.

The following important parameters are different components of the velocity field on the sheet's cross-section. These velocities can be calculated by Eq. (13) and (14).

$$v_x(x, z) = \lambda(x, z) \frac{\partial \Phi(x, z)}{\partial z}, \quad (13)$$

$$v_z(x, z) = -\lambda(x, z) \frac{\partial \Phi(x, z)}{\partial x}. \quad (14)$$

where,  $v_x$  and  $v_z$  are the velocities of a point in directions  $x$  and  $z$ .

The calculation of the velocity values needs to have the  $\lambda(x, z)$  function in the form of Eq. (15), which can be determined from the velocity boundary conditions.

$$\lambda(x, z) = \frac{v_x(x = d, z)}{(\alpha^{-n} + 1)^{1/n}}. \quad (15)$$

where,  $v_x(x = d, z)$  is the velocity at the exit point of the streamline, it can be calculated by different methods, the used parameters during this modeling are often based on measurement [1, 15]. However, by knowing the velocity functions, we can define the velocity gradients by Eq. (16), which can be used for calculating the strain values by integrating them along the streamlines.

$$L_{ij} = \frac{\partial v_i}{\partial j}. \quad (16)$$

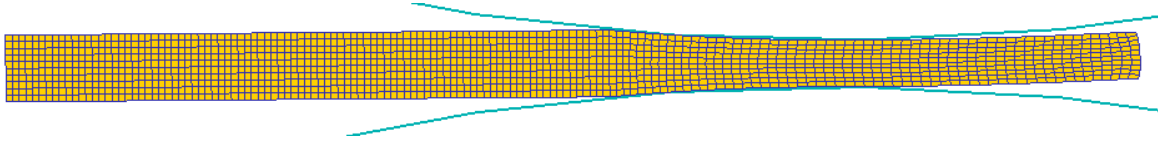
where,  $L_{ij}$  is the  $ij$  component of velocity gradient,  $v_i$  is the velocity in direction  $i$ , and  $j$  is the direction used during the derivation. The values of  $i$  and  $j$  can be  $x$ ,  $y$  and  $z$  [51].

There is a modified version of the FLM [51] method, the mFLM method, which is described in [52]. The modified streamline function is given by Eq. (17) [52].

$$\Phi(x, z) = \frac{z}{e} \left[ 1 + \left( \frac{s}{e} + \left( 1 - \frac{s}{e} \right) \left( \frac{d-x}{d} \right)^{2.1} \right)^{-m} \right]^{1/m}, \quad (17)$$

The velocity in direction  $x$  can be calculated by Eq. (18) [52].

$$v_x(x, z) = f_1(x) \cdot (1 - z_s)^n + f_2(x) \cdot z_s^n. \quad (18)$$



**Figure 2.** Applied geometry for FEM

The  $f_1$  and  $f_2$  functions can be determined from the boundary condition in form of the Eq. (19)-(21).

$$\frac{1}{n+1}f_1(x) + \frac{1}{n+1}f_2(x) = v_{in} \cdot \left[ 1 + \left( \frac{s}{e} + \left( 1 - \frac{s}{e} \right) \left( \frac{d-x}{d} \right)^{2.1} \right)^{-m} \right]^{1/m}, \quad (19)$$

$$f_2 - f_1 = \alpha \cdot \left\{ e \cdot v_{in} \cdot \left[ 1 + \left( \frac{s}{e} + \left( 1 - \frac{s}{e} \right) \left( \frac{d-x}{d} \right)^{2.1} \right)^{-m} \right]^{1/m} - f_{1,ref} \right\}, \quad (20)$$

$$f_{1,ref} = \left[ 1 - e^{-a\left(\frac{x}{d}\right)^b} \right] \left( \frac{e}{s}v_{in} - v_{in} \right) + v_{in}. \quad (21)$$

The parameters  $\alpha$  and  $n$  can be calculated from the geometrical dimensions and technological parameters by using the results of [53].

## 5. Finite element simulation of rolling

The FEM method is based on separating the bodies into smaller elements and performing further calculations on it. The rolls were modelled as rigid rotating bodies, the sheet as a plastic-elastic material. The 3D model was simplified to a 2D plane strain geometry, by neglecting the TD dimensions. The applied geometry is shown in Fig. 2, the geometrical and technological parameters are the same as for roll tests carried out. The friction coefficient is calculated by the Eq. (5) and (6). The effect of the heat and the strain rate were neglected as it was described in the material model. Simplifications made in frame of the current simulations are the same as for [3, 37]. DEFORM 2D software [46] was employed for simulation of the rolling.

## 6. Measurement

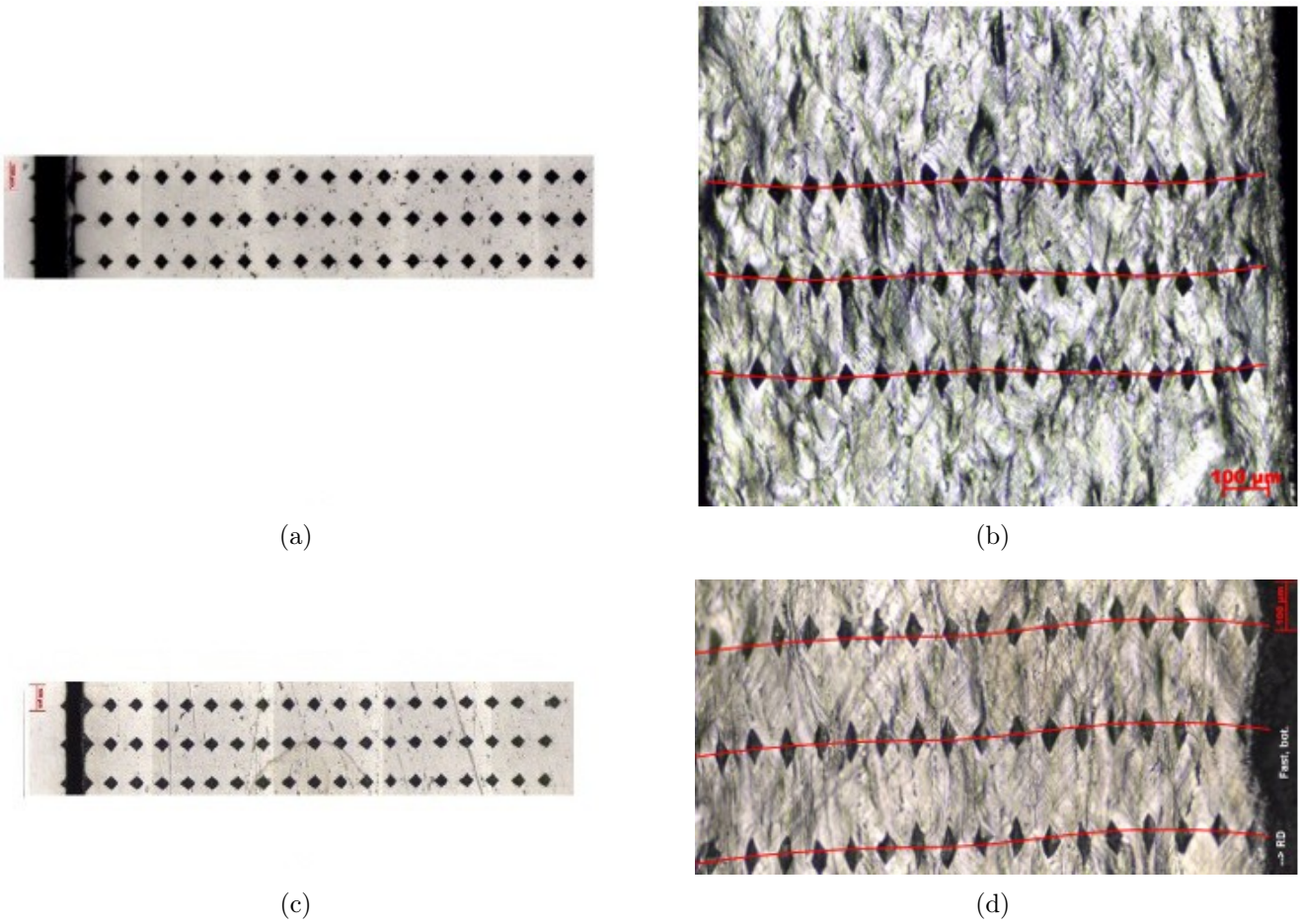
The deformation flow was investigated in both symmetrically and an asymmetrically rolled sheets. The characteristic parameters for the rolling experiments are shown in Table 1.

The displacement measurement was conducted by using the method described in [3, 69]. Prior to rolling the surface was grinded and polished, and Vickers hardness measurement was performed on the polished TD plane. After cold rolling, the relative displacements were measured between the points. The hardness indents before and after the rolling processes are shown in Fig. 3.

The relative displacement values are determined by the Fiji-ImageJ software package [70, 71], while

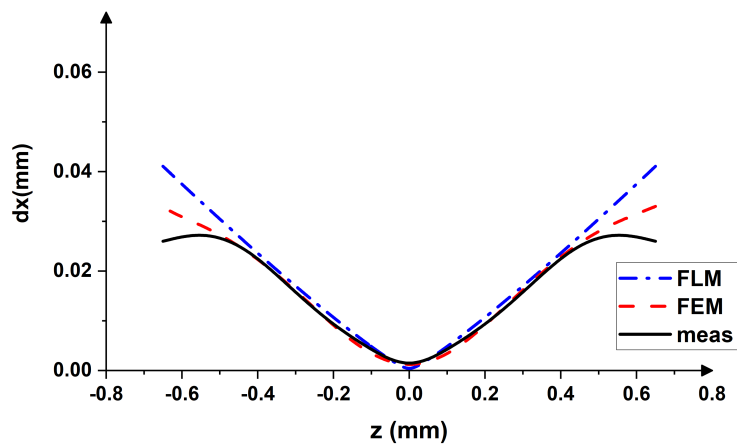
**Table 1.** Characteristic parameters for symmetric and asymmetric rolling tests

Parameter	Symmetric rolling	Asymmetric rolling
Radius of the roll, $R$ [mm]	75	75
Initial thickness of the sheet, $h_i$ , [mm]	1.92	1.92
Sheet thickness following rolling, $h_f$ , [mm]	1.25	1.35
Angular velocity of the top roll, $\omega_t$ , [rad/s]	1.1023	1.1023
Angular velocity of the bottom roll, $\omega_b$ , [rad/s]	1.1023	0.7480

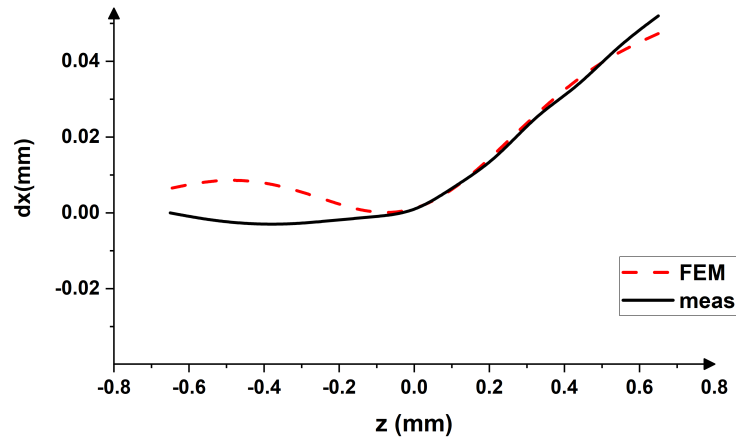


**Figure 3.** Symmetrically rolled sheet before (a) and after (b) rolling, asymmetrically rolled sheet before (c) and after (d) rolling

the extracted displacements for the symmetric and asymmetric rolling are presented in Fig. 4 and 5, respectively.



**Figure 4.** The measured and calculated displacements for the symmetrically rolled sheet



**Figure 5.** The measured and calculated displacements for the asymmetrically rolled sheet

## 7. Results

In case of symmetrically rolled sheet, the deviations for the measured three samples are significantly larger, than the measured differences of points' displacements. This deviation is due to the resolution of the applied microscope and the uneven distortion of grains. However, the values calculated by FLM, and FEM methods are comparable. The difference in results is visible in figure 4, where all the measured and calculated results are presented.

Similarly, the results for the asymmetrically rolled sheet are presented in Fig. 5. In this case the FLM method is not applicable, because this approach is valid only for symmetric rolling, the shear cannot be determined by this method. The displacement value near the faster roll is similar for both method; near the slower roll, the difference for the displacement values of different methods are higher, (15% deviation is observed).

Results of the simulations and experimental data, presented in Fig. 4 and 5 suggest that the measured data and the simulated counterparts by FEM and FLM are in a good correlation. It can be concluded here that the calculation methods with the previously described set of parameters are applicable for both symmetric and asymmetric rolling processes.

## 8. Summary

In this work we have examined different modeling approaches for the simulation of deformation by cold rolling processes. It was shown that the experimentally observed deformation flow can be successfully modelled with the Finite Element Model (FEM) and Flow Line approximation. The advantage of later over FEM is high performance in terms of computational time. The results of FEM and FLM are comparable and accurately reproduce the experimental evidence.

## 9. Acknowledgement

Project no. TKP2021-NVA-29 has been implemented with the support provided by the Ministry of Innovation and Technology of Hungary from the National Research, Development and Innovation Fund, financed under the TKP2021-NVA funding scheme.

## 10. References

- [1] J.J Sidor, R.H. Petrov, L. Kestens, *Texture Control in Aluminum Sheets by Conventional and Asymmetric Rolling*, in: Comprehensive Materials Processing, Elsevier, 2014, pp. 447–498. [CrossRef](#)

- [2] S. Geleji, *A fémek képlékeny alakításának elmélete*, Akadémiai Kiadó, Budapest, 1967.
- [3] J.Gy. Bátorfi, J.J. Sidor, *Alumínium lemez aszimmetrikus hengerlése közben fellépő deformációjának vizsgálata*, MéRNöki és Informatikai Megoldások|Engineering and IT Solutions, 2020. I, pp. 5–14, [CrossRef](#)
- [4] J.J. Sidor, Effect of Hot Band on Texture Evolution and Plastic Anisotropy in Aluminium Alloys, *Metals* 11, 2021, 1310, [CrossRef](#)
- [5] J.G. Bátorfi, P. Chakravarty, J. Sidor, *Investigation of the wear of rolls in asymmetric rolling*, MéRNöki és Informatikai Megoldások|Engineering and IT Solutions, 2021. II, pp. 14–20, [CrossRef](#)
- [6] J. Sidor, A. Miroux, R. Petrov, L. Kestens, *Controlling the plastic anisotropy in asymmetrically rolled aluminium sheets*, *Philosophical Magazine* 88, 2008, pp. 3779–3792, [CrossRef](#)
- [7] J. Sidor, R.H. Petrov, L.A.I. Kestens, *Deformation, recrystallization and plastic anisotropy of asymmetrically rolled aluminum sheets*, *Materials Science and Engineering A*. 528, 2010, pp. 413–424, [CrossRef](#)
- [8] O. Engler, V. Randle, *Introduction to texture analysis: macrotexture, microtexture, and orientation mapping*, 2nd edition, CRC Press, Boca Raton, 2010, [CrossRef](#)
- [9] U.F. Kocks, C.N. Tomé, H.-R. Wenk, *Texture and anisotropy: preferred orientations in polycrystals and their effect on materials properties*, Cambridge Univ. Press, Cambridge, 1998.
- [10] P. Chakravarty, G. Pál, J.Gy. Bátorfi, J.J. Sidor, *Estimation of Dislocation Distribution at Mid Thickness for 1050 Al*, *Acta Materialia Transylvanica* 5, 2022, pp. 6–9, [CrossRef](#)
- [11] J. Gubicza, T. Ungár, *Characterization of defect structures in nanocrystalline materials by X-ray line profile analysis*, *Zeitschrift Für Kristallographie - Crystalline Materials* 222, 2007, [CrossRef](#)
- [12] H.J. Bunge, *Texture analysis in materials science: mathematical methods*, Butterworths, London, 1982, [CrossRef](#)
- [13] D. Banabic, H.-J. Bunge, K. Pöhlandt, A.E. Tekkaya, *Formability of Metallic Materials*, Springer Berlin Heidelberg, Berlin, Heidelberg, 2000, [CrossRef](#)
- [14] S.S. Dhinwal, L.S. Toth, *Unlocking Deformation Path in Asymmetric Rolling by Texture Simulation*, *Materials* 13, 2019, 101, [CrossRef](#)
- [15] M. Diehl, *High-resolution crystal plasticity simulations*, 1. Auflage, Apprimus Verlag, Aachen, 2016.
- [16] F. Roters, ed., *Crystal plasticity finite element methods: in materials science and engineering*, Wiley-VCH, Weinheim, 2010, [CrossRef](#)
- [17] F. Roters, M. Diehl, P. Shanthraj, P. Eisenlohr, C. Reuber, S.L. Wong, T. Maiti, A. Ebrahimi, T. Hochrainer, H.-O. Fabritius, S. Nikolov, M. Friák, N. Fujita, N. Grilli, K.G.F. Janssens, N. Jia, P.J.J. Kok, D. Ma, F. Meier, E. Werner, M. Stricker, D. Weygand, D. Raabe, *DAMASK – The Düsseldorf Advanced Material Simulation Kit for modeling multi-physics*



- crystal plasticity, thermal, and damage phenomena from the single crystal up to the component scale*, Computational Materials Science 158, 2019, pp. 420–478, [CrossRef](#)
- [18] F. Roters, P. Eisenlohr, C. Kords, D.D. Tjahjanto, M. Diehl, D. Raabe, *DAMASK: the Düsseldorf Advanced Material Simulation Kit for studying crystal plasticity using an FE based or a spectral numerical solver*, Procedia IUTAM 3, 2012, pp. 3–10, [CrossRef](#)
- [19] F. Roters, P. Eisenlohr, L. Hantcherli, D.D. Tjahjanto, T.R. Bieler, D. Raabe, *Overview of constitutive laws, kinematics, homogenization and multiscale methods in crystal plasticity finite-element modeling: Theory, experiments, applications*, Acta Materialia 58, 2010, pp. 1152–1211, [CrossRef](#)
- [20] J.J. Sidor, *Crystal plasticity and continuum mechanics-based modelling of deformation and recrystallization textures in aluminum alloys*, IOP Conf. Ser.: Mater. Sci. Eng. 375, 2018, 012028, [CrossRef](#)
- [21] J.J. Sidor, *Deformation texture simulation in Al alloys: continuum mechanics and crystal plasticity aspects*, Modelling Simul. Mater. Sci. Eng. 26, 2018, 085011, [CrossRef](#)
- [22] A. Molinari, G.R. Canova, S. Ahzi, *A self consistent approach of the large deformation polycrystal viscoplasticity*, Acta Metallurgica 35, 1987, pp. 2983–2994, [CrossRef](#)
- [23] R.A. Lebensohn, C.N. Tomé, *A self-consistent anisotropic approach for the simulation of plastic deformation and texture development of polycrystals: Application to zirconium alloys*, Acta Metallurgica et Materialia 41, 1993, pp. 2611–2624, [CrossRef](#)
- [24] C.N. Tomé, R.A. Lebensohn, *Manual for Code VISCO-PLASTIC SELF-CONSISTENT (VPSC) - Version 7c*, accessed August 25, 2022, [CrossRef](#)
- [25] Q. Xie, A. Van Bael, J. Sidor, J. Moerman, P. Van Houtte, *A new cluster-type model for the simulation of textures of polycrystalline metals*, Acta Materialia 69, 2014, pp. 175–186, [CrossRef](#)
- [26] P. Eyckens, Q.G. Xie, J.J. Sidor, L. Delannay, A. van Bael, L. Kestens, J. Moerman, H. Vegter, P. van Houtte, *Validation of the Texture-Based ALAMEL and VPSC Models by Measured Anisotropy of Plastic Yielding*, MSF. 702–703, 2011, pp. 233–236, [CrossRef](#)
- [27] C.Q. Ma, L.G. Hou, J.S. Zhang, L.Z. Zhuang, *Strain Analysis during the Symmetric and Asymmetric Rolling of 7075 Al Alloy Sheets*, in: M. Hyland (Ed.), Light Metals 2015, Springer International Publishing, Cham, 2015, pp. 445–449, [CrossRef](#)
- [28] T. Inoue, *Strain Variations on Rolling Condition in Accumulative Roll-Bonding by Finite Element Analysis*, in: D. Moratal (Ed.), Finite Element Analysis, Sciyo, 2010, [CrossRef](#)
- [29] T. Inoue, H. Qiu, R. Ueji, *Through-Thickness Microstructure and Strain Distribution in Steel Sheets Rolled in a Large-Diameter Rolling Process*, Metals 10, 2020, p. 91. [CrossRef](#)
- [30] M. Szűcs, G. Krallics, J.G. Lenard, *The Difficulties of Predicting the Coefficient of Friction in Cold Flat Rolling*, Journal of Tribology 14, 2021, pp. 101703, [CrossRef](#)
- [31] G.-Y. Tzou, *Relationship between frictional coefficient and frictional factor in asymmetrical sheet rolling*, Journal of Materials Processing Technology 86, 1999, pp. 271–277, [CrossRef](#)

- [32] Q.Y. Wang, Y. Zhu, Y. Zhao, *Friction and Forward Slip in High-Speed Cold Rolling Process of Aluminum Alloys*, AMM. 229–231, 2012, pp. 361–364, [CrossRef](#)
- [33] P.P. Gudur, M.A. Salunkhe, U.S. Dixit, *A theoretical study on the application of asymmetric rolling for the estimation of friction*, International Journal of Mechanical Sciences 50, 2008, pp. 315–327, [CrossRef](#)
- [34] L.A. de Carvalho, J. Ebrahim, Z. Lukács, *The Importance of Pressure and Velocity Dependent Friction Coefficient in the Metal Forming Simulation*, GÉP LXXII, 2021, pp. 11–14.
- [35] M. Szűcs, G. Krállics, J. Lenard, *A Comparative Evaluation of Predictive Models of the Flat Rolling Process*, Period. Polytech. Mech. Eng. 2018, [CrossRef](#)
- [36] B. Avitzur, *Friction-aided strip rolling with unlimited reduction*, International Journal of Machine Tool Design and Research 20, 1980, pp. 197–210, [CrossRef](#)
- [37] J.Gy. Bátorfi, G. Pál, P. Chakravarty, J.J. Sidor, *Models for symmetric cold rolling of an aluminum sheet*, EIT, 2022.
- [38] P. Hao, A. He, W. Sun, *Predicting model of thickness distribution and rolling force in angular rolling process based on influence function method*, Mechanics & Industry 19, 2018, p. 302, [CrossRef](#)
- [39] F. Czerwinski, *Thermal Stability of Aluminum Alloys*, Materials 13, 2020, p. 3441, [CrossRef](#)
- [40] B. Gruber, F. Grabner, G. Falkinger, A. Schökel, F. Spieckermann, P.J. Uggowitzer, S. Pogatscher, *Room temperature recovery of cryogenically deformed aluminium alloys*, Materials & Design 193, 2020, 108819, [CrossRef](#)
- [41] P.T. Summers, Y. Chen, C.M. Rippe, B. Allen, A.P. Mouritz, S.W. Case, B.Y. Lattimer, *Overview of aluminum alloy mechanical properties during and after fires*, Fire Sci Rev. 4, 2015, p. 3, [CrossRef](#)
- [42] F. Huang, N.R. Tao, *Effects of Strain Rate and Deformation Temperature on Microstructures and Hardness in Plastically Deformed Pure Aluminum*, Journal of Materials Science & Technology 27, 2011, pp. 1–7, [CrossRef](#)
- [43] Y. Zhao, L. Li, Z. Lu, G. Teng, S. Liu, Z. Hu, A. He, *The effect of annealing temperature on the recrystallization and mechanical properties of severe plastic deformed commercial pure aluminium during ultra-fast annealing*, Mater. Res. Express. 8, 2021, 046515, [CrossRef](#)
- [44] G. Gadamchetty, A. Pandey, M. Gawture, *On Practical Implementation of the Ramberg-Osgood Model for FE Simulation*, SAE Int. J. Mater. Manf. 9, 2016, pp. 200–205, [CrossRef](#)
- [45] W. Ramberg, W.R. Osgood, *Description of stress-strain curves by three parameters*, 1943, accessed November 24, 2021, [CrossRef](#)
- [46] J. Fluhner, *DEFORM(TM) 2D Version 8.1 User's Manual*, [CrossRef](#)
- [47] Y.-M. Hwang, T.-H. Chen, H.-H. Hsu, *Analysis of asymmetrical clad sheet rolling by stream function method*, International Journal of Mechanical Sciences 38, 1996, pp. 443–460, [CrossRef](#)

- [48] S.I. Oh, S. Kobayashi, *An approximate method for a three-dimensional analysis of rolling*, International Journal of Mechanical Sciences 17, 1975, pp. 293–305, [CrossRef](#)
- [49] J.J. Sidor, *Deformation Texture Modelling By Mean-Field And Full-Field Approaches*, AML. 10, 2019, pp. 643–650, [CrossRef](#)
- [50] H.P. Yang, Y.H. Sha, F. Zhang, L. Zuo, *Through-thickness shear strain control in cold rolled silicon steel by the coupling effect of roll gap geometry and friction*, Journal of Materials Processing Technology 210, 2010, pp. 1545–1550, [CrossRef](#)
- [51] B. Beausir, L.S. Tóth, *A New Flow Function to Model Texture Evolution in Symmetric and Asymmetric Rolling*, in: A. Haldar, S. Suwas, D. Bhattacharjee (Eds.), *Microstructure and Texture in Steels*, Springer London, London, 2009, pp. 415–420, [CrossRef](#)
- [52] K. Decroos, J. Sidor, M. Seefeldt, *A New Analytical Approach for the Velocity Field in Rolling Processes and Its Application in Through-Thickness Texture Prediction*, Metall and Mat Trans A. 45, 2014, pp. 948–961, [CrossRef](#)
- [53] J.J. Sidor, *Assessment of Flow-Line Model in Rolling Texture Simulations*, Metals 9, 2019, 1098, [CrossRef](#)
- [54] A. Halloumi, Ch. Desrayaud, B. Bacroix, E. Rauch, F. Montheillet, *A Simple Analytical Model of Asymmetric Rolling*, Archives of Metallurgy and Materials 57, 2012, [CrossRef](#)
- [55] A. Hasani, L.S. Toth, Sh. Mardokh Rouhani, *A New Flow Line Function for Modeling Material Trajectory and Textures in Nonequal-Channel Angular Pressing*, Advances in Materials Science and Engineering, 2019, pp. 1–6, [CrossRef](#)
- [56] A. Hasani, L.S. Tóth, B. Beausir, *Principles of Nonequal Channel Angular Pressing*, Journal of Engineering Materials and Technology 132, 2010, 031001, [CrossRef](#)
- [57] L.S. Tóth, R. Arruffat Massion, L. Germain, S.C. Baik, S. Suwas, *Analysis of texture evolution in equal channel angular extrusion of copper using a new flow field*, Acta Materialia 52, 2004, pp. 1885–1898, [CrossRef](#)
- [58] A. Parvizi, K. Abrinia, *A two dimensional upper bound analysis of the ring rolling process with experimental and FEM verifications*, International Journal of Mechanical Sciences 79, 2014, pp. 176–181, [CrossRef](#)
- [59] B. Avitzur, *An Upper-Bound Approach to Cold-Strip Rolling*, Journal of Engineering for Industry 86, 1964, pp. 31–45, [CrossRef](#)
- [60] Y. Yang, Y. Peng, *Dynamic rolling model based on uniform deformation*, Journal of Manufacturing Processes 58, 2020, pp. 1334–1347, [CrossRef](#)
- [61] C. Yao, A. He, J. Shao, J. Zhao, G. Zhou, H. Li, Y. Qiang, *Finite Difference Modeling of the Interstand Evolutions of Profile and Residual Stress during Hot Strip Rolling*, Metals 10, 2020, 1417, [CrossRef](#)
- [62] A. Ma, F. Roters, D. Raabe, *A dislocation density based constitutive model for crystal plasticity FEM including geometrically necessary dislocations*, Acta Materialia 54, 2006, pp. 2169–2179, [CrossRef](#)

- [63] D. Pustovoytov, A. Pesin, P. Tandon, *Asymmetric (Hot, Warm, Cold, Cryo) Rolling of Light Alloys: A Review*, *Metals* 11, 2021, p. 956, [CrossRef](#)
- [64] D. Pustovoytov, A. Pesin, O. Biryukova, *Finite element analysis of strain gradients in aluminium alloy sheets processed by asymmetric rolling*, *Procedia Manufacturing* 15, 2018, pp. 129–136, [CrossRef](#)
- [65] M. Wronski, K. Wierzbanski, B. Bacroix, P. Lipinski, *Asymmetric rolling textures of aluminium studied with crystalline model implemented into FEM*, *IOP Conference Series: Materials Science and Engineering* 82, 2015, 012012, [CrossRef](#)
- [66] T. Imai, H. Utsunomiya, R. Matsumoto, *Finite Element Analysis of Plastic Instability Phenomenon in Cold Rolling of Clad Sheets*, *Procedia Engineering* 184, 2017, pp. 306–312 [CrossRef](#)
- [67] A. Graça, G. Vincze, *A Short Review on the Finite Element Method for Asymmetric Rolling Processes*, *Metals*. 11, 2021, p. 762, [CrossRef](#)
- [68] H. Wang, S. Ding, T. Taylor, J. Yanagimoto, *Cold Rolling Texture Prediction Using Finite Element Simulation with Zooming Analysis*, *Materials* 14, 2021, p. 6909, [CrossRef](#)
- [69] R. Roumina, C.W. Sinclair, *Deformation Geometry and Through-Thickness Strain Gradients in Asymmetric Rolling*, *Metall and Mat Trans A* 39, 2008, pp. 2495–2503, [CrossRef](#)
- [70] J. Schindelin, I. Arganda-Carreras, E. Frise, V. Kaynig, M. Longair, T. Pietzsch, S. Preibisch, C. Rueden, S. Saalfeld, B. Schmid, J.-Y. Tinevez, D.J. White, V. Hartenstein, K. Eliceiri, P. Tomancak, A. Cardona, *Fiji: an open-source platform for biological-image analysis*, *Nat Methods* 9, 2012, pp. 676–682, [CrossRef](#)
- [71] C.A. Schneider, W.S. Rasband, K.W. Eliceiri, *NIH Image to ImageJ: 25 years of image analysis*, *Nat Methods* 9, 2012, pp. 671–675, [CrossRef](#)

# Investigation of cutting force components and surface roughness in face milling with different cutting ratios

Csaba Felhő<sup>a\*</sup>, Frezgi Tesfom<sup>a</sup>

<sup>a</sup> *University of Miskolc*

## ABSTRACT

During the face milling process, the choice of technological parameters plays an important role. The two most important parameters are the feed and the depth of cut; the ratio of which is also called the cutting ratio. The main topic of the paper is to examine how different values of the chip ratio affect the components of the cutting force and the roughness of the machined surface. It is also shown how important it is to know the exact geometry of the cutting insert, as well as - in the case of cutting with multiple inserts - the knowledge of the run-out between the individual inserts. Based on the performed investigations, it was determined that the use of a chip ratio close to one is not recommended either in terms of cutting force components or surface roughness.

**Keywords:** *face milling, cutting ratio, cutting force, surface roughness*

---

## 1. Introduction

In the modern advanced manufacturing era, traditional machining equipment are replaced by computer numerical control (CNC) machines for lots of advantage. The most frequently used machining process in the industry gained this advancement are milling and turning processes which are used to remove material from workpieces [1]. Easy machining process, low-cost production system, time and power saving, continuously increase product quality to answer customer demand, and environmentally friendly production system are the main points the manufacturing industry needs to address to compete in the market [2–4]. CNC milling machines are popularly used for metal cutting operations, especially in complicated and very detailed cutting processes [5]. Machines equipped with CNC control are even capable of a certain degree of autonomous operation [6]. Cutting force provided by the spindle and table in different cases greatly affects and is used to predict machining characteristics namely, surface roughness, vibration, chatter, and cutting power.

Face milling, one of the milling cutting methods for creating a planar surface uses a variety of inserts type of material, shape, and numbers to entertain different cutting parameters which affects the surface finish of the product. To increase material removal, high feed rate, depth of cut (increase chip cross-section) [7], and bigger cutting tool diameter are the most responsible cutting parameters. Reducing the thickness of the material to be removed in the design stage is another way of reducing the machining cost if it is observed from the machining time, energy, and tool life perspective. Cutting force components on the workpiece and cutting tool have a direct relationship with these cutting conditions.

---

© ELTE, Faculty of Informatics, Savaria Institute of Technology, 2022

\*Corresponding author: Csaba Felhő, csaba.felho@uni-miskolc.hu

<https://doi.org/10.37775/EIS.2022.2.5>

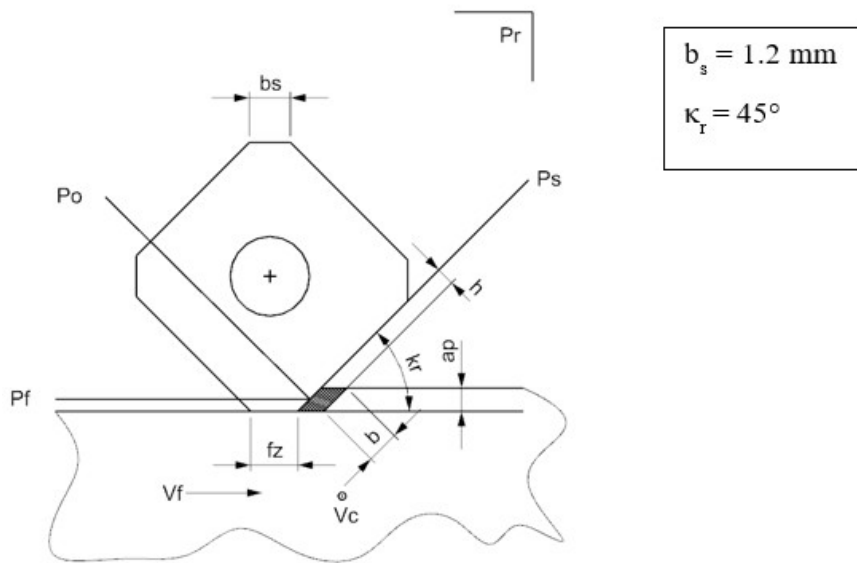
The milling machining process is further evaluated by the quality of the workpiece surface finish as it affects its mechanical and other properties [8] in addition to its efficiency. Another very important factor that helps to indicate milling process performance is cutting force to the depth of cut and feed rate [9–11]. Theoretical, numerical, and experiment-based researches are showing promising increases in addressing the demanded minimum production time per workpiece and the minimum cost of production while maintaining the required quality. Such targeted goals can be achieved by using suitable optimized cutting parameters. Face milling uses multiple inserts with round, square, rectangular-shaped, convex triangular, and parallelogram-shaped inserts to remove material from the workpiece [12]. Kundrak et al. [13] studied the effect of milling process parameters such as depth of cut ( $a_p$ ), cutting speed ( $v_c$ ) and feed rate ( $v_f$ ) on the outcome of the face milling process and verified that feed rate is the most dominant factor. This predominant factor requires continuous thrust from the workbench carrying the workpiece against the cutting insert which affects the cutting force. Apart from the feed rate, an increase in the depth of cut raises the contact duration which gives rise to friction between the cutting insert and workpiece. These interconnected effects give a decreased cutting force.

Furthermore, studies of cutting force estimation and its effect on the milling process based on more than one combined cutting parameters effect have been conducted. An experimental investigation on changes in cutting force and surface roughness were conducted by changing the cutting parameters which are depth of cut and feed per tooth [14]. Based on this research, the undeformed chip cross-section variation represented by  $f_z$  and  $a_p$  which stands for feed per tooth and depth of cut respectively influence the power required by the process by altering all three cutting force components. Another research by Akkad and Felhó [15] attested a decreased component of force by decreasing the depth of cut and feed per tooth while the undeformed chip cross-section remains constant. Chirita et al. [16] conducted an experiment designed by response surface methodology and analyzed using ANOVA to study the input parameters (depth of cut and feed) to the mathematical model developed. The inputs, their interactions, and feed direction-cooling interactions had the most significant influence on the main cutting force. The same inputs effect on surface roughness were also studied and the result showed that feed, feed direction, and the interaction of feed direction and cooling type were the most dominant factors.

Modelling the milling process and optimization of the process using numerical solutions with the help of finite element method (FEM) are popular trends in recent research for predicting possible process mechanisms. A new machine learning algorithms approach and finite element analysis were used to predict the cutting force of face milling of AISI 4140 with coated cemented carbide inserts under dry cutting conditions [17]. Different machine learning algorithms were used in the modelling process and ANSYS software was used for the FEM part of the research. From the applied algorithms, SVR achieved the best performance and with this machine learning algorithm, the required cutting



**Figure 1.** The applied milling head with the holder



**Figure 2.** Position of the cutting insert and the workpiece

force during milling procedures was calculated. FEM simulation validated by experiment research on C45 material to study the characteristics of milling with changing cross-sections showed chip ratio equal to one must be avoided from an energy point of view [18]. In the same research, the recommendation given regarding the chip ratio is  $a_p/f_z < 1$ .

With the brief review done on the conducted research regarding the effect of changing the ratio of the depth of cut and feed per tooth (chip ratio) on cutting force components, it can be concluded that still more research is needed. In the present work, experimental work was conducted to study the varying behaviour of cutting force and surface roughness up on changing ratio of the depth of cut and feed per tooth. This research work can help in selecting the ratio with a minimum cutting force of the two cutting parameters for an optimized machining process.

**2. Materials and methods**

The experiments were performed on the Perfect Jet MCV-M8 CNC milling machine at the Institute of Manufacturing Sciences of the University of Miskolc. During the experiments, a Canela 0748.90.063 face milling head was used with Dijet SEKN 1203 AFTN JC5030 cutting inserts Fig. 1 shows the applied tool with the holder.

Fig. 2 shows the shape of the cutting insert along with the characteristic geometry and cutting parameters. It can be seen in the figure, that the insert has a 1.2 mm edge parallel to the machined

**Table 1.** The applied constant parameters

Parameter	Value
Cutting speed, $v_c$ [m/min]	150
Cutter diameter, $D_c$ [mm]	63
Cut width, $a_e$ [mm]	59
Main cutting edge angle, $\kappa_r$ [°]	45
Wiper edge length, $b_s$ [mm]	1.2
Undeformed chip cross-section, $a_c$ [mm <sup>2</sup> ]	0.08

**Table 2.** The applied constant parameters

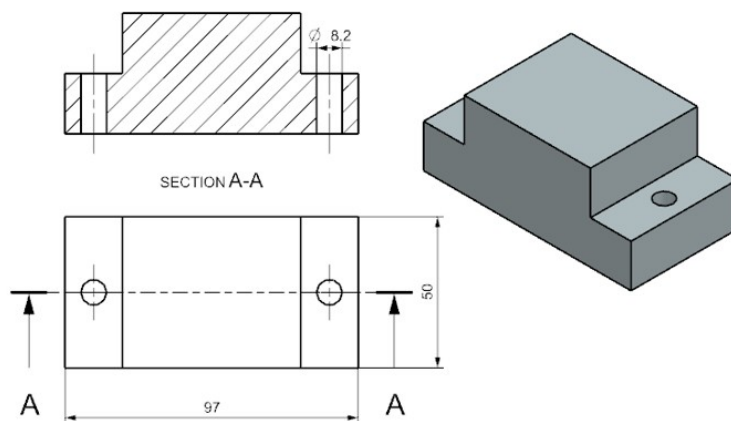
Workpiece	1	2	3	4	5
Feed per tooth, $f_z$ [mm]	0.01	0.18	0.26	0.32	0.40
Depth of cut, $a_p$ [mm]	0.8	0.44	0.31	0.25	0.20
$a_p/f_z$ ratio, [-]	8.00	2.47	1.18	0.78	0.50
Feed rate (1 insert), $v_f$ [mm/min]	76	136	197	243	303
Feed rate (5 inserts), $v_f$ [mm/min]	379	682	985	1213	1516

surface ( $b_s$ , which is often referred to as “wiper edge”), which enables a fine surface roughness to be obtained even with a relatively large feed (when  $f_z < b_s$ ). The representations shown in Fig. 2 are the tool reference plane ( $P_r$ ),  $P_s$  is the tool edge plane,  $P_f$  is the assumed work plane and  $P_o$  is the orthogonal plane.

In Fig. 2, only the dimensions of the main cutting-edge angle ( $\kappa_r$ ), the length of the edge section parallel to the machined surface ( $b_s$ ), and the cutting speed ( $v_c$ ) are constant, because, during the test, a different value of the  $a_p/f_z$  ratio was selected for each workpiece. Consequently, during cutting, the other parameters changed according to the ratio, which of course influenced the resulting force components. The applied constant parameters are summarized in Table 2 shows the ratio of the feed per tooth and the depth of cut, as well as the values of the feed rates which varies by changing the  $a_p/f_z$  ratios in the case of one or five inserts.

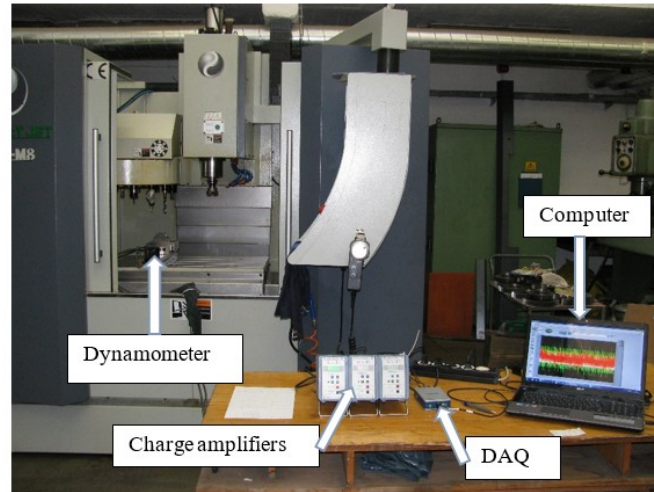
When five inserts were placed into the milling head, the axial deviations of the cutting inserts were checked with a Zoller Hyperion tool measuring device. Before the measurement, the inserts were marked with numbers in the milling head to be able to identify them. The axial runout of the inserts in relation to the deepest-lying one (Insert 5) are 37, 25, 49, 20 and 0  $\mu\text{m}$  respectively.

The material of the workpiece used was C45 normalized carbon steel, which is a general-purpose unalloyed steel. Nowadays, it is one of the most widely used raw material to produce various parts (these areas of use can be, for example, parts of the machine and automotive industry that require lower loads, as well as wear-resistant parts, pressure-bearing parts, screw production, etc.). C45 carbon steel is excellent for heat treatment, which is a rather important aspect from the point of view of production technology. Fig. 3 shows the specimen used during the research in a sectional, a top view, and a three-dimensional representation. To carry out the tests, the workpiece had to be made with the dimensions shown in the figure. The holes on the specimen were used for attachment to the dynamometer. The cutting process was performed on the upper  $50 \times 59$  mm surface of the



**Figure 3.** Geometric characteristics of the specimen used during the experiments





**Figure 4.** The machining and force measurement system for experimental tests

part. The cutting force components were determined experimentally using instrumental measurements. For this purpose, a force-measuring instrument was attached to the machining system. This force measuring system consisted of a Kistler 9257A three-component dynamometer, 3 pcs Kistler 5011A charge amplifiers, a National Instruments CompactDAQ-9171 four-channel data acquisition unit (USB), and a portable computer for data processing and visualization. The measuring software was created in the LabView programming language. Fig. 4 shows the listed measuring devices assembled in the manner which was necessary to perform the experiments. Roughness measurements were also performed, for which an AltiSurf 520 three-dimensional surface topography analyzer equipment from Altimet Company (France) was used with a CL2 confocal chromatic sensor equipped with an MG140 magnifier. The measurement range of this setup is 300  $\mu\text{m}$ , while its axial resolution is 50 nm. The Altimap software, a product of the Digital Surf company (France), was used to evaluate the roughness data. The measurements and evaluations were performed according to ISO 4287 and ISO 4288 standards because the software of the previously described roughness measuring device supports these standards. However, we would like to note that these standards are already in withdrawn status, the new, current standards are EN ISO 21921-2:2021 and ISO 21920-3:2021, respectively. However, the existence of the new standard does not necessarily mean that instruments according to the old standard can no longer be used for certain tasks. For the three-dimensional parameters, the ISO 25178-2:2021 standard was considered. During the investigations, the following surface roughness parameters were used to qualify the surfaces:

- $R_a$ : arithmetical mean of the absolute ordinate values  $Z(x)$  within a sampling length.
- $R_z$ : maximum height of profile: sum of the height of the largest profile peak height  $Z_p$  and the largest profile valley depth  $Z_v$  within the sampling length. When five sampling lengths are considered (as in the current study), the old ten-point parameter can be obtained.
- $S_a$ : arithmetic mean of the absolute ordinate values within a defined area  $A$ .
- $S_{10z}$ : ten-point height of surface: average value of the heights of the five peaks with the largest global peak height added to the average value of the heights of the five pits with the largest global pit height, within the definition area:  $S_{10z} = S_{5p} + S_{5v}$ .

The microscopic images presented in the article were taken with a Zeiss Stereo Discovery V8-type stereomicroscope.

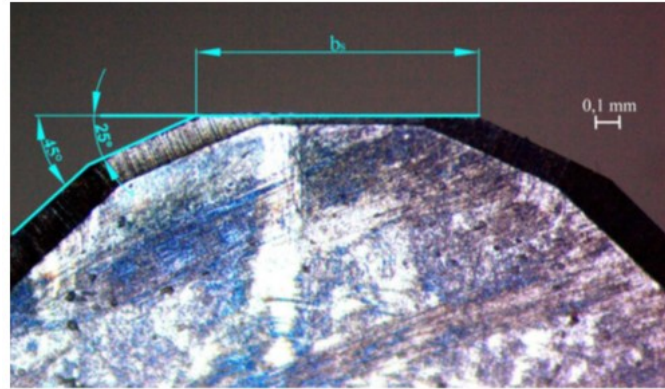


Figure 5. Microscopic image of the working part of the cutting insert

### 3. Results

During the presentation of the results, it is necessary to first describe an interesting discovery. Even though the insert manufacturer has specified the main cutting-edge placement angle of 45° for the insert, microscopic examinations revealed that it has a 25° facet too (see Fig. 5). It is known that better surface roughness can be achieved with faceted inserts [19]. Such unpublished features help manufacturers make their inserts competitive in the market and possibly outperform other manufacturers’ products. However, it is worth noting that the facet also affects the values of the cutting forces, so in the case of applying theoretical calculations and FEM modelling, it is worth examining the inserts carefully in each case, and not relying solely on the public catalogue data. This can be particularly critical when cutting on a micro-scale [20].

Fig. 6 provides help for the interpretation of the individual force components. The applied force-measuring equipment can measure the forces acting on the workpiece since the workpiece has been fixed on the force-measuring cell. These are the forces  $F_x$ ,  $F_y$ , and  $F_z$ . At the same time, the forces  $F_c$ ,  $F_f$ , and  $F_p$  are the forces acting on the tool, which are directly related to the individual cutting parameters ( $v_c$ ,  $v_f$  and  $a_p$ , respectively).

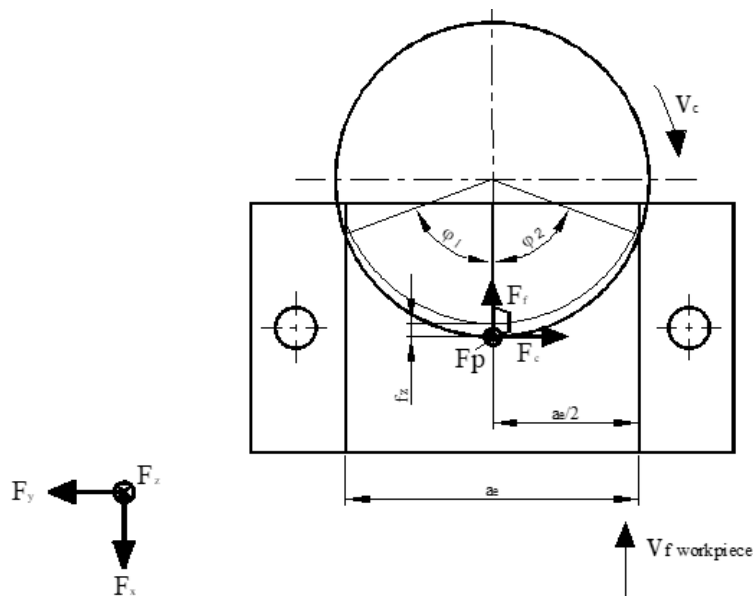
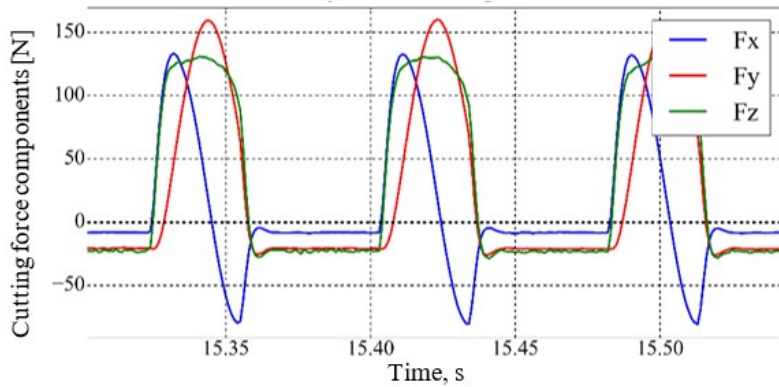


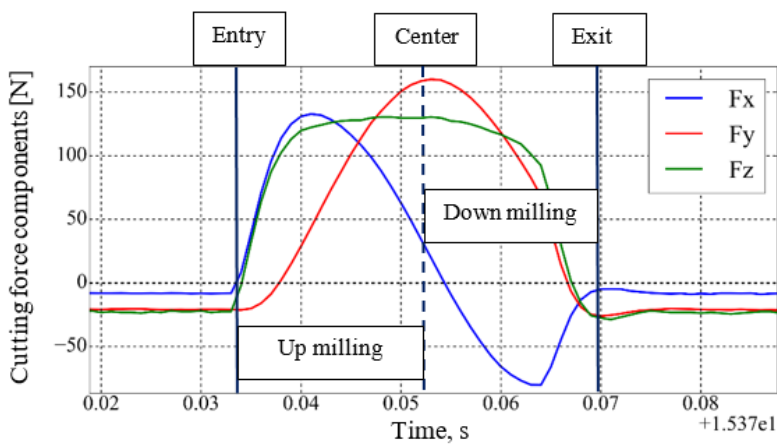
Figure 6. Interpretation of several cutting parameters and cutting force components



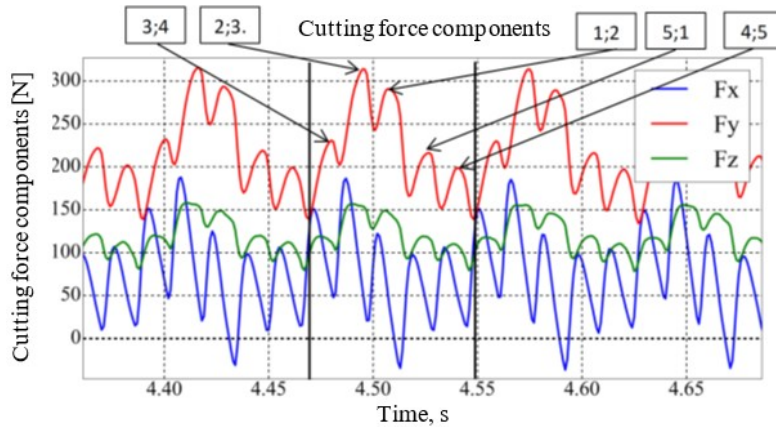
**Figure 7.** The force components  $F_x, F_y, F_z$  when cutting with one insert ( $a_p/f_z = 1.18$ )

In the following, the results of the cutting experiments with one insert are described. Fig. 7 shows the force components  $F_x, F_y, F_z$  for three cutting periods. It can be seen in the figure, that the forces are cyclically repeated as a function of time. It can be also observed, that when no cutting has yet taken place, the zero point of the force components has shifted during the measurement. It was important to take this into account when determining the data, otherwise one can get false values. This can be solved by a simple offset (adding a constant value to the measurement results). Despite all of this, the values of the measured force components can be easily read from the diagram with sufficient accuracy. The periodic pattern of the diagram clearly shows the chip removal stages.

Fig. 8 shows one cutting period of the force components as a function of time, so basically, a single chip removal section is shown enlarged, representing the working period of a cutting edge from the entry to the exit. The diagram in Fig. 8 shows that the force  $F_y$  is the largest of the components because the main cutting motion (rotation of the cutter) generates a large force in that direction. The force  $F_x$  can also be said to be relatively large, this force is also connected to the main cutting motion and the feeding motion as well. However, there is a change in character for this force component - precisely because of the main cutting speed. From a quarter of the cutting period, the force  $F_x$  starts to decrease, and it even goes into the negative range after the insert crossed the milling head centreline, since from here on the main cutting speed has the opposite meaning to the direction of this force. The force  $F_z$  shown in the diagram can be said to be relatively linear compared to the other forces, it reaches the linear section in a relatively short time (insert entry time) and drops suddenly at the exit. The components of the cutting force acting on the tool can be deduced in the



**Figure 8.** Three characteristic points of the force curves for  $a_p/f_z = 1.18$  (cutting with one insert)



**Figure 9.** The force components  $F_x$ ,  $F_y$ ,  $F_z$  measured at cutting with five inserts when  $(a_p/f_z = 1.18)$

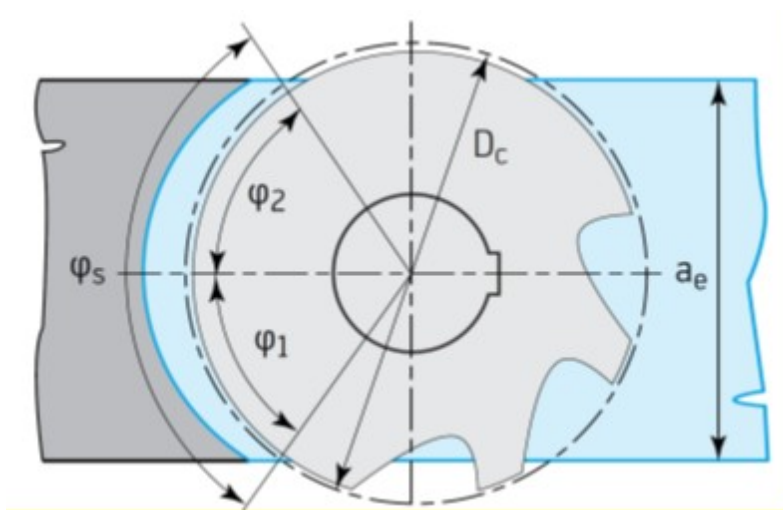
following way for the cutting insert in a special angular position, as shown earlier in Fig. 6. The main cutting force  $F_c$  is obtained when  $F_y$  has a maximum, and this occurs at the angular position in Fig. 6:  $F_c = F_{y,max}$ . At the same moment, however, the force  $F_f$  has only an  $x$ -direction component, so  $F_f = F_x(F_{y,max})$ . And the force  $F_p$  is equal to  $F_z$ , the maximum of which was taken.

Fig. 9 shows the force diagram for face milling with five inserts. The diagram shows that even during the cutting of 5 inserts, the shape of the force components is repeated periodically, and they take almost the same value in each period. From the number of peaks of the acting force components, it can be determined that all 5 inserts are indeed cutting during one rotation. The number of inserts simultaneously involved in the cut at a given moment in time ( $\psi$ ) is given by Eq. (1).

$$\psi = \frac{z_s}{2\pi}(\hat{\varphi}_1 + \hat{\varphi}_2) \approx 1.92, \tag{1}$$

where  $z_s$  is the number of inserts,  $\hat{\varphi}_1$  is the range of up (conventional) milling and  $\hat{\varphi}_2$  is the range of down (climb) milling. The  $(\hat{\varphi}_1)$  and  $(\hat{\varphi}_2)$  angles can be determined by Eq. (2) from the diameter of the cutter and the width of the cut as shown in Fig. 10.

$$\hat{\varphi}_1 = \hat{\varphi}_2 = \sin^{-1} \frac{a_e}{D_c} \approx 1.21. \tag{2}$$



**Figure 10.** Visualization of the  $\hat{\varphi}_1$  and  $\hat{\varphi}_2$  angles [21]

Approximated insert exit and entry of next insert

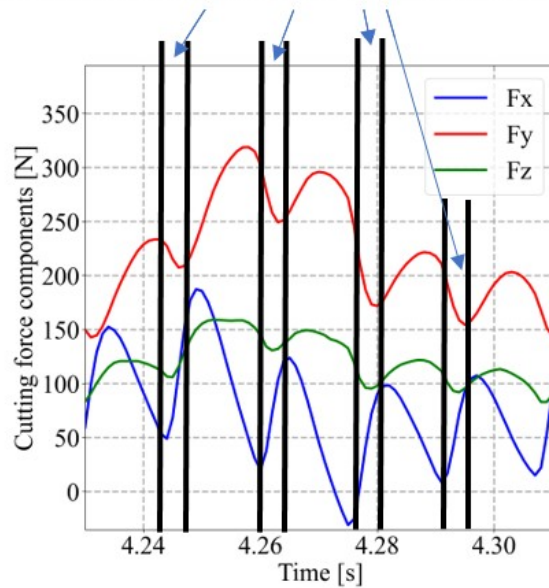

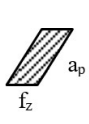
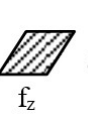
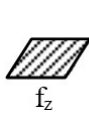
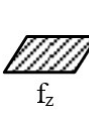


Figure 11. Approximated insert exit and entry ranges according to  $\psi$

From the above value of the number of inserts simultaneously involved in the cut, it can be determined that in this case, two inserts are almost always in cutting action at the same time, only one insert is cutting for a very short time.

These findings for the simultaneously cutting inserts are supported by Fig. 11 (which is, by the way, the enlarged detail of Fig. 10, showing a single cutting period), where it can be seen that the force component  $F_z$  decreases at the exit of the currently working insert, and then starts to increase again when the next insert enters into the cut. The other force components - since they depend on

Table 3. Values of the force components measured for face milling with one and five inserts

	Parameter	1	2	3	4	5
Workpiece	Feed per tooth, $f_z$ [mm]	0.10	0.18	0.26	0.32	0.40
	Depth of cut, $a_p$ [mm]	0.80	0.44	0.31	0.25	0.20
	Theoretical chip cross section					
	$a_p/f_z$ ratio	8.00	2.47	1.18	0.78	0.50
1 insert	$F_{x,max}$ [N]	199.60	163.33	141.34	129.87	120.47
	$F_{y,max} = F_c$ [N]	234.20	198.82	180.96	174.96	169.42
	$F_{z,max} = F_p$ [N]	200.10	166.06	153.00	143.67	130.61
	$F_f$ [N]	54.18	35.69	28.05	24.22	23.11
5 inserts	$F_{x,max}$ [N]	262.4	190.10	178.40	174.60	129.70
	$F_{y,max} = F_c$ [N]	348.70	291.80	316.70	311.50	217.90
	$F_{z,max} = F_p$ [N]	160.20	149.90	158.10	162.30	131.20
	$F_c$ [N]	227.06	225.52	253.94	253.54	170.54
	$F_f$ [N]	79.30	51.94	47.32	100.18	34.30

the rotational motion - therefore do not show this change that clearly. The insert exit and entry points indicated in the figure were marked only approximately, based on visual inspections.

Based on Table 3, it is known that the inserts were at distinct height differences from each other in the milling head. From these data, it was concluded that at the highest peaks of force values shown in Fig. 9, the deepest-lying inserts do the cutting, which is the 2nd and 3rd inserts based on Table 3. After the highest force component, the next peak value was formed by the cutting of the 1st and 2nd inserts. The third largest value, and the middle values of the force components, were created by the 3rd and 4th inserts. After that, inserts 5 and 1 followed, and inserts 4 and 5 determined the formation of the smallest peak value at the end of the period.

The cutting force components acting on the tool  $F_c$ ,  $F_f$ , and  $F_p$  in the case of cutting with five inserts were determined using the previously described method as well, and the final cutting force values were obtained by averaging the force values of each pair of inserts.

The values of the measured ( $F_x$ ,  $F_y$  and  $F_z$ ) and inferred ( $F_c$ ,  $F_f$ ,  $F_p$ ) force components for the cutting experiments with one and five inserts are summarized in Table 3. In the case of some force components, the maximum values were taken as numerical values, this is indicated by the "max" subscript. In the following, these parameters are referenced without this index. In the following, the force components  $F_c$ ,  $F_f$ , and  $F_p$  acting on the tool will be analysed, as they are generally used to characterize the cutting process.

The diagrammatic representation of the force values is illustrated in Fig. 12. Among the examined force components,  $F_c$  is clearly the largest, both in the case of cutting with one insert and with five inserts. However, it is immediately obvious that both the  $F_c$  and  $F_f$  components have a spike around the  $a_p/f_z = 1$  ratio when cutting with five inserts. This leads to the conclusion, that the value  $a_p/f_z = 1$  should be avoided, especially when milling with five inserts. By the way, the same jump can also be observed in the  $F_p$  diagram belonging to the five inserts, but to a lesser extent.

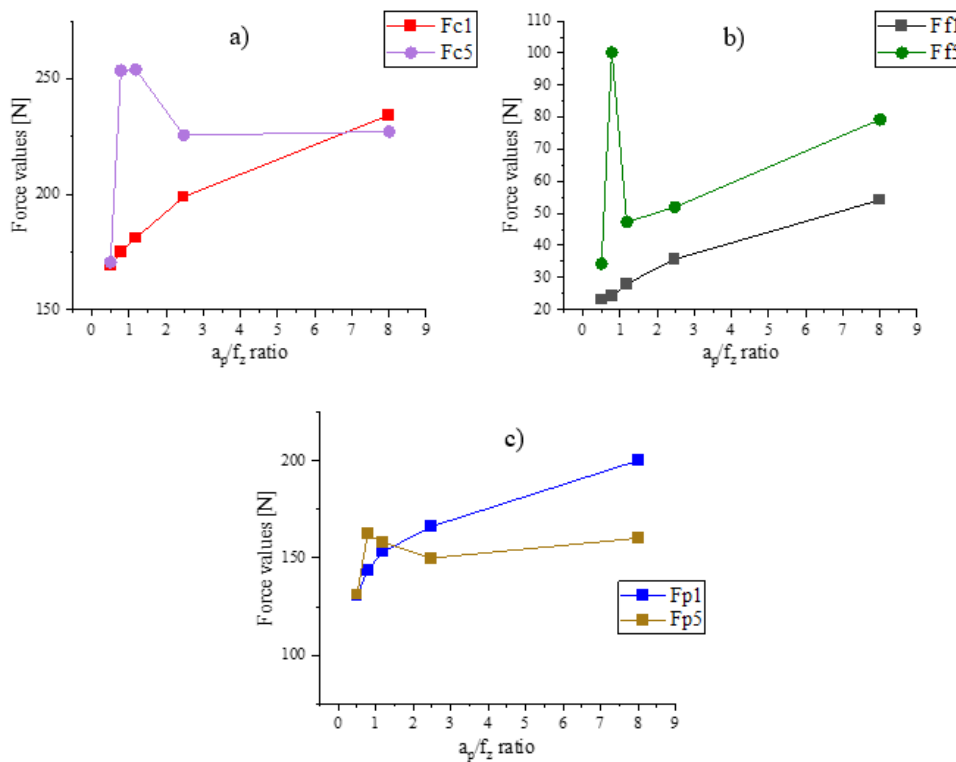


Figure 12. Force components obtained in experiments with one and five inserts (a)  $F_c$ ; b)  $F_f$ ; c)  $F_p$ )

**Table 4.** Surface roughness values measured when using one insert

	$f_z$ [mm]	$a_p$ [mm]	$R_a$ [ $\mu\text{m}$ ]	$R_z$ [ $\mu\text{m}$ ]	$S_a$ [ $\mu\text{m}$ ]	$S_{10z}$ [ $\mu\text{m}$ ]
#1	0.10	0.80	0.25	1.74	0.25	3.16
#2	0.18	0.44	0.48	3.70	0.47	4.00
#3	0.26	0.31	0.54	3.94	0.56	5.26
#4	0.32	0.25	0.57	4.06	0.60	5.21
#5	0.40	0.20	0.62	4.35	0.61	4.37

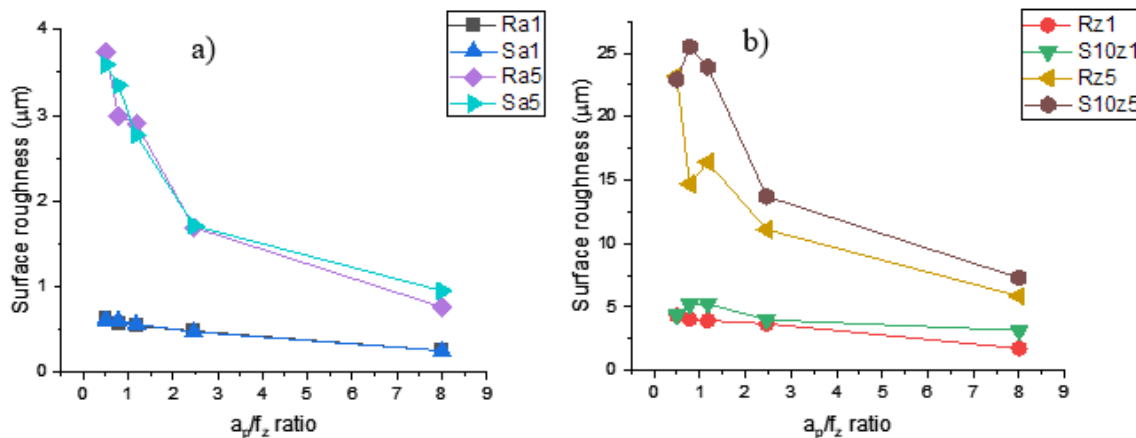
**Table 5.** Surface roughness values measured when using five inserts

	$f_z$ [mm]	$a_p$ [mm]	$R_a$ [ $\mu\text{m}$ ]	$R_z$ [ $\mu\text{m}$ ]	$S_a$ [ $\mu\text{m}$ ]	$S_{10z}$ [ $\mu\text{m}$ ]
#1	0.10	0.80	0.76	5.86	0.95	7.30
#2	0.18	0.44	1.69	11.10	1.71	13.70
#3	0.26	0.31	2.90	16.40	2.77	23.90
#4	0.32	0.25	2.99	14.70	3.35	25.50
#5	0.40	0.20	3.74	23.20	3.59	22.90

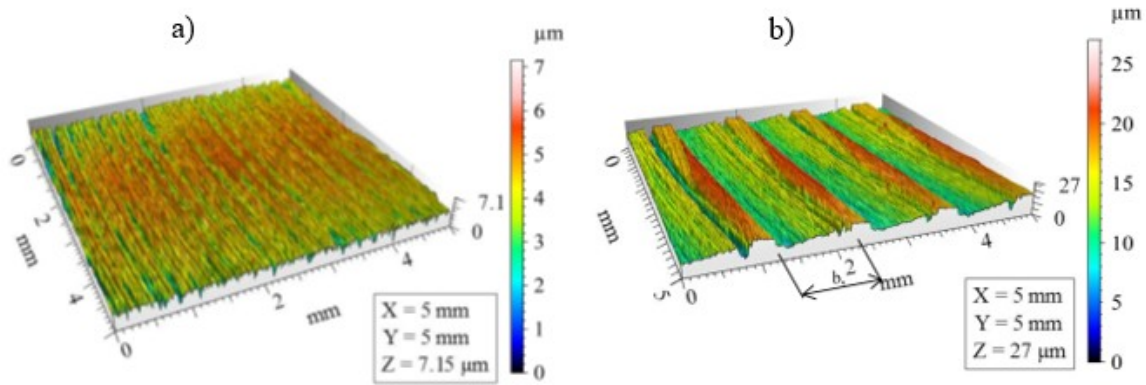
Table 4 shows the measured roughness values when cutting with one insert, while Table 5 summarizes the results when five inserts were used in the milling head simultaneously.

Based on the examination of the tabular values, it is quite clear that much higher roughness values were obtained when cutting with five inserts. This is shown even more vividly in the comparison diagrams shown in Fig. 13. It can also be seen from the graphs in Fig. 13, thanks to the high rigidity of the tool and the machine, the high force does not affect the roughness dramatically. However, in the vicinity of the  $a_p/f_z$  ratio value of one, the roughness is not favourable, as there is a breaking point on the curves showing the cutting with five inserts ( $R_{z5}$  and  $S_{10z5}$ ).

In the case of all examined 2D and 3D roughness parameters, approximately 3/6-fold increase was observed when five inserts were used compared to the results with a single one. The axial runouts of the inserts were previously described, where the deviations were between 20 and 49 microns. It can be seen that the roughness maxima are smaller even for the smallest run-out. So in most cases, a single insert will actually form the surface topography. The proof of this is shown in Fig. 14: part a) of the figure shows the surface roughness obtained by cutting with one insert, while part b) shows



**Figure 13.** Comparison charts of roughness values (a)  $R_a$  and  $S_a$ ; b)  $R_z$  and  $S_{10z}$



**Figure 14.** Surface topography images for  $f_z = 0.4$  mm (a) one insert; b) five inserts

the result of cutting with five inserts. The figures show the raw measured surfaces for the greatest applied feed value ( $f_z = 0.4$  mm) without the use of filters, which is why larger values are visible than in the previous tables.

In Fig. 14, the edge section parallel to the machined surface is also drawn ( $b_s$ ). Since the value of  $b_s = 1.2$  mm, in part a) of the figure, the surface created by the edge roughness of the tool superimposed to the vibrations appears. On the other hand, in part b) of the figure,  $b_s$  clearly appears, as well as the repetition period of  $f = 2$  mm, so the imprint of a single insert is indeed displayed with the repetition corresponding to the feed per revolution value ( $f$ ).

#### 4. Conclusions

Based on the tests carried out, the following conclusions were reached:

- First of all, it should be mentioned that during cutting experiments, it is worth examining the tools used from as many points of view as possible, since manufacturers often do not make all detailed information public about their products. Continuous improvements help in the development of better-performing tools, however, in experimental works, especially if the goal is to simulate the process with theoretical or numerical modeling, it is important to strive for an accurate geometrical description of the used tools. In the present work, it was revealed that the insert has a faceted design, which was not disclosed by the manufacturer.
- In the case of face milling with several cutting inserts, the axial run-out of the inserts significantly transforms the forces, often significantly increasing the values of some force components.
- The conclusion regarding the cutting ratio is that the use of the vicinity of the  $a_p/f_z$  ratio of 1 is not recommended, especially when using more than one insert, as values of the  $F_c$  and  $F_f$  force components were the largest here, however it has not affected the surfaces roughness significantly.

#### 5. Acknowledgement

This research was supported by the National Research, Development, and Innovation Office (Hungary), grant number NKFI-125117. Project no. NKFI-125117 has been implemented with the support provided from the National Research, Development and Innovation Fund of Hungary, financed under the K\_17 funding scheme.



## 6. References

- [1] A. Amiruddin, S. Lubis, *Effectiveness of CNC Turning and CNC milling in machining process*, International Journal of Economic, Technology and Social Sciences 2(2), pp. 575–583, [CrossRef](#)
- [2] X. Chen, C. Li, Y. Tang, L. Li, Y. Du, L. Li, *Integrated optimization of cutting tool and cutting parameters in face milling for minimizing energy footprint and production time*, Energy 175(15), 2019, pp. 1021–1037, [CrossRef](#)
- [3] D.Y. Pimenov, A.T. Abbas, M.K. Gupta, I.N. Erdakov, M.S. Soliman, M.M. el Rayes, *Investigations of surface quality and energy consumption associated with costs and material removal rate during face milling of AISI 1045 steel*, International Journal of Advanced Manufacturing Technology 107(7–8), 2020, pp. 3511–3525, [CrossRef](#)
- [4] A. M. Khan, M. Jamil, K. Salonitis, S. Sarfraz, W. Zhao, N. He, M. Mia, G. Zhao, *Multi-Objective Optimization of Energy Consumption and Surface Quality in Nanofluid SQCL Assisted Face Milling*, Energies 12(4), 2019, p. 710, [CrossRef](#)
- [5] A. Mgherony, B. Mikó, *The Effect of the Cutting Speed on the Surface Roughness When Ball-End Milling*, Hungarian Journal of Industry and Chemistry 49(2), 2021, [CrossRef](#)
- [6] R. Benotsmane, L. Dudás, G. Kovács, *The Concept of Autonomous Systems in Industry 4.0*, Advanced Logistic Systems - Theory and Practice 12(1), 2018, pp. 77–87, [CrossRef](#)
- [7] I. Korkut, M.A. Donertas, *The influence of feed rate and cutting speed on the cutting forces, surface roughness and tool-chip contact length during face milling*, Materials & Design 28(1), 2007, pp. 308–312, [CrossRef](#)
- [8] B. Rao, C.R. Dandekar, Y.C. Shin, *An experimental and numerical study on the face milling of Ti-6Al-4V alloy: Tool performance and surface integrity*, Journal of Materials Processing Technology 211(2), 2011, pp. 294–304, [CrossRef](#)
- [9] M.H. Ali, B.A. Khidhir, M.N.M. Ansari, B. Mohamed, *FEM to predict the effect of feed rate on surface roughness with cutting force during face milling of titanium alloy*, HBRC Journal 9(3), 2013, pp. 263–269, [CrossRef](#)
- [10] Ş. Aykut, M. Gölcü, S. Semiz, H.S. Ergür, *Modeling of cutting forces as function of cutting parameters for face milling of satellite 6 using an artificial neural network*, Journal of Materials Processing Technology 190(1-3), 2007, pp. 199–203, [CrossRef](#)
- [11] K.A. Abou-El-Hossein, K. Kadrigama, M. Hamdi, K.Y. Benyounis, *Prediction of cutting force in end-milling operation of modified AISI P20 tool steel*, Journal of Materials Processing Technology 182(1–3), 2007, pp. 241–247, [CrossRef](#)
- [12] N.T. Nguyen, *A development method of cutting force coefficients in face milling process using parallelogram insert*, EUREKA, Physics and Engineering 5, 2021, pp. 36–52, [CrossRef](#)
- [13] J. Kundrák, A.P. Markopoulos, T. Makkai, N.E. Karkalos, *Effect of Edge Geometry on Cutting Forces in Face Milling with Different Feed Rates*, MManufacturing Technology 19(6), 2019, pp. 984–992, [CrossRef](#)

- [14] J. Kundrák, K. Gyáni, Cs. Felhő, I. Deszpoth, *The Effect of the Shape of Chip Cross Section on Cutting Force and Roughness when Increasing Feed in Face Milling*, *Manufacturing Technology* 17(3), 2017, pp. 335-342, [CrossRef](#)
- [15] M.Z. Akkad, Cs. Felhő, *Effect of Depth of Cut and Feed Rate on the Forces in Face Milling*, Conference: MultiScience - XXXIII. microCAD International Multidisciplinary Scientific Conference 2019, [CrossRef](#)
- [16] B. Chirita, C. Grigoras, C. Tampu, E. Herghelegiu, *Analysis of cutting forces and surface quality during face milling of a magnesium alloy*, in *IOP Conference Series: Materials Science and Engineering* 591, 2019, 012006, [CrossRef](#)
- [17] P. Charalampous, *Prediction of Cutting Forces in Milling Using Machine Learning Algorithms and Finite Element Analysis*, *Journal of Materials Engineering and Performance* 30(3), 2021, pp. 2002–2013, [CrossRef](#)
- [18] J. Kundrák, B. Karpuschewski, Z. Pálmai, Cs. Felhő, T. Makkai, D. Borysenko, *The energetic characteristics of milling with changing cross-section in the definition of specific cutting force by FEM method*, *CIRP Journal of Manufacturing Science and Technology* 32, 2021, pp. 61–69, [CrossRef](#)
- [19] P. Muthuswamy, *Influence of micro-geometry of wiper facet on the performance of a milling insert: an experimental investigation and validation using numerical simulation*, *Sādhanā* 47, 2022, p. 140, [CrossRef](#)
- [20] B.Z. Balázs, M. Takács, *Finite element simulation of micro-milling of hardened tool steel*, *IOP Conference Series: Materials Science and Engineering* 1246, 2021, 012019, [CrossRef](#)
- [21] Walter Tools: *Main Catalogue*, 2017, p. 2605

# Microstructural study of an aluminium sheet deformed by multistage process

Gyula Pál<sup>a,b\*</sup>, Purnima Chakravarty<sup>a,b</sup>, János György Bátorfi<sup>a,b</sup>, Juriij Sidor<sup>a</sup>

<sup>a</sup> ELTE, Faculty of Informatics, Savaria Institute of Technology

<sup>b</sup> ELTE, Faculty of Science, Doctoral School of Physics

## ABSTRACT

The current as well as the future industrial market for Aluminium (Al) is huge and various research is being under work regarding the usability of Aluminium. However, during the deep drawing of Aluminium several issues can be developed and some of them are originated from the fundamental material properties. One of these factors is the material texture, which is the preferred orientation of the constituent polycrystalline Al, and the characteristic texture is affected by different rolling and annealing recipes. To investigate the material texture, symmetric and asymmetric rolling trials were performed on a commercially available Al 1050 sample. Energy-dispersive X-ray Spectroscopy (EDX), and Electron Backscatter Diffraction (EBSD) scanning has performed to determine the material composition and the crystallographic orientations of the investigated samples.

**Keywords:** *aluminium, microstructure, texture*

## 1. Introduction

Aluminium as a material is widely used in the industry because of its low density and high corrosion resistance. There are several methods already existing in the industry for the processing of Aluminium that can provide optimum material properties. The hollow geometry parts i.e. cups are generally manufactured with relatively small wall thickness, which is commonly produced by the method of deep drawing. However, during the process of deep drawing 5 main issues can be emerged, namely frame wrinkling, wall wrinkling, tearing, earing, and surface scratches [1]. These manufacturing defects originate from different sources. Many manufacturing defects can arise from the non-conformance of manufacturing conditions such as worn out or poorly maintained production equipment, or ignoring of work instructions. Some defects i.e. earing and tearing are caused by the ignorance of different mechanical properties of Aluminium e.g. yield strength and planar anisotropy compared to the better deep-drawability characteristics of steel [2].

The advancement in Aluminium research suggests that it is possible to develop materials with better mechanical properties by non-chemical processes [3]. This is the motivation of the current study. Generally, it is possible to influence the following properties of a base material by [4]:

- The chemical composition;
- Different heat treatment methods;
- Mechanical processing.

---

© ELTE, Faculty of Informatics, Savaria Institute of Technology, 2022

\*Corresponding author: Gyula Pál, pg@inf.elte.hu

<https://doi.org/10.37775/EIS.2022.2.6>

The production steps of sheets classically consist of the hot and cold rolling of casted ingots with optional intermediate and final annealing. During conventional i.e. symmetric rolling, the material passes between two rolls, which rotates opposite to each other with the same angular velocity [5]. However, in the last few decades, experiments are conducted using asymmetric rolling, i.e. the rolls are rotating with a different angular velocity, bringing in an extra shear strain into the material. These processing steps have a significant effect on the mechanical properties, which can be explained at the microstructural level [6].

The atoms of the metals - like Aluminium - forms microscopic crystal lattice. These crystals form groups, where they are grow in the same direction, creating the grains of a polycrystalline microstructure [7]. The dimension and shape of the polycrystal can be evaluated by several methods like the electron microscope, X-Ray diffraction, and Synchrotron Radiation [8]. Nowadays one of the most common methods to characterise polycrystalline material is scanning electron microscope equipped with an electron backscatter diffraction detector (EBSD) [9]. When the electron beam is projected on a specimen under consideration, the instrument detects the backscattered electrons, resulting in the formation of Kikuchi-patterns via the phenomenon of diffraction [10]. These patterns can reveal the orientation of crystals in the examined area. The repetition of this test on every point of a selected sample area shows a grain orientation map called inverse pole figure (IPF). The IPF can reveal the shapes, dimensions, and orientations of the grains spotted on the specimen area, providing necessary information for the analysis of microstructure [11].

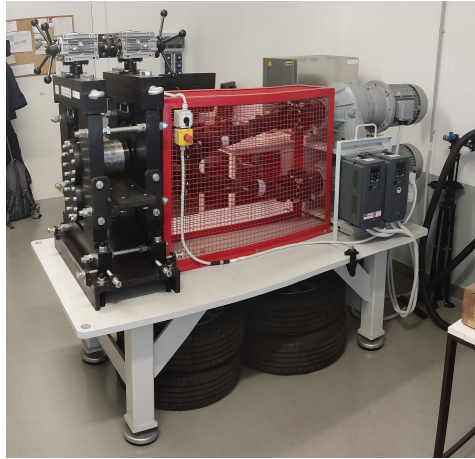
Very important characteristic of a material is the texture, which is the orientation distribution of its crystals [12]. To characterize the texture of materials, quite often the orientation distribution function (ODF) is employed, which shows all of the crystallographic orientations in Euler space [11], based on their angle deviations compared to a specified direction, i.e. rolling direction.

The common directions i.e. textures have received unique names, also specified texture groups are existing which are called fibers, because these typical groups are creating elongated fiber-like patterns within the Euler space [13]. The most common fibers are the  $\beta$ -fiber created by the Copper, S, and Brass textures, the  $\alpha$ -fiber ( $\langle 110 \rangle // ND$ ) and the  $\gamma$ -fiber ( $\langle 111 \rangle // ND$ ). In the Face Centered Cubic (FCC) metals, the  $\alpha$ -fiber and  $\beta$ -fiber components are indicative of plane strain compression, while the  $\gamma$ -fiber tends to appear after shear [14–16]. However, annealing can transform the deformation textures to recrystallization textures, like the Cube (100  $\langle 001 \rangle$ ) [11, 17].

Several studies were published about the connection of microstructure, texture, and material characteristics [18–24]. Based on this literature sources, it is possible to develop recipe e.g. rolling and annealing methods, which help to achieve the desired mechanical properties i.e. the normal anisotropy (Lankford number) over 1.1, and planar anisotropy correlating to 0 [25]. The most preferable textures to achieve these values are the random and shear textures [3].

The change of mechanical properties, i.e. the hardness is connected to the accumulation of deformation, and the evolution of dislocation density. These crystal defects are responsible for the work hardenings, thus measuring the hardness we can estimate the dislocation density and the driving force for recrystallization [26].

In this study, we are analysing the rolling experiment, which contains one step of asymmetric rolling and two steps of symmetric rolling followed by a particular annealing routine. The evolution of microstructure, texture, and mechanical properties during the conducted thermo-mechanical processing (TMP) steps has been reported in this work.



**Figure 1.** Laboratory rolling mill

## 2. Methodology

The experimental work includes the use of Aluminium sheets with starting dimension of  $1000 \times 2000$  mm and with 2 mm of nominal thickness. The base material was Aluminium alloy (AA) 1050, which is the commercially available purest alloy with min. 99.5 wt% of Aluminium content according to the standard EN 573-3:2019, although the measured value was  $99.7 \text{ wt}\% \pm 0.545\%$  which was recorded by an Octane Plus energy-dispersive X-ray spectroscopy (EDX)-detector.  $70 \times 200$  mm samples were cut for further steps by a water jet machine, preventing unnecessary heat transfer into the material. In order to facilitate the cold rolling process with the laboratory rolling mill, and to eliminate the traces of the industrial thermomechanical processes, the material was subjected to annealing at  $250 \text{ }^\circ\text{C}$  for 60 minutes.

The sample was deformed by cold rolling on a laboratory rolling mill (Fig. 1). This equipment is equipped with two motors, which can independently turn the two rolls through the connecting planetary gears and Cardan shafts. The motors are receiving the energy through their own inverters, making it possible for the machine to individually control the speed in the two rolls i.e. asymmetric rolling. The roll gap (distance between the rolls) is adjustable through two worm gears.

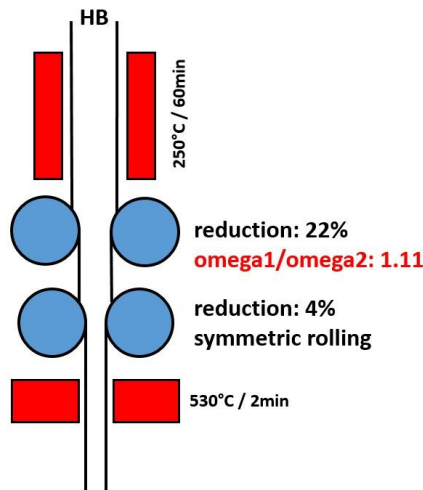
Main data of the rolling mill:

- 2 pcs of 3-phase 7.5 kW motor;  $M = 7750 \text{ Nm}$ ,
- Each motor has equipped with individual planetary gear;  $R = 141 \text{ mm}$ ,
- Each motor is feed by an individual frequency inverter;  $f = 25 \text{ Hz} \mapsto 50 \text{ Hz}$ ,
- Transmission: Cardan shafts,
- Rolls:  $d = 150 \text{ mm}$ .

The initial thickness of the sample was 1.90 mm measured by caliper on multiple points, taking an average from the measurements. The first step was an asymmetric rolling with an asymmetry ratio of 50:45 which is 1.1. The calculation is based on the applied frequency adjusted on the motor inverters. The sample thickness was reduced to 1.49 mm, consequently, the reduction has calculated as following [1]:

$$\varepsilon = \frac{h_i - h_f}{h_i} \cdot 100, \quad (1)$$

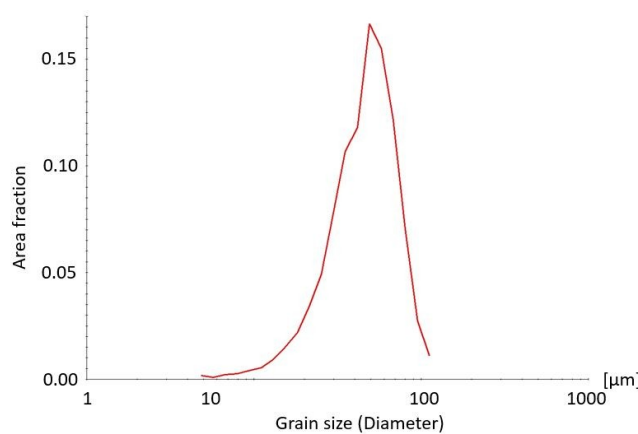
where,  $h_i$  stands for the initial thickness, and  $h_f$  stands for the final thickness. The first step resulted in a 21.58% reduction. The rolled material was processed through one more symmetric rolling



**Figure 2.** Flowchart of the TMP

schedules; given as the following reduction of the thickness to 1.43 mm. After cold deformation, a recrystallization annealing was performed at 530 °C for 120 s (Fig. 2).

The sample preparation for the Electron Backscatter Diffraction (EBSD) scanning includes mechanical grinding and polishing. The mechanical polishing resulted in a mirror-polished surface, which was applicable for the electrolytic polishing, which is required for the EBSD-scanning. During this process we followed the ordinary method of metallographic sample preparation, i.e. the grinding was made using wet sandpapers with grit size 400  $\rightarrow$  600  $\rightarrow$  800  $\rightarrow$  1000  $\rightarrow$  2000, and 240 rpm. The grinded sample was hand polished using Struers® polishing discs with 3  $\mu$ m and 1  $\mu$ m-size diamond suspensions at 400 rpm. The sample preparation was conducted in such a way that, after every step, the sample surface was cleaned by running water, cotton ball, dishwasher detergent, and dried. The electrolytic polishing for the sample was performed at 28 V for 45 s using A2 Struers electrolyte in the temperature range of 5 °C to 10 °C. The transverse direction plane (TD-plane) of the rolled sample was investigated. The prepared surface was examined by a FEI Teneo scanning electron microscope, which was equipped with the EBSD-detector. The recorded data was post-processed by the OIM-TSL-8 software. Furthermore hardness test has performed on the samples by a ZwickRoell ZHV $\mu$  hardness tester, using the Vickers-method with 500 gram-force (gf) load.



**Figure 3.** Grain size (diameter) in the function of area fraction

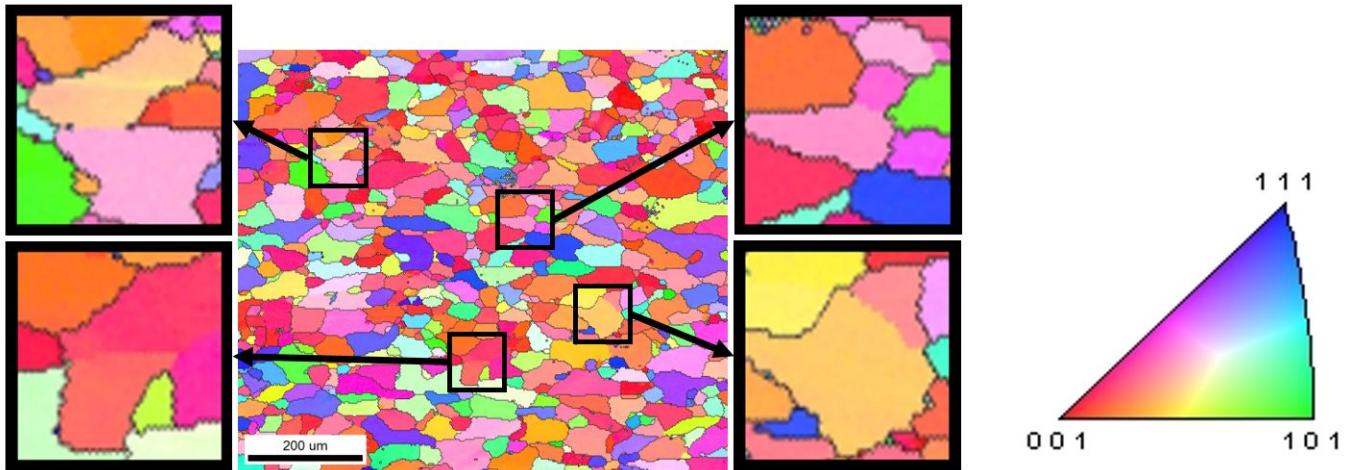


Figure 4. Microstructure of cold rolled and annealed material

### 3. Results

The microstructure analysis of recrystallized material reveals several grains with 0 0 1<uvw> orientation. The majority of grains have quite uniform orientation distribution, but in some cases, the low angle grain boundaries are also visible – see (Fig. 4). The average grain size of 48.5 μm was calculated by the weighted area of the grains from the distribution, shown in (Fig. 3).

In the ODF (Fig. 5), a strong Cube texture is observable with a strength up to 10.5 m.r.d (multiples of a random distribution). Apart from this, there are remaining traces of deformation texture components with relatively low intensity (~1 – 1.3 m.r.d). The absence of E and F textures indicates that the shear strain was negligibly small in the measured sample.

To better understand the TMP of the investigated material, it is important to determine the dislocation density and the stored energy (ED) after every rolling step. The stored energy is the energy originated from the formation of the dislocations and is also mentioned as the driving force for recrystallization. Since the dislocations have a direct impact on the hardness of a material, the driving force can be calculated by the following formula [27, 28]:

$$ED = \frac{H_V^2}{G \cdot (3.06M\alpha)^2}, \tag{2}$$

where the  $H_V$  is the Vickers hardness of the material in MPa (the given results are shown in (Fig. 6)),

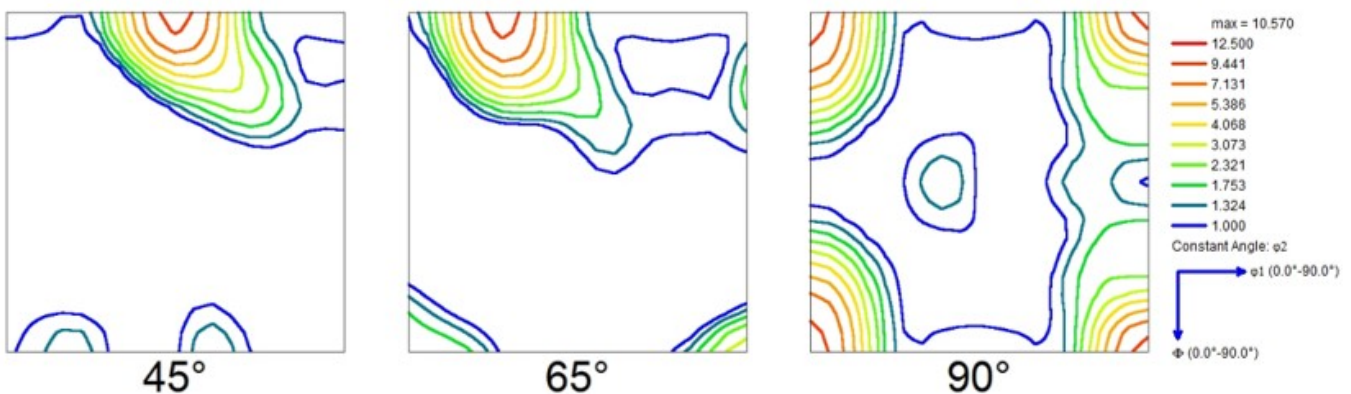
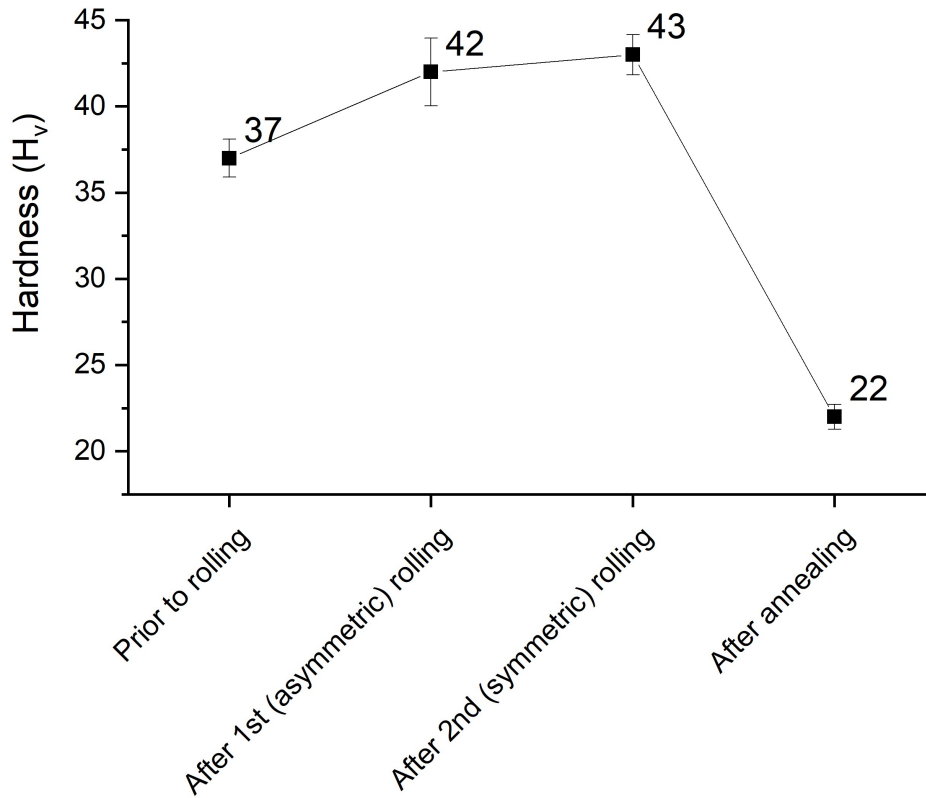


Figure 5. Texture of cold rolled and annealed material



**Figure 6.** Change of hardness during the TMP

$G$  is the shear modulus of Al,  $M$  is the Taylor factor, and the  $\alpha$  is the geometric constant [13, 26, 29], it can be estimated by (3) [18]:

$$\alpha \approx \frac{1 - 0.5\nu}{4\pi(1 - \nu)} \ln \left( \frac{\rho^{-0.5}}{b} \right), \tag{3}$$

where  $\nu$  is 0.33 (this is typical value for high purity Al alloys) [7, 30, 31], and  $\rho$  is the dislocation density, which was estimated by [14]. Another method for calculation stored energy is apply the formula from [13] modified using the Kubin-Estrin (KE) model is:

$$E_{D\_KE} = \alpha \cdot \rho_{\epsilon(eq)} \cdot G \cdot b^2. \tag{4}$$

The calculated values of the stored energy and  $\alpha$  are visible in Table 1.

In case of asymmetric rolling, the compressive and the possible shear strain and the equivalent

**Table 1.** Stored energy and  $\alpha$  values during the rolling process

	Stored energy $\cdot 10^5$ [J/m <sup>3</sup> ]	Stored energy (Kubin-Estrin) $\cdot 10^5$ [J/m <sup>3</sup> ]	$\alpha$
Sample before rolling	2.26	-	0.535
After 1 <sup>st</sup> (asymmetric) rolling	2.59	3.19	0.529
After 2 <sup>nd</sup> (asymmetric) rolling	2.73	3.23	0.528



strain are needed to be calculated:

$$\varepsilon_{\text{eq}} = \frac{2}{\sqrt{3}} \Phi \ln \frac{1}{\alpha_x}, \quad (5)$$

where

$$\alpha_x = \frac{h_f}{h_i}, \quad (6)$$

$$\Phi = \sqrt{1 + \left( \frac{\alpha_x^2}{1 - \alpha_x^2} \tan \Psi \right)^2}, \quad (7)$$

$$\Psi = \arctan \left( \frac{R}{2s} \left( \frac{\omega_{\text{upper}}}{\omega_{\text{lower}}} \left( \arccos \left( \frac{R - \omega_{\text{lower}} \frac{e-s}{\omega_{\text{upper}}}}{R} \right) \right) - \arccos \left( \frac{R + s - e}{R} \right) \right) \right), \quad (8)$$

$$e = \frac{h_i}{2}, \quad (9)$$

$$s = \frac{h_f}{2}, \quad (10)$$

where,  $R$  is the radius of the rolls,  $\omega_{\text{upper}}$ , and  $\omega_{\text{lower}}$  are the angular velocity of the upper and lower rolls respectively, and  $\Psi$  is the shear angle. During the above calculations [17], the initial equivalent strain before the first rolling step is  $\varepsilon = 1.363$ . This value has calculated based on the correlation of the strain and the dislocation density:

$$\frac{d\rho_m}{d\varepsilon} = \frac{C_1}{b^2} - C_2\rho_m - \frac{C_3}{b} \sqrt{\rho_f}, \quad (11)$$

$$\frac{d\rho_f}{d\varepsilon} = C_2\rho_m + \frac{C_3}{b} \sqrt{\rho_f} - C_4\rho_f, \quad (12)$$

where  $\rho_m$  is the density of the mobile dislocations,  $\rho_f$  is the density of the forest dislocations,  $C_1$  is the factor connected to mobile dislocation multiplication,  $C_2 = 1.1 \text{ 1/m}^2$  is the factor of the annihilation and trapping of mobile dislocations,  $C_3 = 4 \cdot 10^5 \text{ 1/m}$  is the factor of the immobilization of them, and  $C_4$  is the factor of the immobilization of the dislocations by the dynamic recovery. The given values are valid at 293 K [32, 33].

Prior to cold rolling the investigated material was hot rolled, and therefore large number of dislocations was generated. Although the material was annealed prior to cold rolling, the low-temperature annealing led to partial recovery, meaning that the investigated material still contains a large amount of dislocations based on the hardness test results, as it is visible in Table 2.

The sum of the forest and mobile dislocations is equals the total dislocation's amount [34]. The calculation of dislocation density, based on the hardness test, can be expressed as:

$$\rho = \frac{1}{\alpha^3} \left( \frac{H_V}{3.06Mgb} \right)^2. \quad (13)$$

**Table 2.** Dislocation density calculated by the indentation technique and the modified Kubin-Estrin model

	$\cdot 10^{14} \rho$ [1/m <sup>2</sup> ]	$\rho_{\varepsilon(\text{eq})}$ (Kubin-Estrin) $\cdot 10^{14}$ [1/m <sup>2</sup> ]	$\varepsilon_{\text{eq}}$ [-]
Sample before rolling	2.106	-	1.363
After 1 <sup>st</sup> (asymmetric) rolling	2.288	2.810	1.644
After 2 <sup>nd</sup> (asymmetric) rolling	2.300	2.944	1.691

Another approach to determine the dislocation density is the modified Kubin-Estrin model:

$$\rho(\varepsilon_{\text{eq}}) = \frac{2C_1}{C_4} - \left( \frac{2C_1}{C_4} - \rho_0 \right) \left( 1 + \frac{C_4 \varepsilon_{\text{eq}}}{2} \right) \exp(-C_4 \varepsilon_{\text{eq}}), \quad (14)$$

where  $\rho_0 = 10^{10} \text{ 1/m}^2$  [26] is the initial dislocation density,  $C_1 = 2.33 \cdot 10^{14} \text{ 1/m}^2$ , and  $C_4$  has the value of  $1.2 \text{ 1/m}$ . The given parameter values are valid for 293 K [32]. The results of equivalent strain and different dislocation density calculations are presented in Table 2.

During the calculations of the dislocation density and stored energy, the equivalent strain of the sample before the first rolling step and the indentation-based dislocation density were determined with the  $\alpha = 0.5$ , since in the case of high strains the  $\alpha$  tends to saturate to this value [26]. For each strain increment the equivalent strains were added to each other, as displayed in Table 2.

#### 4. Discussion

The reported data suggests that, after the initial rolling, the orthorhombic symmetry remained intact due to the lower level of asymmetry maintained during the rolling experiments. The presence of Cube texture is typically observed after conventional rolling and the following recrystallization. The integrity of the orthorhombic ODF symmetry and the lack of  $E$  and  $F$  shear textures can be originated from the low-level i.e. 50/45 asymmetry; although this level was sufficient for the appearance of a weak  $H$  shear texture. The overall symmetric-like rolling is the reason for the ordinary Cube- and  $\beta$ -fiber – type textures.

The minimal rise in the hardening after the second rolling pass can be originated from the low level additional deformation i.e. after a 22% reduction by an asymmetric rolling pass, a symmetric 4% reduction was performed which exposes the sample to a minimal normal strain.

The current study clearly depicts the fact that a 50/45 asymmetry level is not sufficient in the case of 1050 aluminium alloy to reach a substantial level of shear texture, thus a significantly higher level of asymmetry is needed to reach the desired  $H$ ,  $E$ , and  $F$  texture, and to destroy the Cube texture at the same time. The dislocation densities as well as the stored energies, predicted by the indentation technique and K-E model are of the same order of magnitude. The deviations between the measured and calculated values can be explained by the simplifications, made in the modified K-E approach.

#### 5. Conclusion

Results of the current investigation show that the low level of asymmetry is not capable of modifying the conventional texture, which tends to appear during thermomechanical processing. The higher degree of asymmetry might provide a desirable shear-type texture. The estimated dislocation density and driving force for recrystallization are correlated well with the data presented in various literature sources. The deviations observed between the measured and calculated counterparts might emerge from the simplifications made in the modeling approaches.

#### 6. Acknowledgement

Project no. TKP2021-NVA-29 has been implemented with the support provided by the Ministry of Innovation and Technology of Hungary from the National Research, Development and Innovation Fund, financed under the TKP2021-NVA funding scheme.

#### 7. References

- [1] ME Mechanical Team, *Defects in Sheet Metal Drawing*, [CrossRef](#)

- [2] O.M. Ikumapayi, S.A. Afolalu, J.F. Kayode, R.A. Kazeem, S. Akande, *A concise overview of deep drawing in the metal forming operation*, *Materials Today: Proceedings* 62, 2022, pp. 3233–3238, [CrossRef](#)
- [3] J. Sidor, R.H. Petrov, L.A.I. Kestens, *Deformation, recrystallization and plastic anisotropy of asymmetrically rolled aluminum sheets*, *Materials Science and Engineering: A* 528(1), 2010, pp. 413–424, [CrossRef](#)
- [4] J. Herrmann, M. Merklein, *Improvement of deep drawability of ultra-fine grained 6000 series aluminum alloy by tailored heat treatment*, *Procedia Manufacturing* 15, 2018, pp. 976–983, [CrossRef](#)
- [5] J.G. Lenard, M. Pietrzyk, L. Cser, *Mathematical and physical simulation of the properties of hot rolled products*, Amsterdam Lausanne New York: Elsevier, 1999.
- [6] O. Engler, K. Knarbak, *Temper rolling to control texture and earing in aluminium alloy AA 5050A*, *Journal of Materials Processing Technology* 288, 2021, p. 116910, [CrossRef](#)
- [7] W.D. Callister, *Materials science and engineering: an introduction*, 7th ed. New York: John Wiley & Sons, 2007.
- [8] X. Bian, L. Heller, L. Kadeřávek, P. Šittner, *In-situ synchrotron X-ray diffraction texture analysis of tensile deformation of nanocrystalline NiTi wire in martensite state*, *Applied Materials Today* 26, 2022, p. 101378, [CrossRef](#)
- [9] W.Q. Gao, C.L. Zhang, M.X. Yang, S.Q. Zhang, D. Juul Jensen, A. Godfrey, *Strain distribution and lattice rotations during in-situ tension of aluminum with a transmodal grain structure*, *Materials Science and Engineering: A* 828, 2021, p. 142010, [CrossRef](#)
- [10] S. Nishikawa, S. Kikuchi, *Diffraction of Cathode Rays by Mica*, *Nature* 121(3061), 1928, pp. 1019–1020, [CrossRef](#)
- [11] O. Engler, V. Randle, *Introduction to texture analysis: macrotexture, microtexture, and orientation mapping*, 2nd ed. Boca Raton: CRC Press, 2010.
- [12] S.I. Wright, R. Hielscher, *Structures: Orientation texture*, in *Reference Module in Materials Science and Materials Engineering*, Elsevier, 2022, p. B9780323908009000000, [CrossRef](#)
- [13] F.J. Humphreys, M. Hatherly, *Recrystallization and Related Annealing Phenomena*, Elsevier, 1995, [CrossRef](#)
- [14] S.H. Kim, J.H. Ryu, K.H. Kim, D.N. Lee, *The Evolution of Shear Deformation Texture and Grain Refinement in Asymmetrically Rolled Aluminum Sheets*, *Journal of the Society of Materials Science* 51(3), 2002, pp. 20–25, [CrossRef](#)
- [15] D.N. Lee, H.J. Shin, S.H. Hong, *The Evolution of the Cube, Rotated Cube and Goss Recrystallization Textures in Rolled Copper and Cu-Mn Alloys*, *KEM* 233–236, 2003, pp. 515–520, [CrossRef](#)
- [16] H. Jin, D.J. Lloyd, *The different effects of asymmetric rolling and surface friction on formation of shear texture in aluminium alloy AA5754*, *Materials Science and Technology* 26(6), 2010, pp. 754–760, [CrossRef](#)

- [17] J. Sidor, R.H. Petrov, L. Kestens, *Texture Control in Aluminum Sheets by Conventional and Asymmetric Rolling*, Comprehensive Materials Processing 3, 2014, pp. 447–498, [CrossRef](#)
- [18] W. Truszkowski, J. Kr'ol, B. Major, *Inhomogeneity of rolling texture in fcc metals*, MTA 11(5), 1980, pp. 749–758, [CrossRef](#)
- [19] W. Truszkowski, J. Krol, B. Major, *On Penetration of Shear Texture into the Rolled Aluminum and Copper*, MTA 13(4), 1982, pp. 665–669, [CrossRef](#)
- [20] M.Y. Amegadzie, D.P. Bishop, *Effect of asymmetric rolling on the microstructure and mechanical properties of wrought 6061 aluminum*, Materials Today Communications 25, 2020, p. 101283, [CrossRef](#)
- [21] O.V. Mishin, B. Bay, G. Winther, D.J. Jensen, *The effect of roll gap geometry on microstructure in cold-rolled aluminum*, Acta Materialia 52(20), 2004, pp. 5761–5770, [CrossRef](#)
- [22] H. Jin, D.J. Lloyd, *The reduction of planar anisotropy by texture modification through asymmetric rolling and annealing in AA5754*, Materials Science and Engineering: A 399(1–2), 2005, pp. 358–367, [CrossRef](#)
- [23] B. Beausir, S. Biswas, D.I. Kim, L.S. Tóth, S. Suwas, *Analysis of microstructure and texture evolution in pure magnesium during symmetric and asymmetric rolling*, Acta Materialia 57(17), 2009, pp. 5061–5077, [CrossRef](#)
- [24] S. Wronski, B. Ghilianu, T. Chauveau, B. Bacroix, *Analysis of textures heterogeneity in cold and warm asymmetrically rolled aluminium*, Materials Characterization 62(1), 2011, pp. 22–34, [CrossRef](#)
- [25] Horváth László, *Mélyhúzás lemezanyagai és minősítési módszereik*, Óbudai Egyetem, Bánki Donát Gépész és Biztonságtechnikai Mérnöki Kar, Anyagtudományi-és Gyártástechnológiai Intézet, 2009.
- [26] J.J. Sidor, P. Chakravarty, J.Gy. Bátorfi, P. Nagy, Q. Xie, J. Gubicza, *Assessment of Dislocation Density by Various Techniques in Cold Rolled 1050 Aluminum Alloy*, Metals 11(10), 2021, p. 1571, [CrossRef](#)
- [27] M. Taheri, H. Weiland, A. Rollett, *A method of measuring stored energy macroscopically using statistically stored dislocations in commercial purity aluminum*, Metallurgical and Materials Transactions A 37(1), 2006, pp. 19–25, [CrossRef](#)
- [28] A.A. Saleh, P. Mannan, C.N. Tomé, E.V. Pereloma, *On the evolution and modelling of Cube texture during dynamic recrystallisation of Ni–30Fe–Nb–C model alloy*, Journal of Alloys and Compounds 748, 2018, pp. 620–636, [CrossRef](#)
- [29] G.E. Dieter, *Mechanical metallurgy 3. ed*, London Hamburg: McGraw-Hill, 1988.
- [30] J.J. Sidor, K. Decroos, R.H. Petrov, L.A.I. Kestens, *Evolution of recrystallization textures in particle containing Al alloys after various rolling reductions: Experimental study and modeling*, International Journal of Plasticity 66, 2015, pp. 119–137, [CrossRef](#)
- [31] J.J. Sidor, *Assessment of Flow-Line Model in Rolling Texture Simulations*, Metals 9, 2019, p. 21, [CrossRef](#)

- [32] T. Csanádi, N.Q. Chinh, J. Gubicza, G. Vörös, T.G. Langdon, *Characterization of stress–strain relationships in Al over a wide range of testing temperatures*, International Journal of Plasticity 54, 2014, pp. 178–192, [CrossRef](#)
- [33] L.P. Kubin, Y. Estrin, *Evolution of dislocation densities and the critical conditions for the Portevin-Le Châtelier effect*, Acta Metallurgica et Materialia 38(5), 1990, pp. 697–708, [CrossRef](#)
- [34] T. Csanádi, N.Q. Chinh, J. Gubicza, T.G. Langdon, *Plastic behavior of fcc metals over a wide range of strain: Macroscopic and microscopic descriptions and their relationship*, Acta Materialia 59(6), 2011, pp. 2385–2391, [CrossRef](#)





**EÖTVÖS LORÁND UNIVERSITY  
FACULTY OF INFORMATICS  
SAVARIA INSTITUTE OF TECHNOLOGY**

